CRANFIELD UNIVERSITY

IZZATI IBRAHIM

ILLUMINATION INVARIANCE AND SHADOW COMPENSATION ON HYPERSPECTRAL IMAGES

CRANFIELD DEFENCE AND SECURITY

Academic Year: 2009-2013

Supervisor: Dr Peter Yuen
January 2013

CRANFIELD UNIVERSITY

CRANFIELD DEFENCE AND SECURITY

PhD

Academic Year 2009 - 2013

IZZATI IBRAHIM

ILLUMINATION INVARIANCE AND SHADOW COMPENSATION ON HYPERSPECTRAL IMAGES

Supervisor: Dr Peter Yuen

January 2013

ABSTRACT

To obtain intrinsic reflectance of the scene by hyperspectral imaging systems has been a scientific and engineering challenge. Factors such as illumination variations, atmospheric effects and viewing geometries are common artefacts which modulate the way of light reflections from the object into the sensor and that they are needed to be corrected. Some of these factors induce highly scattered and diffuse irradiance which can artificially modify the intrinsic spectral reflectance of the surface, such as that in the shadows.

This research is attempted to compensate the shadows in the hyperspectral imagery. In this study, three methods known as the Diffuse Irradiance Compensation (DIC), Linear Regression (LR) and spectro-polarimetry technique (SP) have been proposed to compensate the shadow effect. These methods have various degrees of shadow compensation capabilities, and their pros and cons are elucidated within the context of their classification performances over several data sets recorded within and outside of the laboratory. The spectro-polarimetry (SP) technique has been found to be the most versatile and powerful method for shadow compensation, and it has achieved over 90% of classification accuracy for the scenes with ~30% of shadow areas.

Keywords:

Hyperspectral, diffuse, direct irradiance, polarizer, illumination invariance, shadow

LIST OF PUBLICATION

Journal Paper

Illumination invariance and shadow compensation via spectro-polarimetry technique. **Ibrahim, I., Yuen, P., Hong, K., Chen, T., Soori, U., Jackman, J. and Richardson, M.** 10, Bellingham, WA : SPIE, 2012, Optical Engineering (OE), Vol. 51.

Shadow compensation and illumination invariance on hyperspectral images. **Ibrahim, I., Yuen, P., Hong, K., Chen, T., Soori, U., Jackman, J. and Richardson, M.** 2012, under review of Imaging Science Journal.

Shadow compensation using spectro-polarimetry technique on hyperspectral images, **Ibrahim, I., Yuen, P., Hong, K., Soori, U., Chen WT and Richardson, M.** Paper to be submitted to the Int. Journal of Remote Sensing.

Conference and Poster Paper

Illumination independent object recognitions in hyperspectral imaging. **Ibrahim, I., Yuen, P., Tsitiridis, A., Hong, K., Chen, T., Jackman, J., James, D. and Richardson, M.** Touluse, France : SPIE, 2010. Proceedings of the SPIE 7838. Vol. 7838, pp. 78380O-1-12 .

Shadow compensation on hyperpsectral imageries. **Ibrahim, I., Yuen, P., Soori, U., Chen, T., Hong, K., Tsitiridis, A., Jackman, J. and Richardson, M.** Shrivenham, Swindon : Defence Academy of the United Kingdom, 2012. 10th Electro-optics & Infrared Conference.

Enhanced object recognition in cortex-like machine. **Tsitiridis, A., Yuen, P. W. T., Ibrahim, I., Soori, U., Chen, T., Hong, K., Wang, Z., James, D. and Richardson, M.** Corfu : IEEE/EANN, 2011. 12th EANN / 7th AIAI Joint Conference on Engineering Application.

Colour invariant target recognition in multiple camera CCTV surveillance. **Soori, U., Yuen, P. W. T., Ibrahim, I., Tsitiridis, A., Hong, K., Chen, T., Jackman, J., James, D. and Richardson, M.** Prague : SPIE, 2011. Proceedings of the SPIE. Vols. 8189A-24.

Assessment of tissue blood perfusion in-vitro using hyperspectral and thermal imaging techniques. **Chen, T., Yuen, P. W. T., Hong, K., Ibrahim, I., Tsitiridis, A., Soori, U., Jackman, J., James, D. and Richardson, M.** Wuhan, China : IEEE, 2011. 5th International Conference on Bioinformatics and Biomedical.

Bulletin Paper

Ibrahim, I., Yuen, P., Tsitiridis, A., Hong, K., Chen, T., Jackman, J., James, D. and Richardson, M. Spectral constancy on hyperspectral imageries. *Defence S&T Technical Bulletin.* 2011, Vol. 4, 1, pp. 19-30.

Yuen, P., Ibrahim, I., Hong, K., Chen, T., Tsitiridis, A., Jackman, J., Kam, F., Jackman, J., James, D. and Richardson, M. Classification enhancements in hyperpsectral remote sensing using atmospheric correction preprocessing technique. *Defence S&T Technical Bulletin.* 2009, Vol. 2, 2, pp. 91-99.

ACKNOWLEDGEMENTS

I would like to thank Dr Yuen for his supervision, support and valuable guidance during my PhD study. I also would like to thank Prof. Dr. Richardson for taking time out of his busy schedules to assists me in my research and my journal paper. I am also grateful to the Malaysian Ministry of Science, Technology and Innovation and Malaysian Science Technology Research Institute for Defence for sponsoring and giving me an opportunity to do my PhD study. Finally, I would like to thank my family especially Haniff Zaid, Dr Ismaeel and my lovely children, Hafiff and Haifa for their patience and supports during my PhD course.

TABLE OF CONTENTS

LIST OF FIGURES

LIST OF TABLES

LIST OF EQUATIONS

GLOSSARY

AD	Anomaly detection
AMF	Adaptive matched filter
ATCOR	Atmospheric and topographic correction
ATREM	Atmosphere removal algorithm
BRDF	Bidirectional reflectance distribution function
DIC	Diffuse irradiance compensation
DN	Digital number
ED	Euclidean distance classifier
ELM	Empirical line method
EM	Electromagnetic
EO	Electro-optic
FD	Fisher linear discriminant classifier
FF	Flat Field
FLAASH	Fast line-of-sight atmospheric analysis of spectral hypercubes
FOV	Field of view
GLRT	Generalized likelihood ratio test
GMM	Gaussian mixture model

GMRX	Global Mean RX
GRX	Global RX
HATCH	High-accuracy atmospheric correction for hyperspectral data
HSI	Hyperspectral imaging
IAR	Internal average reflectance
IGRX	Iterated global RX
LR	Linear regression
LRX	Local RX
LWIR	Long wave infrared (8 to 14 μm)
MD	Minimum distance classifier
MF	Matched filter
MODTRAN	Moderate resolution atmosphere radiance and transmittance model
MSI	Multispectral imaging
MWIR	Mid wave infrared (3 to 5 μm)
PFA	Probability of false alarm
PoD	Probability of detection
QD	Quadratic likelihood classifier
QUAC	Quick atmosphere correction
RGB	Red green blue
ROC	Receiver operating characteristic
ROI	Region of interest
RX	Iriving Reed and Xiaoli Yu
SEM	Stochastic expectation maximization
SP	Spectro-polarimetry
SS	Single spectrum method
SWIR	Short wave infrared (1 to 2.4 μm)
TI	Thermal imager
VNIR	Visible to near infrared

1 HYPERSPECTRAL IMAGING SYSTEMS (HSI)

1.1 Motivation of Research

Hyperspectral imaging (HSI) is a technique that allows the intrinsic electro-optic (EO) properties, such as the reflectance and emissions of objects in the scene, to be acquired remotely. This information can then be used for a variety of applications including target detection and classification. The ultimate usefulness of the technology relies very much on whether the reflectance and emissions of the objects in the scene can be accurately retrieved from the image as observed by the HSI system. If a flat landscape of scenery is uniformly illuminated within the normal plane of the surface then it is possible to deduce the reflectance of the scene accurately. This is possible only if the viewing and illumination geometries are close to the normal plane and that the atmospheric parameters are known. However, this is not the case in general, partly due to the adjacency multiple diffuse scattering caused by nearby objects in the scene.

Objects under shadows exhibit rather different EO properties compared to objects that under direct illuminations. The reflected energy recorded by an imaging system from a shadowed object usually consists of only diffuse irradiance scattered by sky lights and adjacency surroundings objects. Therefore, the digital number (DN) value of shadowed target is always lower and it appears to look dark in the image, as shown in Figure 1-1.

The other issue when dealing with shadows in hyperspectral imageries is the softness of the shadow which can be represented by the ratio between the intensity of the shadow pixels with respected to that under direct illumination. The softness of shadows is scene dependent as shown in Figure 1-2. When a target is in hard shadow in which the direct illumination is completely blocked (i.e. no direct illumination), the apparent reflectance spectrum appears to be very weak approaching to almost zero. This is quite different for a target that is in partial shadow. The partially shadowed target will have non-zero reflection of

the diffuse irradiance. Therefore, it is important to assess the softness of the shadows to avoid overcorrection.

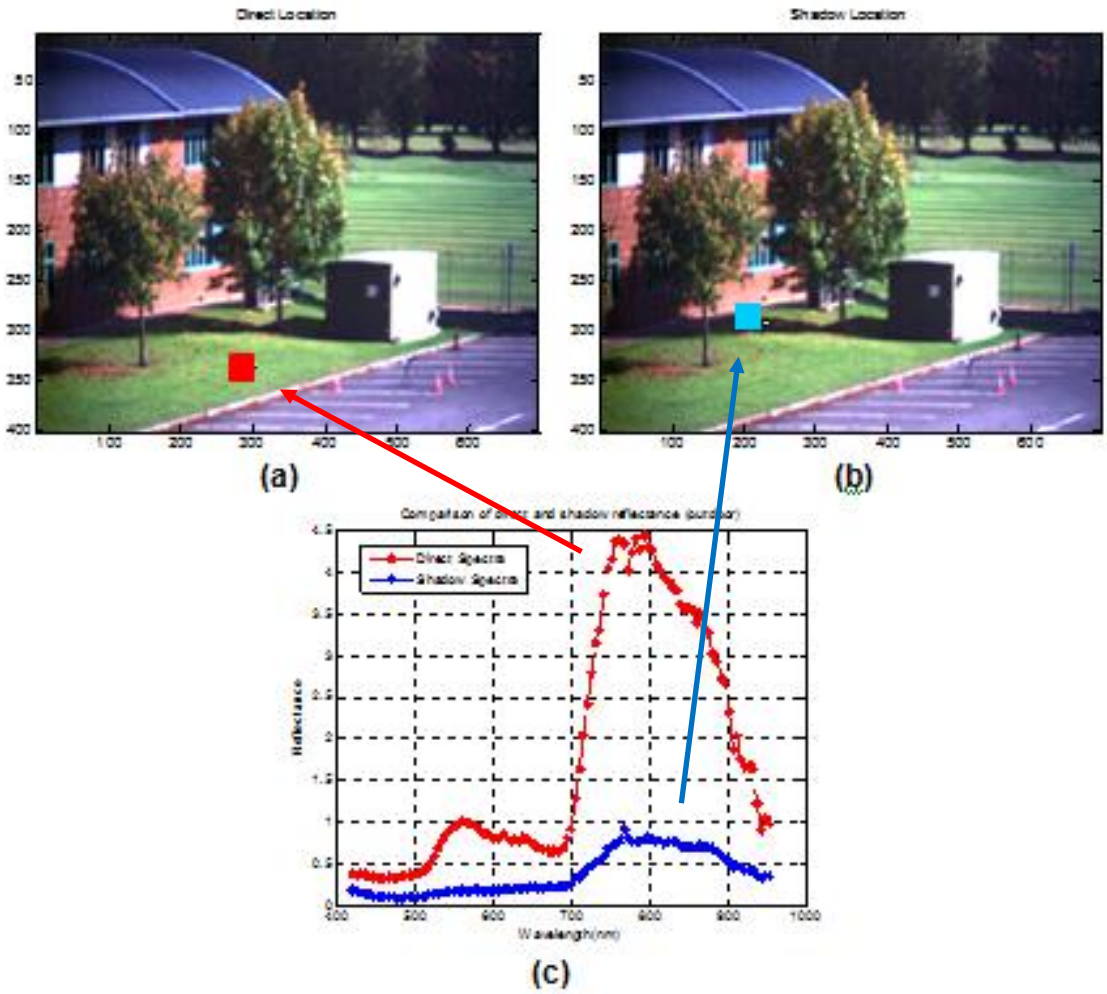

Figure 1-1 Reflection from the shadowed target appears to be weak (a) shows the location of fully illuminated ROI (red square), (b) shadow pixels (blue square) and (c) the plot shows that the spectral reflection of shadow is very weak in comparison to that under direct illumination.

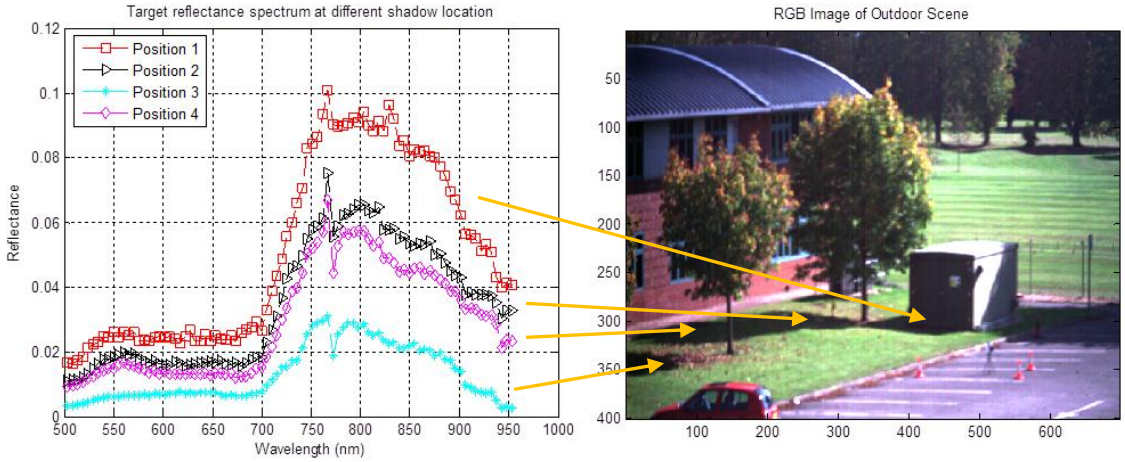

Figure 1-2 The spectral properties of the lawn at various locations of an outdoor scene. Note that different locations of the shadow regions exhibit different apparent reflectance values as estimated by Empirical Line Method (ELM). This is due to the various degrees of self shadowing effects.

1.2 Aim

It is evident that objects under shadow exhibit significant changes in the reflected energy and spectral shape. This will cause a considerably negative effect in target detection and classification. Therefore, the aim of this research is to develop a method to compensate shadow effects in hyperspectral imagery. The methodology adopted in this study involves:

1. Segmentation of direct and diffuse irradiance pixels from the hyperspectral images
2. Correction of apparent reflectance of the shadowed objects using information when the same object is under direct irradiance.

1.3 Introduction to HSI

Hyperspectral Imaging System (HSI) has been widely used in various applications especially when more information apart from textural and broadband RGB colours are required for the identification and discrimination of objects. Hyperspectral imaging system offers high resolution of spectral

information and it has been deployed in many applications, including agriculture (1, 2), surveillance (3), remote sensing (4, 5), medical (6, 7) and military (8). The HSI system takes hundreds or more of contiguous wavebands ranging from visible to near infrared (VNIR) region (0.4 to 0.95 μm) through the short wave infrared (SWIR) (1 to 2.4 μm), mid wave infra-red (MWIR) (3 to 5 μm) and up to long wave infrared (LWIR) (8 to 14 μm) region. Each waveband occupies very narrow slice of electromagnetic (EM) spectrum of approximately 5 to 20 nm wide, allowing the analysis to be performed on each individual waveband or a subset of a selection of them to maximise the spectral contrast between the target and the clutter background. For instance, HSI is able to distinguish targets of similar colours by exploiting slices of spectral information in a wide region as illustrated in Figure 1-3. Other conventional imaging systems such as broadband digital RGB will be unable to discriminate these look-alike targets.

1.3.1 HSI and Other Imaging Systems

Historically, much of the success in defence surveillance and reconnaissance has relied upon expert (human) interpretation such as by visual examination of the imagery data. Conventional imaging systems, namely panchromatic and broadband colour RGB, integrate the complete spectral range or broad bandwidths in the order of ~100-200nm. These systems are not capable to provide enough spectral information for target acquisition and can only provide spatial information of the scene.

Advanced imaging technology, such as a thermal imager (TI), capture emissions from targets rather than reflected light to form an image. The spectral range of the thermal imaging systems are mostly in the Middle Wave Infrared region (MWIR) 3 to 5 μm and Long Wave Infrared (LWIR) 8 to 14 μm. The advantage of using thermal imaging systems is that they can operate in an environment of total darkness and do not depend on the light of a scene as they capture thermal energy emitted from the targets. Most TI systems are less capable to sample IR radiations in narrow bandwidths and as a result, two different objects which emit the same integrated thermal energy would exhibit

similar radiance intensity in the thermal band. It is even more difficult to use the conventional TI system to detect targets that incorporate thermal camouflage techniques by concealing the thermal radiation to blend into the surrounding.

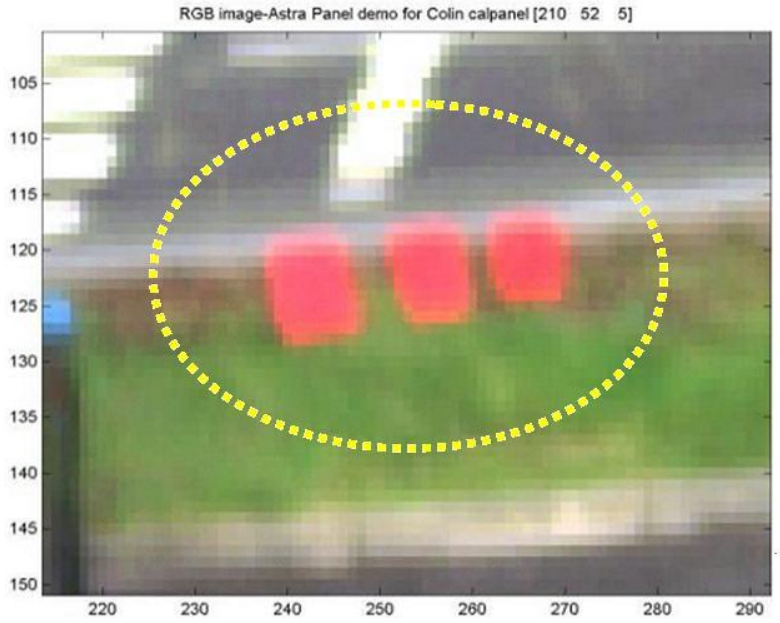

(a)

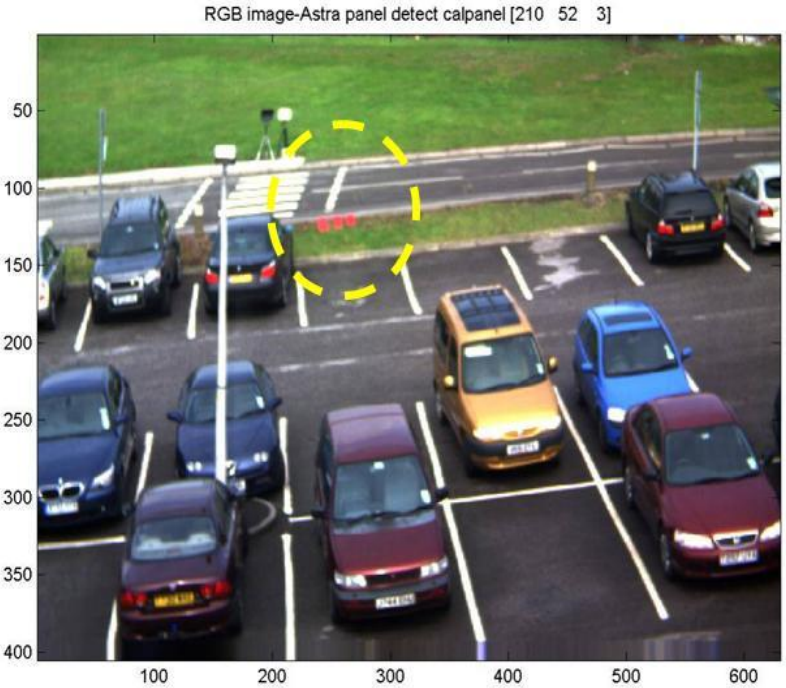

(b)

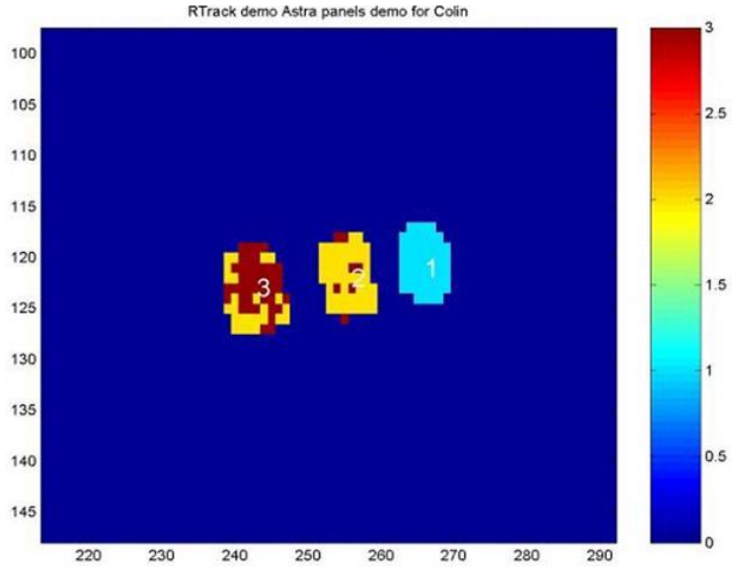

(c)

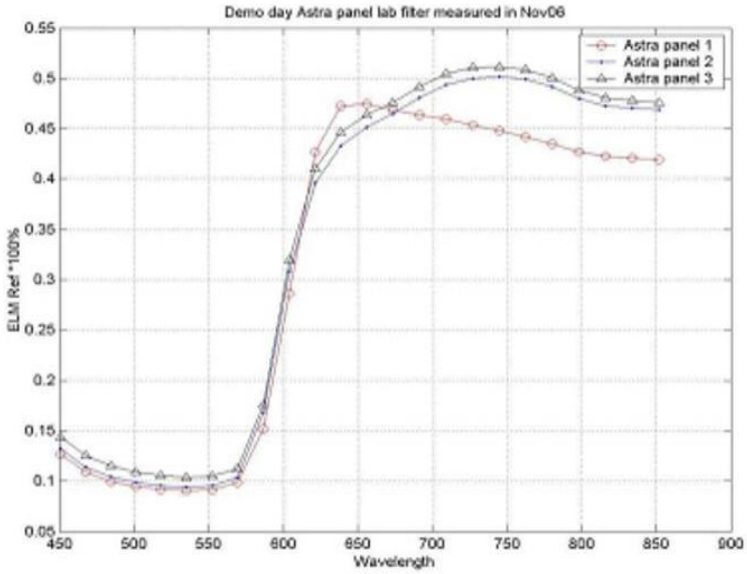

(d)

Figure 1-3 Shows (a) RGB image, (b) location, (c) classification map of a specific probability of detection and (d) reflectance graph (reflectance versus wavelength (μm)) in Visible-near infrared (VNIR) of three look-alike red Astra car panels. The hyperspectral imaging system is capable to distinguish three different panels by exploiting more detailed spectral information other than the RGB bands.

HSI systems represent an evolution in imaging technology from earlier multispectral imaging (MSI) systems. Multispectral imaging systems commonly employ about 10-20 discrete bands covering visible, Near Infrared (NIR), SWIR, MWIR and LWIR regions. As these systems employ discrete bands, and therefore they are not able to produce detailed signatures of targets due to the insufficient spectral resolution.

HSI systems have been developed through the advancement in sampling the reflective electromagnetic spectrum spanning from visible region (VIS) all the way to LWIR region in narrow contiguous bands (about 10 to 30 nm wide) in every pixel of a scene. HSI differs from MSI in that the number of bands utilized in HSI is much higher (about 100 or more) and that the spectral bands are contiguous.

1.3.2 Hyperspectral Images

HSI image cube consists of spatial and spectral information as illustrated in Figure 1-4. Spatial information is normally presented in the x and y axis and the spatial width are dependent on the field of view (FOV) of the system (9). Spectral information is presented in the z axis and the resolution is dependent on the spectral sampling capability of the system (9). One way to present hyperspectral data is to make a composite image using three carefully chosen spectral bands. However, choosing the most appropriate three channels from HSI cube is not a straightforward task. Nevertheless, a set of three bands similar to those used in the conventional RGB images are often adopted for simple display of hyperspectral imageries (10). After appropriate processing, the spectral vector in each pixel can be used for target detection and classification as shown in Figure 1-5.

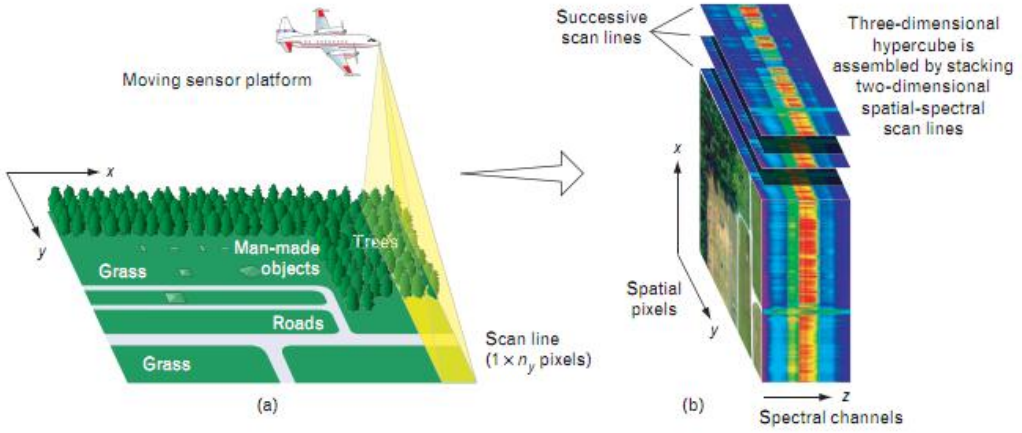

Figure 1-4 A sample of a 3D HSI cube consists of spatial pixels in the axis x and y with spectra channels in the z direction. (b) The comparison of the 'reflectance' of a sample collected by MSI (top) and HSI (bottom) (9).

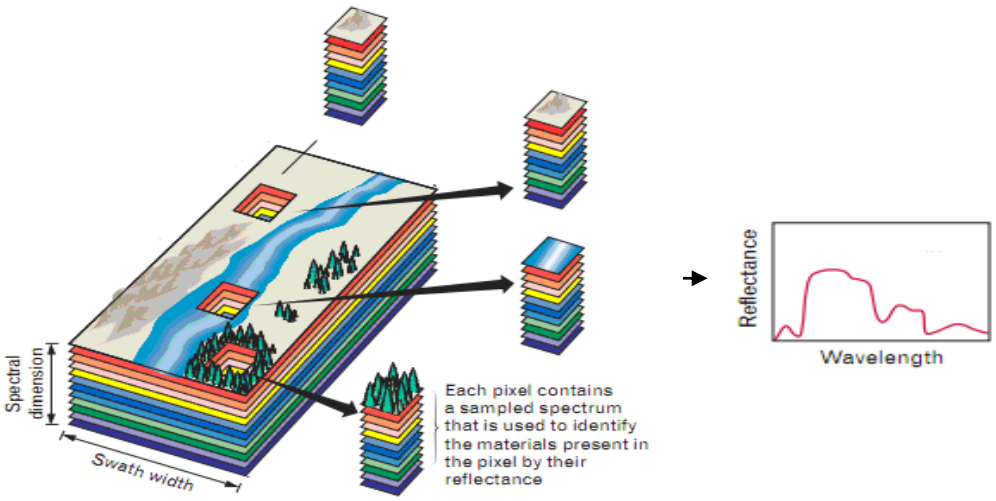

Figure 1-5 Each pixel in the image can be plotted as the reflectance of targets in each waveband. This reflectance or spectral signature of targets can then be interpreted for target detection or classification (9).

The ultimate goal of HSI is to detect and classify any interesting objects in the scene based on the spectral characteristics of the target reflectance signature. An overview of detection and classification methods will be outlined in Chapter 2. Suppose that there are 3 types of classes consisting of soil, water and vegetation with spectral signatures within the visible to near infrared region as given in Figure 1-6. However, the spectral signature of a given objects is not

represented by a single spectra but by a family of spectra as shown in Figure 1-7 due to the variability of natural substances. This variability is partly due to the atmospheric and sensor effects that hamper the retrieval of target reflectance accurately. All these factors make the separation of classes much more difficult in practice. Hence pre-processing algorithm to compensate all these factors is needed in order to improve the integrity of the spectral characteristics of HSI data thus to improve the detection and classification accuracy. This pre-processing step will be briefly reviewed in Chapter 3.

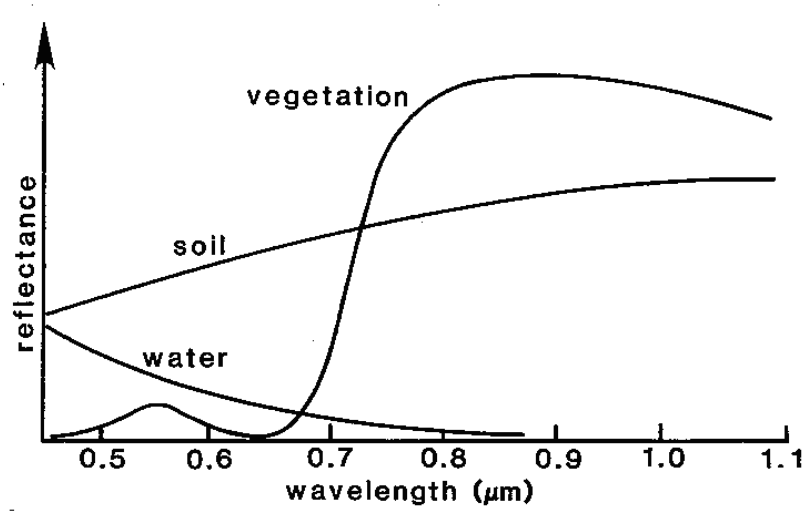

Figure 1-6 An example of spectral signature for soil, water and vegetation (50).

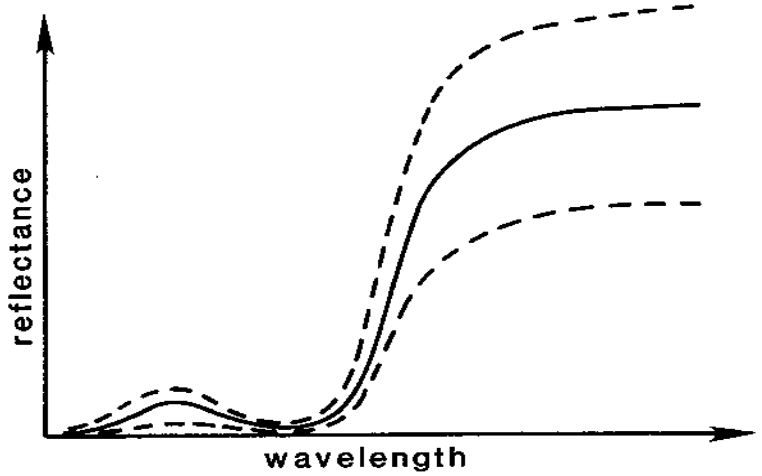

Figure 1-7 Typical variation of reflectance for vegetation (50) due to the variability of natural materials.

Apart from the factors as mentioned above, illumination effects such as shadowing also affect the accuracy of retrieving intrinsic spectral property such as reflectance of objects from the scene in remote sensing. Shadow effects distort the intrinsic optical characteristic and therefore it is crucially important to compensate this undesired shadowing effect in order to improve the target detection and classification (10). This is the main concern of this research. Three new methods of shadow compensation, namely Diffuse Irradiance Compensation (DIC), Linear Regression (LR) and Spectro-polarimetry (SP) technique have been proposed. The details of each method are outlined in Chapter 6, 7 and 8.

2 AN OVERVIEW OF DETECTION AND CLASSIFICATION ALGORITHMS

This chapter presents an overview of the theoretical and practical issues of detection and classification algorithms for hyperspectral imagery processing. The basic idea of HSI stems from the fact that different materials will exhibit variable amounts of wavelength dependent reflection, absorption or emission (11). This spectral characteristic can be used as signature for the detection and classification of the scene.

2.1 Detection Overview

There are two main types of detection algorithms in HSI processing, namely anomaly detection (AD) and matched filter (MF) detection. The former is the detection technique that identifies pixels different from the background without prior information (12). The latter is a detection technique based on prior information of targets, i.e. spectral signatures of targets. This type of detection aims to locate the pixel vectors that match the targets signature as much as possible (13).

2.1.1 Anomaly Detection

Anomaly detection is a technique that locates and identifies the uncommon pixel vector compared to the ‘norm’ of the background model. If an observed pixel spectra differs from the ‘norm’ of the background then the deviation is measured using a distance metric to represent the degree of anomaly. The distance metric normally used in anomaly detection was derived by Iriving Reed and Xiaoli Yu (RX) in 1990 (13). Yu and Reed developed the algorithm under the Generalized Likelihood Ratio Test (GLRT) framework for multidimensional image data. This assumes that the spectrum of the target and the covariance of the background are Gaussian distributed and that they are generally unknown (13-15).

By denoting a background model as B, a distance measure as $d(.)$ and a threshold as t, pixel x is regard as an anomaly if (16):

$$D_{RX}\left(\langle x|B\rangle\right)=\left[d(x,B)>t\right]=\left[(x-\hat{\mu})\hat{\Sigma}(x-\hat{\mu})>t\right] \quad \textbf{(2-1)}$$

Where

$$\mu=\frac{1}{N}\sum_{n=1}^{N}x(n) \quad \textbf{(2-2)}$$

and

$$\Sigma=\frac{1}{N}\sum_{n=1}^{N}(x(n)-\mu)(x(n)-\mu)^{T} \quad \textbf{(2-3)}$$

In equation (2-1) the distance between each pixel signature to the background signature is calculated using Mahalanobis distance (16) in the RX formulation. Here, the background is modelled as a multivariate Gaussian distribution (16). Hence, in AD it is the model of the background which is needed for the identification of uncommon pixels. There are various techniques reported for characterizing the background, such as the employment of local or global windowing, target removal or clustering.

2.1.2 Spatial Subsetting

The employment of local or global windowing has been one of the simplest methods for background characterization and it is commonly known as spatial subsetting. There are two types of local windowing: one is the local spatial subset and the second is the spatial scene subset (globally) (17) as shown in Figure 2-1. The local mode is commonly implemented using two concentric sliding windows. The mean and covariance of the background are extracted from the outer window while excluding the inner one. This is called Local RX (LRX) (6). The global mode denoted as Global RX (GRX) which uses one sliding window that takes large section of the imagery (13) and the Mahalanobis

distance of every test pixel is evaluated sequentially according to equation (2-1). Global Mean RX (GMRX) models the background by utilizing the whole image to calculate the mean and covariance of the background and it is more suitable for real time detection work than LRX method.

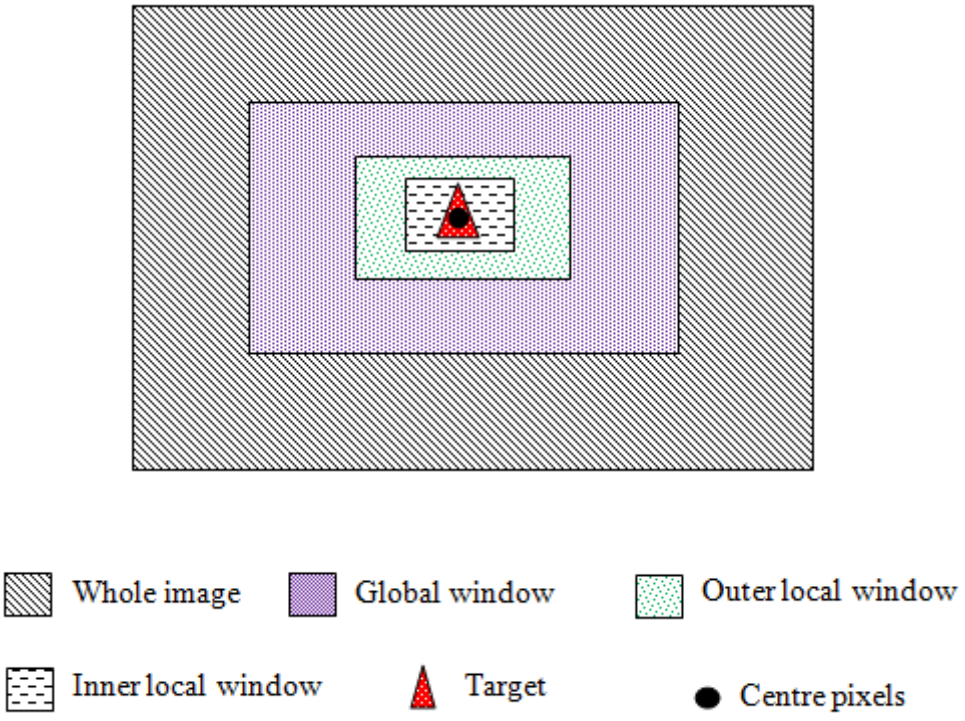

Figure 2-1 Graphical presentation of spatial subsetting in HSI images.

2.1.3 Target Removal

Studies have shown that the background covariance can be affected significantly if 0.02% of target pixels have been included in the background characterisation (18). The background characterisation can be improved by removing these target pixels through an iteration of processing where potential target pixels can be sequentially removed from each cycle. This can be achieved simply through iterated target detection process where a percentage of the detected targets in the previous run are excluded in the subsequent run (18). For example, this can be implemented together with Global RX and the combination of these methods is called Iterated Global RX or IGRX (12). Normally in IGRX, the Global RX will be performed iteratively where the target

pixels will be detected by loosely thresholding the GRX in the first few rounds of detection (12). Then, these target pixels are subsequently excluded in the next iteration of detection. This process will be repeated until the IGRX detection performance does not change significantly with respect to the previous run. Alternatively, the target pixels can be found by using other algorithms, such as spectral unmixing (19), as the first round of target detection.

2.1.4 Spectral Subsetting

All the detection algorithms mentioned in the above sections are based on the assumption that the HSI data conforms to multivariate Gaussian distribution. However, it is found that the real world HSI imagery generally consists of fat tail containing high order statistics (12, 18). One way to circumvent this is to classify the non-Gaussian HSI data into more Gaussian-like clusters. This can be achieved by using Gaussian Mixture Model classification such as K-means clustering or Stochastic Expectation Maximization (SEM) classification (18). K-means technique is applied by classifying or grouping the objects based on the spectral features into K classes. The feature refers to the mean of the class and is calculated by minimizing the sum of squares of distances between each pixel to the corresponding mean. While for SEM, the features refer to the mean and the covariance of the classes. Both K-means and SEM aim to generate class or cluster maps for the scene. Then, the detection is applied by finding the anomalous pixels that is least likely to fall into each class (20).

2.1.5 Matched Filter Detection

Matched filter detection is a well-developed technique that uses a known target spectral signature or target probe to search for the presence of that spectrum in a scene (21). It attempts to detect and locate pixels containing a target signature by modelling the scene background as unstructured or stochastic. This takes the form of first and second order spectral statistics (mean, μ and covariance, Σ) estimated from the HSI data of the scene like that performed in the anomaly detection.

The adaptive matched filter (AMF) is a detector that models and suppresses a background (21) and then uses a known target spectrum, denoted as *s*, to search for that in the scene. The pixel x is classified as target classes, C if (16)

$$D_{AMF}\left(x|B,C\right)=\left[\frac{\tilde{s}^{T}\tilde{x}}{\|\tilde{s}\|^{2}}\right]>t=\left[\frac{\left(s-\mu\right)^{T}\Sigma^{-1}\left(x-\mu\right)}{\left(s-\mu\right)^{T}\Sigma^{-1}\left(s-\mu\right)}\right]>t \qquad \textbf{(2-4)}$$

This detector is optimum only when the target and background follow a Gaussian distribution and in real applications this is highly unlikely (16).

The adaptive coherence or cosine detectors model the target variability by measuring the angle between the target pixels to the target spectrum. The pixel x is classified as a target pixel if (16):

$$D_{ACE}\left(x|B,C\right)=\left[\frac{\tilde{x}^{T}\tilde{P}_{S}\tilde{x}}{\tilde{x}^{T}\tilde{x}}\right]>t=\left[\cos^{2}\alpha\right]>t \qquad \textbf{(2-5)}$$

Where $\tilde{P}_S$ is the projection and reconstruction operator onto the target subspace $\tilde{\Phi}$ s , that is

$$\tilde{P}_{S}=\tilde{\Phi}_{S}\left(\tilde{\Phi}_{S}^{T}\tilde{\Phi}_{S}\right)^{-1}\tilde{\Phi}_{S}^{T} \qquad \textbf{(2-6)}$$

and α is the angle between the target subspace and the test vector.

2.1.6 Performance Measure

The performance of the detection in remote sensing is commonly assessed through a projection of detection result onto a map as illustrate in Figure 2-2, which displays the detected pixels over the ground truth target map for a specific probability of detection and the associated probability of false alarm rate. This will provide the reader with an intuitive image of the detection result. Alternatively, the Receiver Operating Characteristic (ROC) has been another and more effective way to present the performance of the detector. The ROC can be assessed in Pixel Based Graph (as in Figure 2-3 (a)) that counts every

detected pixel for various false alarm rates, while the Target Based Graph (as in Figure 2-3 (b)) counts the number of the detected target. The ROC graph shows the detector performance by plotting the probability of detection (PoD) versus Probability of False Alarm (PFA), where the ideal case is to have the highest PoD with the lowest PFA. By using both pixel based and target based ROC, the efficiency of the detector can be assessed more accurately.

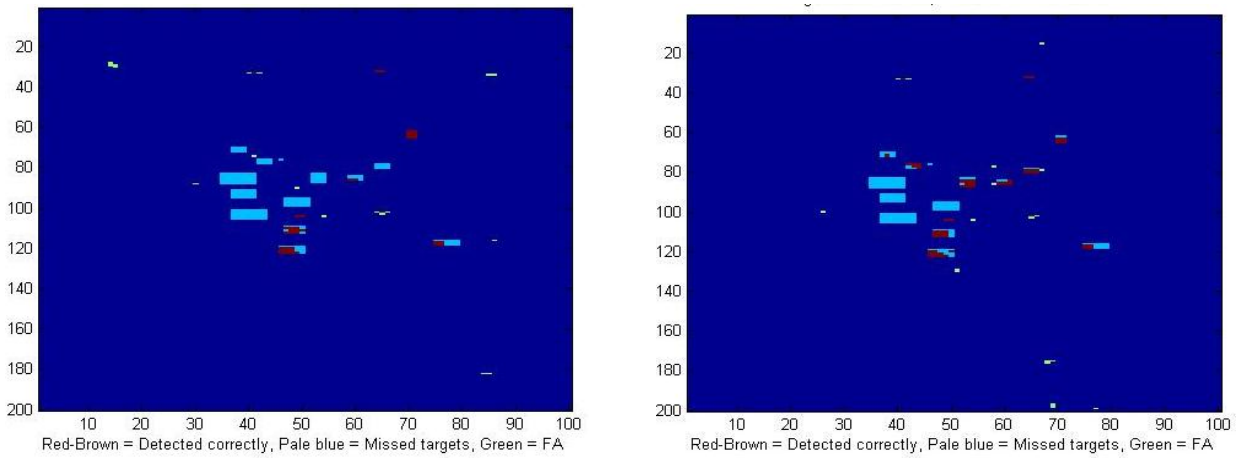

(a) **(b)**

Figure 2-2 shows an example of displaying the detected pixels over that of the ground truth target maps at a specific PFA.

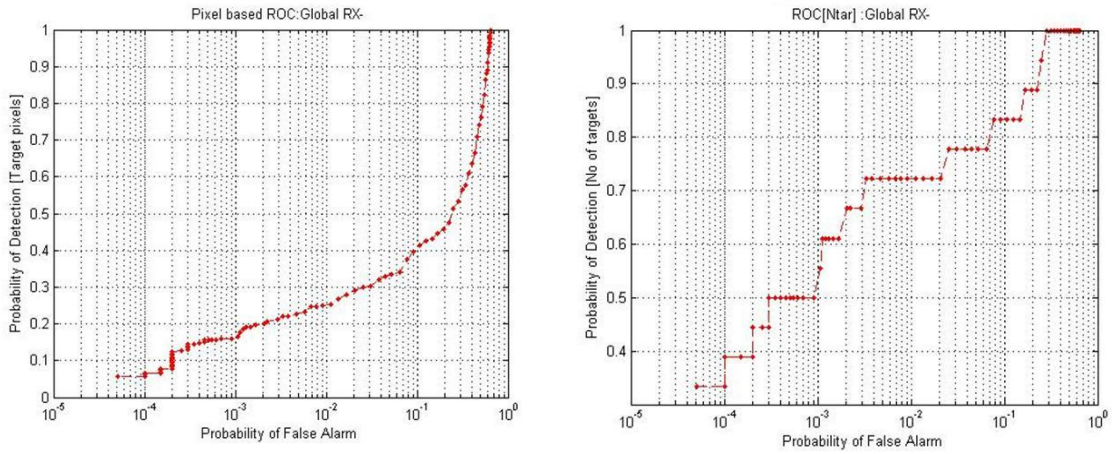

(a) **(b)**

Figure 2-3 shows an example of (a) pixel based ROC and (b) indicates the target based ROC.

2.2 Classification Overview

Classification on hyperspectral imageries normally adopts a non-literal processing which exploits mostly spectral information rather than spatial (21). Each pixel in each band of the HSI imageries consists of specific reflectance or radiance which can be labelled into specific classes by matching the distance between the characteristics of each pixels with respected to the training data, as shown in Figure 2-4. The assignment of a pixel into any particular class is commonly based on the statistical intelligent which is associated with the probability of error. There are two types of classification, namely supervised and unsupervised. Supervised classification is a discriminate classifier that uses class information whereas unsupervised classification clusters the groups without the class information (22). For the purpose of this thesis we will concentrate on supervised classification using a parametric classifier via Bayes' theorem. Figure 2-5 shows a diagram of the classification taxonomy.

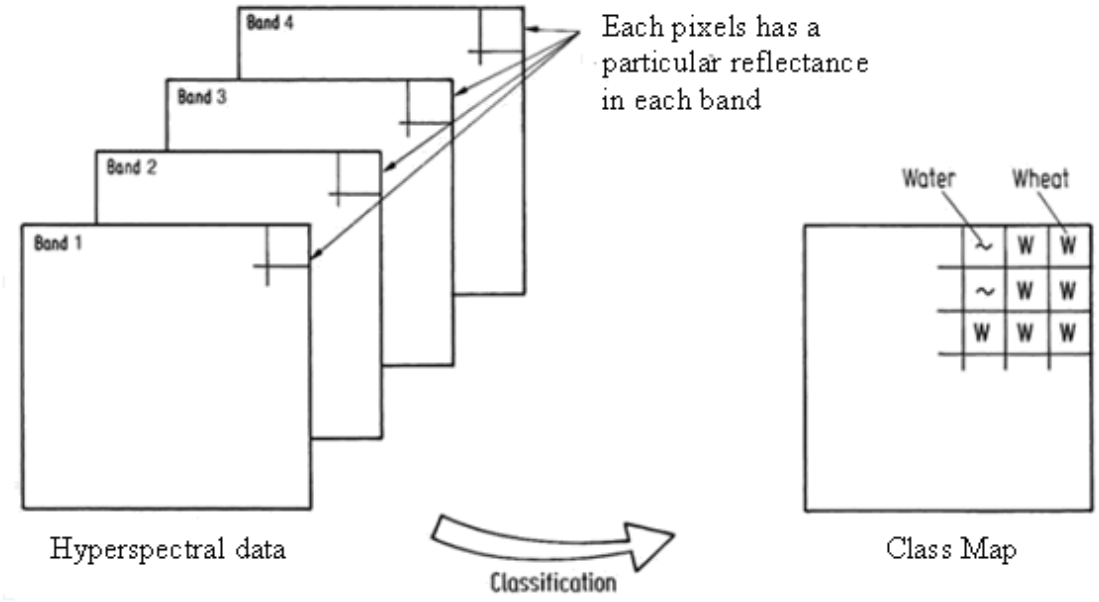

Figure 2-4 The role of classification in labelling the hyperspectral data (22).

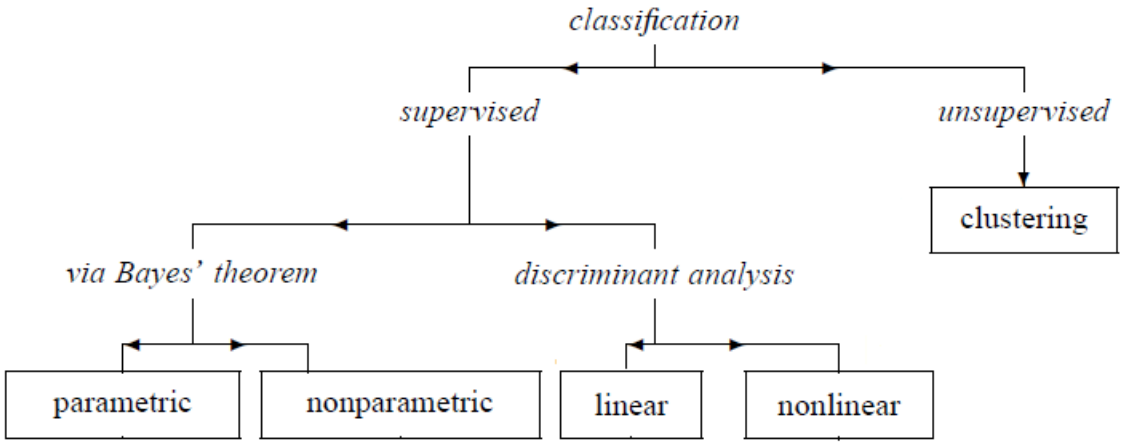

Figure 2-5 Diagram of classification taxonomy (22).

2.2.1 Parametric Classifier via Bayes' Theorem

Parametric classifier utilises a statistical approach to classify the object of interest to specific classes based on their spectral properties. These specific classes that contains known spectral signature are associated with a specific label. An important assumption in a statistical approach to classification is that each spectral class can be described by a probability distribution in spectral space such as normal or Gaussian distribution (22).

Given L number of training data, a posteriori probabilities that the pixel x belongs to class i can be calculated with Bayes Rule:

$$p(i|x) = \frac{p(x|i)p(i)}{p(x)} \quad \textbf{(2-7)}$$

Where

$$p(x) = \sum_{i=i}^{L} p(x|i)p(i) \quad \textbf{(2-8)}$$

A decision rule to assign pixel x to one of the L number of classes can be achieved using equation (2-7). For example, based on the Figure 2-6, let the number of class is equal to 2, the Bayes decision rule can easily be interpreted such that (49):

a pixel x belongs to class 1 if $p(x|1)p(1) > p(x|2)p(2)$

a pixel x belongs to class 2 if $p(x|2)p(2) > p(x|1)p(1)$

a decision cannot be made if $p(x|1)p(1) = p(x|2)p(2)$

The equation (2-7) is also called as discriminant function and is denoted as g_i. This discriminant function can be rewritten in a logarithmic form (22):

$$g_i = \log(p(x|i)) + \log(p(i)) \quad \textbf{(2-9)}$$

The error of the classification is given by the area under the overlapping portions of the posteriori probability as in Figure 2-7. Note that in this figure, the crossover line indicate the decision boundary; which to the right indicate the pixel x belongs to class 2 and to the left the decision favour class 1.

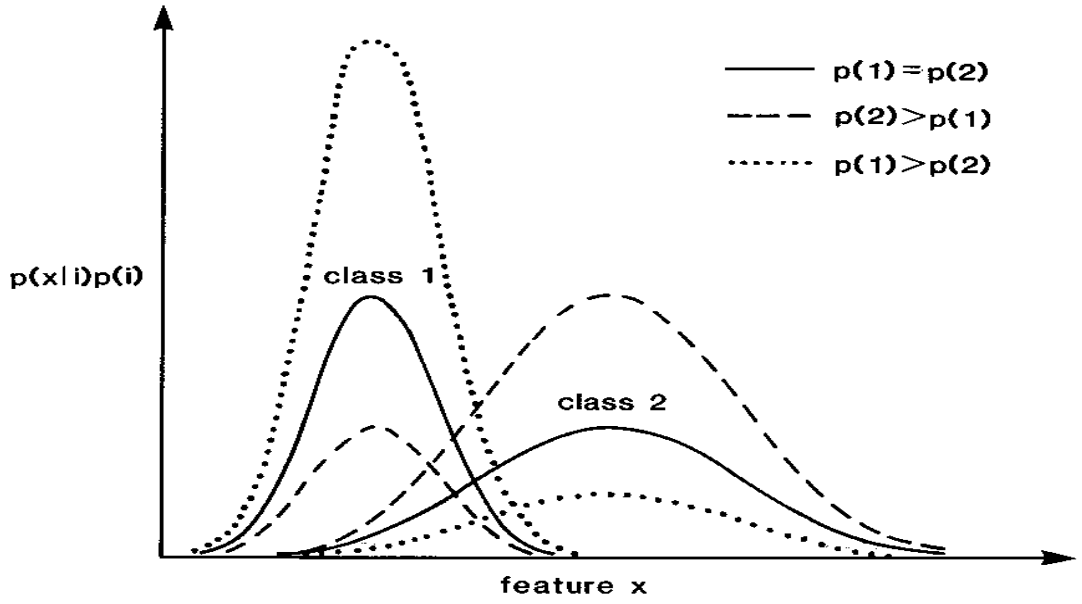

Figure 2-6 The effect of the a priori probability on class probability density function (49).

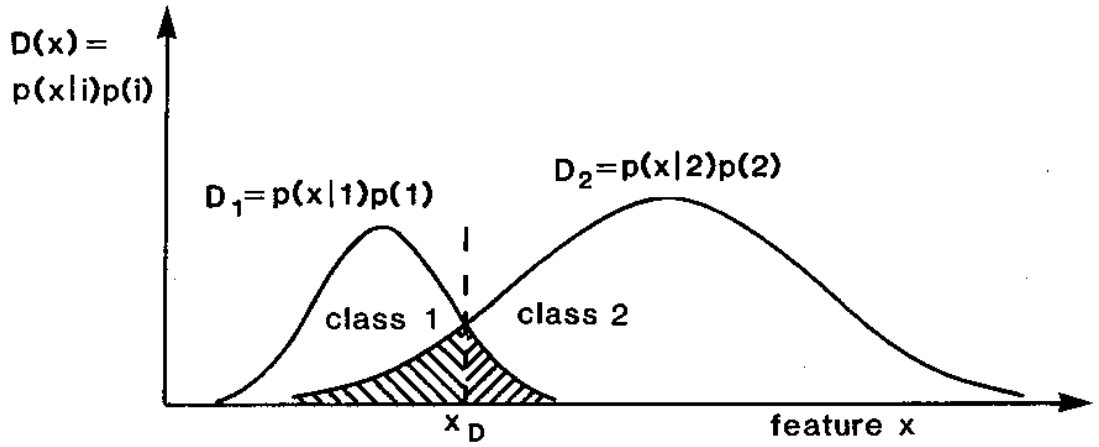

Figure 2-7 shows the discriminant function for the Bayes optimal partition between 2 classes and the probability of error (49).

2.2.2 Quadratic Likelihood Classifier (QD)

In hyperspectral images that consist of *N* number of bands, the probability functions, $p(x|i)$ becomes a multivariate functions, $p(X|i)$. The general multivariate form for N-dimensional normal distribution is given as (49):

$$p(X|i)=\frac{1}{(2\pi)^{\frac{N}{2}}|\Sigma_i|^{\frac{1}{2}}}\exp\left\{-\frac{1}{2}(X-m_i)^T\Sigma_i^{-1}(X-m_i)\right\} \quad \textbf{(2-10)}$$

Where X = pixel feature vector

m_i = mean vector for class i

Σ_i = $N \times N$ symmetric covariance matrix for class i

So the Bayes discriminant function for class i is then (49):

$$g_i=\log(p(i))-\frac{N}{2}\log(2\pi)-\frac{1}{2}\log|\Sigma_i|-\frac{1}{2}(X-m_i)^T\Sigma_i^{-1}(X-m_i) \quad \textbf{(2-11)}$$

The Quadratic Likelihood Classifier class partition is defined by equation (2-11) and the decision is depended on the relations between the means and

covariance matrices of different classes. The values for μ and Σ are estimated from a set of training sample, given as $\{x_1.....x_n\}, x_j \in \Re^N$

Therefore,

$$m_i = \frac{1}{N}\sum_{i=1}^{N} x_i \qquad \textbf{(2-12)}$$

And

$$\Sigma_i = \frac{1}{N}\sum_{i=1}^{N} (x_i - m_i)(x_i - m_i)^T \qquad \textbf{(2-13)}$$

As this classifier measures both the mean and the covariance it has been proven to be one of the most effective classification methods within the HSI community. However, the sample size of the training data must be sufficiently large enough to achieve a well characterised covariance for each class to minimise misclassifications (22).

2.2.3 Fisher Linear Discriminant (FD)

The minimum distance classifier assign the feature vector X to class whose mean vector, m_i, is closest to X. If we assume that the covariance matrix are equal for all classes, i.e. $\Sigma_i = \Sigma_j = \Sigma_0$ and the a priori probabilities are equal, i.e. $p(i) = p(j) = p(0)$, the discriminate function of equation (2-11) becomes (49):

$$g_i(x) = -\frac{1}{2}(X - m_i)^T \Sigma_0^{-1}(X - m_i) \qquad \textbf{(2-14)}$$

Equation 2-14 is known as Mahalanobis Distance or Fisher Linear Discriminant classifier (FD). A pattern is classified by finding the minimum distance from the normalised mean.

2.2.4 Minimum distance Classifier (MD)

If the covariance matrices of all classes are assumed to be diagonal and have equal variance along each feature axis, i.e.

$$\Sigma_i = \begin{pmatrix} \sigma^2 & 0 & 0 \\ 0 & \sigma^2 & 0 \\ 0 & 0 & \sigma^2 \end{pmatrix}$$

Therefore, the covariance is merely σ^2 times the identity matrix, I (22), i.e. $\Sigma_i = \sigma^2 I$ and $\Sigma_i^{-1} = \left(\frac{1}{\sigma^2}\right) I$. So the discriminant function becomes:

$$g_i(X) = \log(p(i)) + \frac{\|X - m_i\|^2}{2\sigma^2} \qquad \textbf{(2-15)}$$

The quantity $\|X - m_i\|^2$ is a scalar that can be expanded as:

$$d_i{}^2 = \sum_{n=1}^{N} (x_n - m_{n,i})^2 \qquad \textbf{(2-16)}$$

This scalar is simply the square of the Euclidean distance between vector X and the mean, m_i. Therefore this of classifier is called the Minimum Distance Classifier (MD) or Euclidean distance classifier (ED).

3 RADIOMETRIC DISTORTION

The radiant energy that is sensed by a hyperspectral system can generally be separated into two components: one is the radiant energy reflected or transmitted by objects due to irradiance sources such as solar or artificial light; and the second one is the radiant energy due to self-emissions from the objects (24). These radiant energies propagate through the atmospheric medium before reaching the sensor. Therefore, it is important to measure all these components in order to obtain accurate reflectance or spectral signatures of targets. This is especially the case when dealing with electromagnetic propagation and transmission through the atmosphere. Factors such as atmospheric scattering and absorption, direct and diffuse solar irradiance, reflectance of adjacent targets and bidirectional reflection differential effect may distort the assessment of absolute reflectance.

3.1 Atmospheric Effects

When solar radiation propagates through the atmosphere it is affected by two important mechanisms: absorption and scattering. Absorption by molecules in the atmosphere is a quantum process that changes the molecules internal state, increasing the energy and resulting in a temperature change (25). Figure 3-1 shows the energy structure of a molecule. For a photon to be absorbed by a molecule, the photon energy, E_{photon} must be higher than the molecular energy bandgap, E_g. The energy of photon is given by Einstein equation:

$$E = h\nu \qquad \textbf{(3-1)}$$

Where *E* is the energy of the photon, *h* is the Planks' constant (6.626 x 10^{-34} J-sec) and ν is the frequency of the incident light. Because of this quantum mechanism, the absorption is not significant within the visible band except for H_2O absorption between 0.65 and 0.85 um. However, absorption has a strong affect within the thermal infrared region. There are approximately 30 different species of gases in atmosphere but only 7 of them, namely water vapour (H_2O), carbon dioxide (CO_2), ozone (O_3), nitrous oxide (N_2O), carbon monoxide (CO),

methane (CH_4) and oxygen (O_2), produce appreciable absorption features in the thermal region (26). The spectral regions in which absorption does not occur due to these gases are called atmospheric windows. Several atmospheric windows exist in the range between 0.4 and to 2.5 μm (26), as shown in Figure 3-2. In the absence of atmospheric absorption the radiation transmittance should be 100% but this is not generally the case. Hyperspectral data should be collected within these atmospheric windows because outside these windows the radiation transmittance will be significantly reduced due the atmospheric absorption.

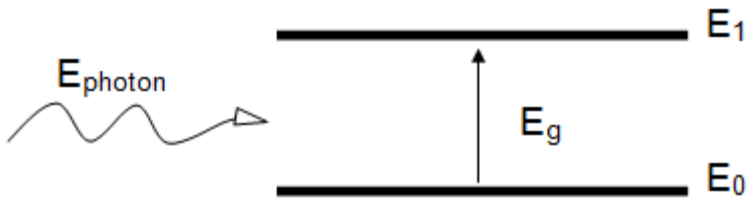

Figure 3-1 The energy structure for molecule (25).

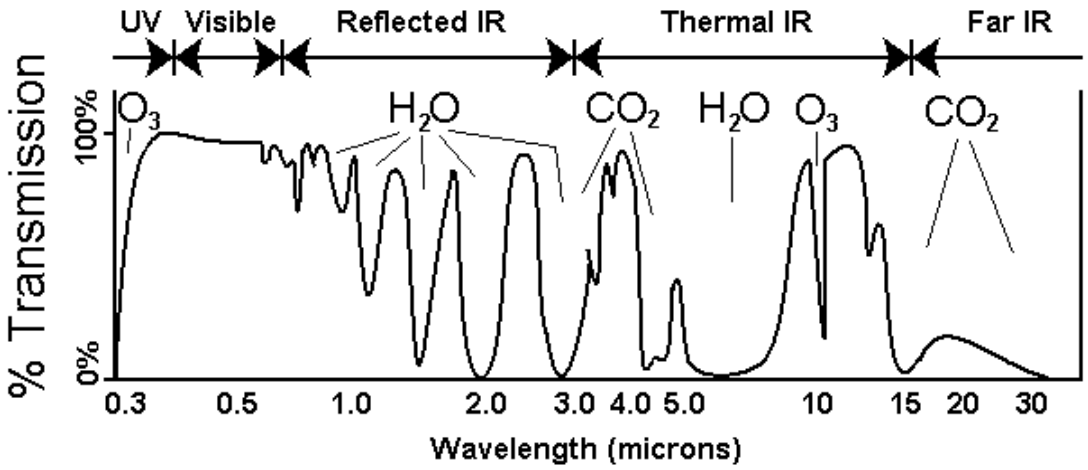

Figure 3-2 Diagram of the atmospheric windows – spectral regions in which solar radiation is able to transmit through the Earth's atmosphere. Chemical notation indicates the gas molecules that are responsible for the atmospheric absorption at particular wavelength (27).

In the visible wavelengths the major scattering in the atmosphere is due to gas molecules and water vapour. There are three forms of atmospheric scattering: Rayleigh scattering, Mie scattering and Geometric optics model as illustrated in Figure 3-3. Rayleigh scattering occurs when the solar radiation interacts with molecules that have size less than one-tenth of the EM wavelength (25). Example of such particles could be air molecules and haze particles or some of the molecules of atmospheric gas such as nitrogen (N_2) and oxygen (O_2) (52). Rayleigh scattering is wavelength dependant and is inversely proportional to the fourth power of wavelength function. Therefore scattering is much higher at shorter wavelengths.

Mie scattering or aerosol scattering occurs when the particles are comparable in size to the radiation wavelength, such as dust, pollen, smoke and fog droplets. Like that of the Rayleigh scattering, Mie scattering also influence a broad range of wavelengths in the visible spectrum. However, this scattering tends to be the greatest in the lower atmosphere where large particles are abundant.

The third type of scattering is non-selective and it is also known as Geometric optics model scattering that occurs when the particles are larger than the wavelength such as the rain drops (25). This scattering causes the light to be scattered primarily in the forward direction. Because of these scattering effects, the radiation may reach the sensor field of view before it reaches the ground. This radiation component is called path radiance and can also be caused by the diffuse reflectance from the ground to the sensor. Figure 3-4 shows the path radiation, component 1, which scatters along the path up to sensor field of view and component 2, which is the light scattered and reflected from the ground.

After the light passes through the atmosphere it will reach the surface of targets and will be reflected in two ways: directly or diffusely as illustrated in Figure 3-5. The surface or targets will reflect the radiation partially in the form of direct reflection and partially in the form of diffuse reflection, regardless of the direction of the incoming radiation (29). Direct reflection is when the incoming radiation angle is normal to the plane of the reflected radiation angle and is reflected only in a single direction (30). This type of reflection is sometimes

called specular reflection. Diffuse reflection relates to scattered light where the irradiation is reflected in many angles (31). If the reflected angles are equal in all directions then the surface is termed a Lambertian source (32). Some reflected energy from the ground, either direct or diffuse, may affect the pixel quality as recorded by the HSI system in two ways. One is the energy of the light source is diffusely scattered by the particles of the atmosphere which is then radiated towards the targets and subsequently is reflected towards the sensor field of view. This component is denoted as sky irradiance component 1 in Figure 3-4. The second type is the light that diffusely scattered by adjacent objects and illuminates the targets, and then reflected upward to the sensor field of view. This is denoted sky irradiance as component 2 in Figure 3-4.

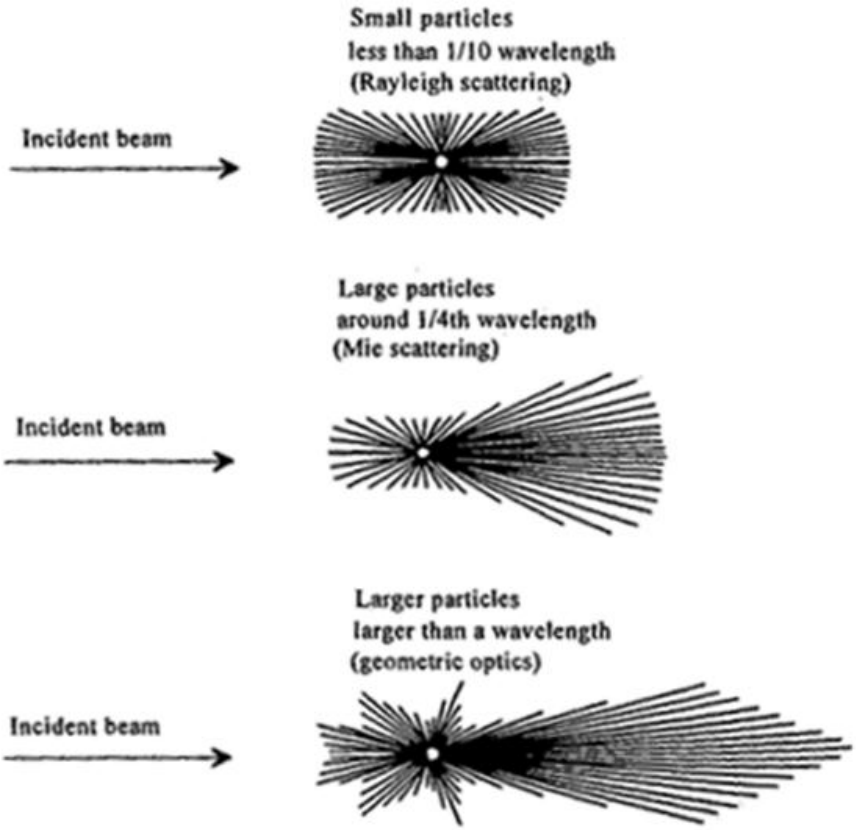

Figure 3-3 Represents three types of scattering; Rayleigh scattering, Mie scattering and Geometrical optic model (25).

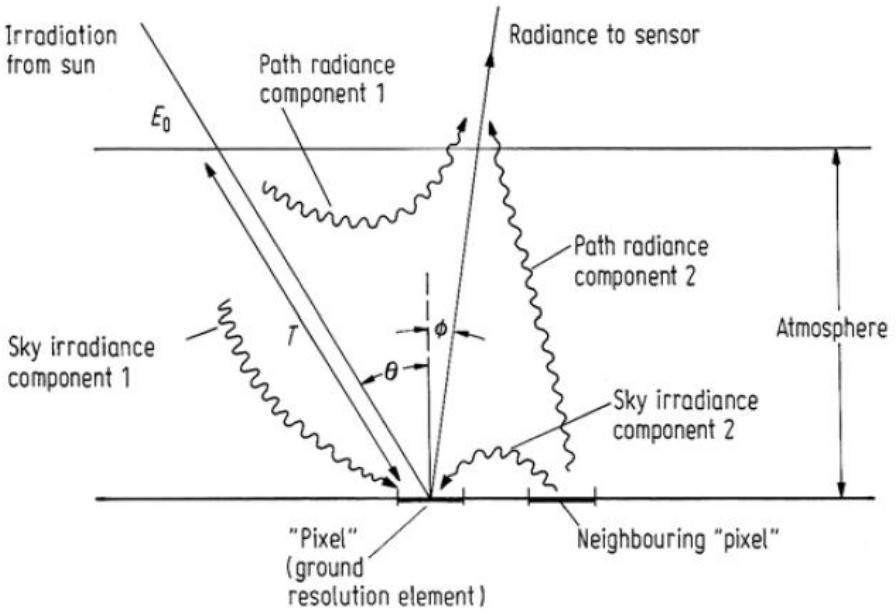

Figure 3-4 Effect of the atmosphere in determining various paths for energy to illuminate a (equivalent ground) pixel and to reach the sensor (27).

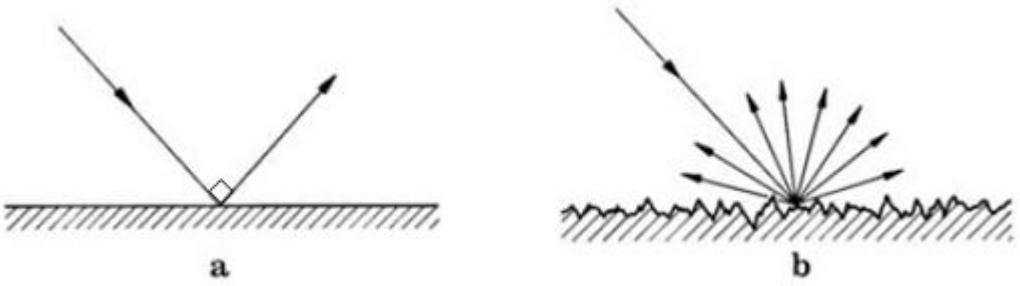

Figure 3-5 (a) Direct and (b) diffuse reflection (27).

The combined effects of these atmospheric scattering will make the assessment of intrinsic reflectance of objects in a real remote sensing scenario very difficult. To compensate for these effects, atmospheric correction is essentially needed for a better estimation of target reflectance and spectral signature from HSI imageries.

3.2 Atmospheric Correction

Atmospheric correction aims to compensate for the effects of atmospheric absorption and scattering, as well as illumination angle artefacts on hyperspectral imageries, by converting the radiance at the sensor to the reflectance of the target surface (20). There are three types of atmospheric correction methods (33, 34, 35 and 36): scene based empirical approach, model based and hybrid based. Scene based empirical approach was the first atmospheric correction that was developed during 1980s. Several examples of scene based empirical methods are the Internal Average Reflectance (IAR) (37, 38), Flat Field (FF) (39, 40), Single Spectrum Method (SS) (41) and Empirical Line Method (ELM) (42, 43 and 44).

In the late 1980s the first model based correction method, called Atmosphere Removal Algorithm (ATREM), was introduced (26). This was then followed by Atmospheric and Topographic Correction (ATCOR) (45), the Fast Line-of-Sight Atmospheric Analysis of Spectral Hypercubes (FLAASH) (46) and High-Accuracy Atmospheric Correction for Hyperspectral Data (HATCH) (47). For the hybrid approach, researchers have used combinations of radiative modelling approaches together with empirical approaches to estimate the surface reflectance on HSI imageries (36, 48), such as the combination of ATCOR and ELM (45). The selection of the atmospheric correction method depends on the data quality, availability of radiometric calibration and atmospheric parameters, a priori knowledge of the scene and ground spectral measurements (37). For the purpose of this study several methods of empirical approach and model based correction method, such as ATCOR, will be explained in more detail.

3.2.1 Empirical Line Method (ELM)

The Empirical Line Method (ELM) employs field reflectance measurements of the scene to calculate the targets apparent reflectance. The word ‘apparent’ used in the ELM approach does not consider other possible effect, such as the topography of the scene, for the estimation of target reflectance. Given an at

sensor raw image as DN, the linear equation for the radiance conversion is given by

$$L = d^2(c_o + c_1 DN) \quad \textbf{(3-2)}$$

Where c_o and c_1 are the calibration coefficients for the offset and slope respectively, d is the distance between the light source and the target and it is commonly assumed to be 1, DN is the digital number of the at sensor measurement. When the downwelling radiance and the reflectance of two standard calibration panels are presented in the scene, the two coefficients c_o and c_1 can be found. To measure the offset and slope, at least two calibration panels (white and black spectralon) are placed in the scene. From the mean spectra of both calibration panels the ELM method generates the linear fit to solve for gain and offset according to equation (3-2) and schematically as shown in Figure 3-6. The reflectance, ρ, for at-sensor radiance, L, can be computed for each pixel in each band using (27)

$$\rho = c_1(L - c_0) \quad \textbf{(3-3)}$$

The term of c_1 is equal to the atmospheric effect. This method will yield poor result if the standard calibration panels do not represent the 'true' radiance of the scene. Very often equations 3-2 and 3-3 are combined into one step:

$$DN = \rho(\lambda)A_b(\lambda) + B_b(\lambda) \quad \textbf{(3-4)}$$

where A_b and B_b are the multiplicative and additive terms which comprises of atmospheric transmission and instrumental factors.

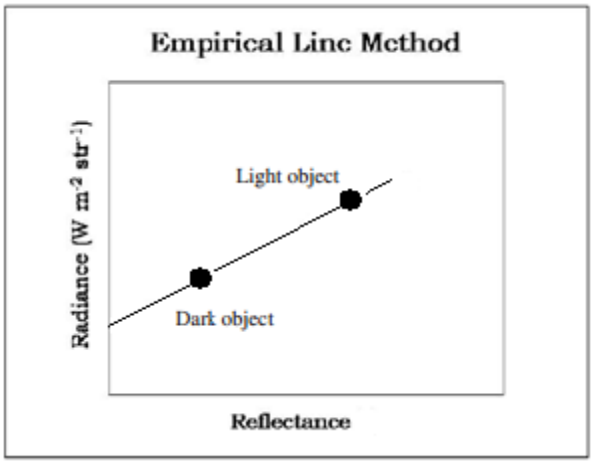

Figure 3-6 ELM representation (21).

3.2.2 Flat Field Conversion

This type of radiance to reflectance conversion is an image based method as it requires the ability to identify flat field materials in the scene. The mean spectrum for that area will be used to convert the radiance image into 'relative reflectance' by (39):

$$\rho = \frac{DN - DN_D}{DN_w - DN_D} \quad \textbf{(3-5)}$$

Where DN = each pixels image in each bands

DN_D = mean spectra of dark flat field target

DN_W =mean spectra of bright flat field target

Since a perfect dark pixel has zero reflectance in one or all bands the conversion of radiance to reflectance values can be simply accomplished using

$$\rho = \frac{DN}{DN_w} \quad \textbf{(3-6)}$$

3.2.3 Internal Average Relative Reflectance (IARR)

Internal Average Relative Reflectance (IARR) extracts the spectral information from the raw data by measuring the mean spectrum of the whole image (37). Every pixel vector is normalised by this global spectral mean to produce a 'relative reflectance' image. Given x as the pixels, $i*j$ is the image coordinate location, n is the number of bands and μ_n is the global spectral mean of the whole image for each band, Internal Average Relative Reflectance (IARR) correction method can be defined as:

$$\rho = \frac{x_{i*j,n}}{\mu_n} \quad \textbf{(3-7)}$$

This correction method is normally employed when the atmospheric parameters and ground spectral measurements of the scene is unavailable. Some artifacts which may be mis-interpreted as real spectral features can induce large errors in this atmospheric correction method. Ben-Dor et. al. have suggested to employ subsets of the scene for the mean estimation to avoid inducing artefacts (37).

3.2.4 Atmosphere Removal program (ATREM)

Atmosphere Removal program or ATREM retrieves the scaled surface reflectance from hyperspectral image based on the radiative transfer model (51). This program was developed in the late 1980s by the University of Colorado. First, the solar zenith angle is derived based on the image acquisition time, date and geographic location. Then, this program extracts the water vapour column for every pixels based on the water vapour absorption band between 940 nm and 1140 nm from the image. Then, it assesses the transmission of other atmospheric gases such as water vapour, carbon dioxide, ozone, nitrous oxide, carbon monoxide, methane and oxygen by using Malkos narrow band model based on the 'look-up' table generate from the absorption of water vapour through the Moderate Resolution Atmosphere Radiance and

Transmittance Model called MODTRAN. The apparent reflectance spectra are obtained based on the equation given as (51):

$$L_o(\lambda) = L_{sun}(\lambda)T(\lambda)R(\lambda)\cos(\theta) \quad \textbf{(3-8)}$$

Where $L_o(\lambda)$ = observed radiance at sensor

$L_{sun}(\lambda)$ = solar radiance above atmosphere

$T(\lambda)$ = total atmospheric transmittance

$R(\lambda)$ = surface reflectance

θ = incidence angle

This code, however, is rarely employed for hyperspectral analysis due to its inefficiency for atmospheric correction (51). Advanced features such as spectral smoothing, topographic correction and adjacency effects have not been considered in the ATREM model (37).

3.2.5 Atmospheric and Topographic Correction (ATCOR)

Similar to other model based approaches, Atmospheric and Topographic Correction (ATCOR) uses the MODTRAN atmospheric propagation model to estimate the surface reflectance of the scene on a pixel-by-pixel basis. Given the surface radiance for flat terrain background (Figure 3-7) (45)

$$L = L_p(\theta_v, \theta_s, \phi) + \tau_v(\theta_v)\frac{\rho}{\pi(1-\rho_r)s}\frac{E_g(0)}{} \quad \textbf{(3-9)}$$

Where L = at-sensor radiance for surface reflectance, ρ

L_p = path radiance

τ_v = total ground-to-sensor atmospheric transmission

E_g = global flux of horizontal surface, sum of direct irradiance (E_{direct}) and diffuse irradiance ($E_{diffuse}$)

ρ_r = large scale reference background reflectance determining the effective global flux

s = spherical albedo of the atmosphere, accounts for atmospheric backscattering to the ground

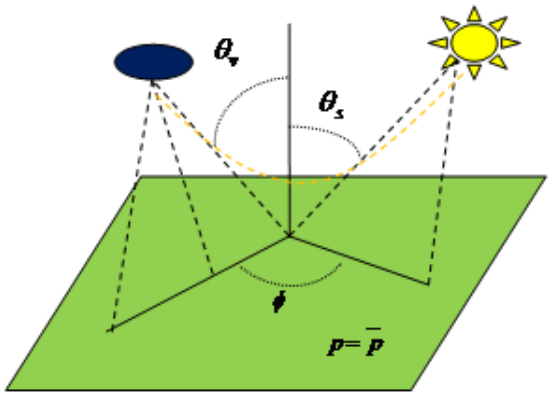

Figure 3-7 Illumination and viewing geometry (ATCOR) (45).

MODTRAN computes the atmospheric transmittance, τ_v, direct and diffuse solar flux, E_g, and path radiance, L_p as functions of viewing and illumination geometry and the solar irradiance (45). The path radiance calculated by MODTRAN is given by

$$L_{path}(\rho) = L_{path}(0) + \frac{\tau_{diffuse} E_g(0)/\pi}{1-\rho_s} \quad \textbf{(3-10)}$$

By setting $\rho = 0$ and $\rho_r = 0.15$, the direct and diffuse solar flux and spherical albedo can be estimated. The result is then stored in a precompiled look-up table (LUT) for further reference. The at-sensor radiance as shown in Figure 3-8 consists of the following components

L_1 = scattered radiance or path radiance

L_2 = reflected energy from the target pixel itself which consists of global flux that is the sum of direct and diffuse irradiance

L_3 = radiation reflected from the neighbouring pixel and scattered into the field of view of the sensor, i.e. the adjacency effect that include the atmospheric backscattering and volume scattering.

So the total radiance signal L received by the sensor can be written as (45)

$$L = L_1 + L_2 + L_3 \quad \textbf{(3-11)}$$

In this case, the surface properties of the target pixels are given by component L_2 and L_1 and L_3 are needed to be removed during the atmospheric correction. L_2 is given by

$$L_2 = L = d^2\left(c_o + c_1 DN\right) \quad \textbf{(3-12)}$$

The radiance of the scene can be estimated using the Empirical Line Method (ELM) approach where c_0 and c_1 are the calibration coefficients (offset and slope). Then the final surface reflectance can be obtained by combining equation (3-12) into (3-9):

$$\rho = \frac{\pi\left[d^2\left(c_o + c_1 DN\right) - L_p\right]}{\tau_v\left(E_g\right)} \quad \textbf{(3-13)}$$

Where L_p = path radiance, L_1

E_g = $E_{direct} + E_{diffuse}$

d^2 = the sun to earth distance (in astronomical units) which is taken as 1 in the atmospheric correction (ATCOR) software (45).

It is seen that the scene based empirical approach has been a simple way for the estimation of surface reflectance in remote sensing. However, this approach

relies on accurate spectral calibration for the estimation of calibration coefficients. To achieve better assessment of surface reflectance the angle dependent path radiance, atmospheric and topographic effects should be taken into account.

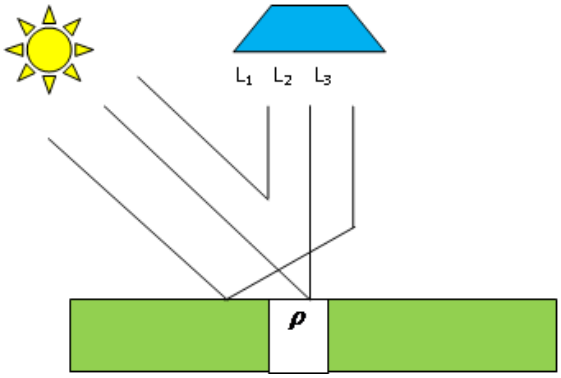

Figure 3-8 Schematic sketch of solar radiation components as seen by the HSI system (45).

3.2.6 Quick Atmosphere Correction (QUAC)

Quick Atmosphere Correction (QUAC) is an advanced method for atmospheric correction (90, 91). This method converts the radiance data to reflectance by locating the near-zero reflectance target to determine the offset or baseline. This baseline is subtracted from the data and the remaining data is used to determine the gain spectrum. The relative gain spectrum is calculated by ratioing the spectral mean of all the endmembers to the spectral mean of each endmember. QUAC will apply the offset and gain linearly such as ELM to derive the reflectance data.

The method only uses information directly from the scene to allow the retrieval of target reflectance even when the data does not have proper radiometric or wavelength calibration, or when the solar illumination intensity is unknown. The underlying assumption of this approach is that there must be a sufficiently low non-zero reflectance for better estimation of baseline. Also, at least 10 diverse materials should be selected in the scene for calculating a reasonable value for the gain.

4 ILLUMINATION EFFECT AND SHADOW

In remote sensing the estimations of upwelling and path radiance have been important factors for the assessment of surface reflectance of the scene. Generally, solar irradiance is the main source of illumination in the outdoor remote sensing applications, while artificial sources such as tungsten or halogen lamps have been commonly deployed for the indoor work. Different types of illumination sources exhibit different spectral power density across the spectrum.

The power density of the illuminations can be assessed directly by using a standard calibration panel such as spectral on which can then be used for reflectance estimation. Spectralon can be made by materials which exhibit diffuse reflectance spanning from zero to 1 independent of the viewing angle.

4.1 Illumination Geometry

The rate at which photons strike a surface is called radiant flux, which is measured in Watts. This unit measures the energy delivered to a surface per unit of time (52). The irradiance of an object is defined as the radiation per unit time (power) impinging on the surface, normalized to the surface area (Wm^{-2}). Radiance is the normalization of irradiance to the solid angle of the observation of the reflected light ($Wm^{-2}sr^{-1}$) (9). Solid angle is the angle subtended at the centre of sphere by an area on the surface of sphere as shown in Figure 4-1. The steradian is defined as (25),

$$\Omega = \frac{A(m^2)}{r^2(m^2)} = \frac{\pi r^2}{r^2} = \pi \qquad \textbf{(4-1)}$$

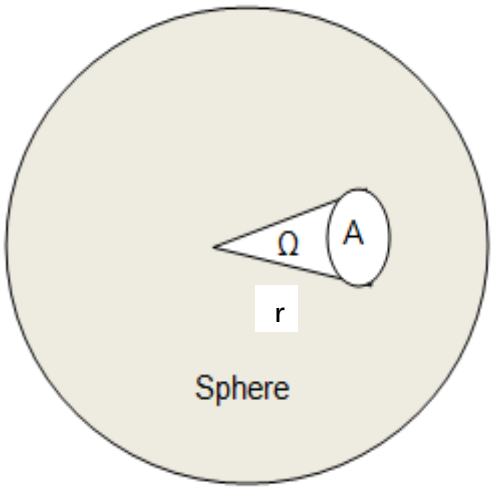

Figure 4-1 Illustration of steradian (25).

Given the sun as the source of illumination, the illumination spectral power distribution, E $(Wm^{-2}sr^{-1})$ is given by,

$$E = S_\lambda \cos\phi_i \qquad \textbf{(4-2)}$$

Where S_λ = Solar Spectral Irradiance $(Wm^{-2}sr^{-1})$

ϕ_i = solar zenith angle (as shown in Figure 4-2)

When the solar radiation hits the surface of an object, the bidirectional reflectance distribution function (BRDF) is given as the ratio of the reflected radiance to incident irradiance (27),

$$BRDF(sr^{-1}) = \frac{L_\lambda(\theta_r,\phi_r)(W/m^2)}{E_\lambda(\theta_i,\phi_i)(W/m^2 sr)} \qquad \textbf{(4-3)}$$

The relationship between the spectral reflectance ρ and $BRDF$ is,

$$\rho_\lambda(\theta_i,\phi_i,\theta_r,\phi_r) = \pi BRDF(\theta_i,\phi_i,\theta_r,\phi_r) \qquad \textbf{(4-4)}$$

Combining equations (4-2), (4-3) and (4-4) gives

$$\rho_\lambda = \frac{\pi L_\lambda}{S_\lambda \cos\phi_i} \qquad \textbf{(4-5)}$$

Equation 4.5 has shown that the illumination and viewing angle can affect the surface reflectance assessment rather significantly.

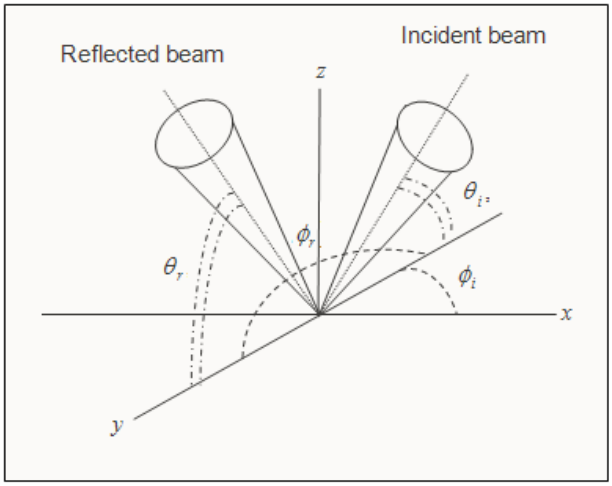

Figure 4-2 Depiction of the BRDF nomenclature (25).

4.1.1 Shading

Shading is a phenomenon caused by the geometry of the object as well as the topology of the scene (32). This effect only appears on Lambertian surface targets such as paints, cloths and wood, not shiny mirror-like objects (25). Shading is defined as the intensity change as a function of the incident I_n and reflected rays, I_r with respected to the surface normal as illustrated in (Figure 4-3 (a))

$$I_r = I_n \cos\theta \qquad \textbf{(4-6)}$$

Note that from equation (4-6) the intensity decreases with increasing angle.

For non-Lambertian (specular) surfaces the light is reflected in a single direction as shown in Figure 4-3 (b). This specular reflection angle defines the optimum position for viewing the scene.

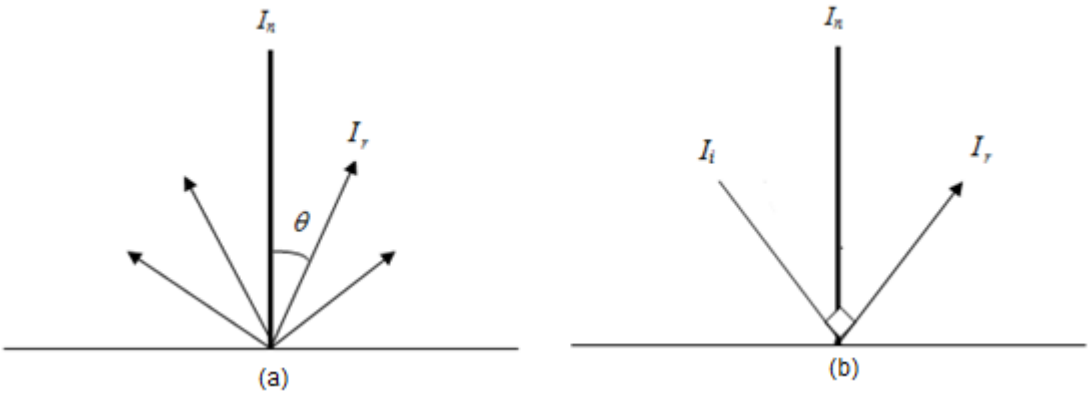

Figure 4-3 Shows (a) Lambertian surface and (b) specular surface.

4.1.2 Shadow

The amount of illumination received by an area can be reduced as the results of shadows (22). Shadows may be caused by adjacent targets, clouds or any obstacles that block the illumination from impinging on the targets surface as illustrated in Figure 4-4. Due to the lack of the direct irradiance by the light source, the surface in the shadow would appear darker in intensity and exhibits smaller 'apparent' reflectance in general. When the surface is in complete shadow it is illuminated by diffuse irradiance scattered by the surrounding objects in the scene or particles in the atmosphere. This scattered energy hitting the target surface before reflected to sensor field of view. Thus the energy that is captured by the imaging system is low with non-zero value.

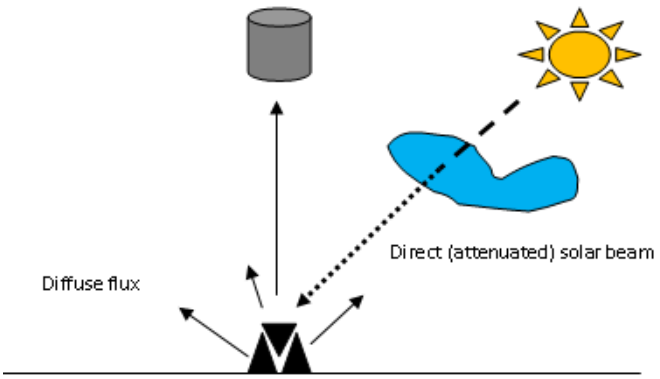

Figure 4-4 Sketch of cloud shadow geometry (34).

Shadow effects do not merely exhibit a lower energy of the reflected light; they also induce a change of the spectral shape when compared with the same object under direct irradiance. The extent of the change is dependent on the surroundings such as the atmosphere and the background of the scene. For scenes that contain homogenous and uniform background and that when the sky is misty white, the change of spectral shape due to diffuse irradiance is not an important issue, as shown in Figure 4-5.

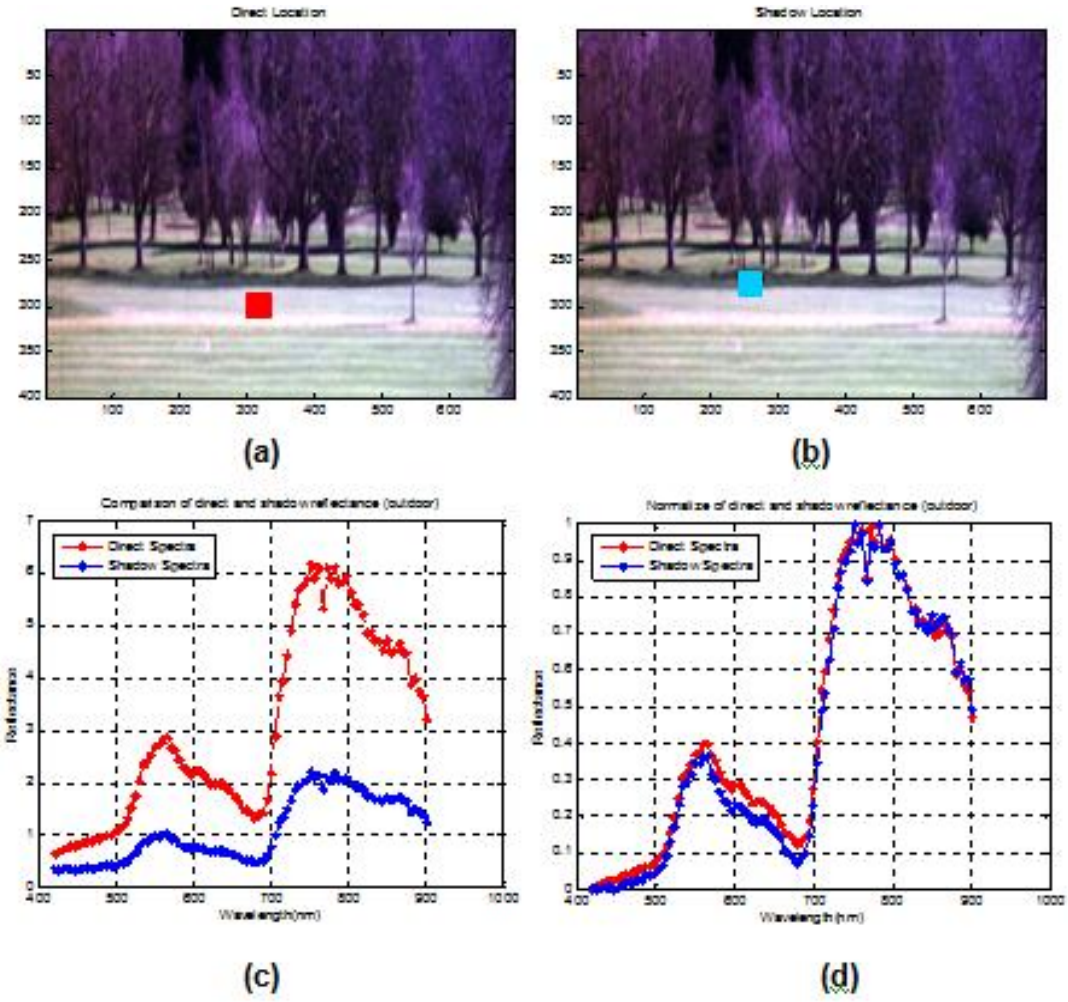

Figure 4-5 (a) red square and (b) blue square represent the location extracted from the image of fully illuminated pixels and shadow pixels respectively, (c) the spectral shape of direct and shadowed pixel are the same due to homogeneous background and that the sky is misty white, (d) normalised spectra of direct and diffused irradiated grass.

However, for the scene that contains many different types of surfaces crowded together in small area such as that in an indoor scene which consists of coloured wall (magnolia), desk or boxes, the spectral shape change due to diffuse irradiance appears to be very significant. This is illustrated in Figure 4-6 which depicts significant change of spectral shape of the shadowed surface illuminated by diffuse irradiance with respected to that under direct illumination.

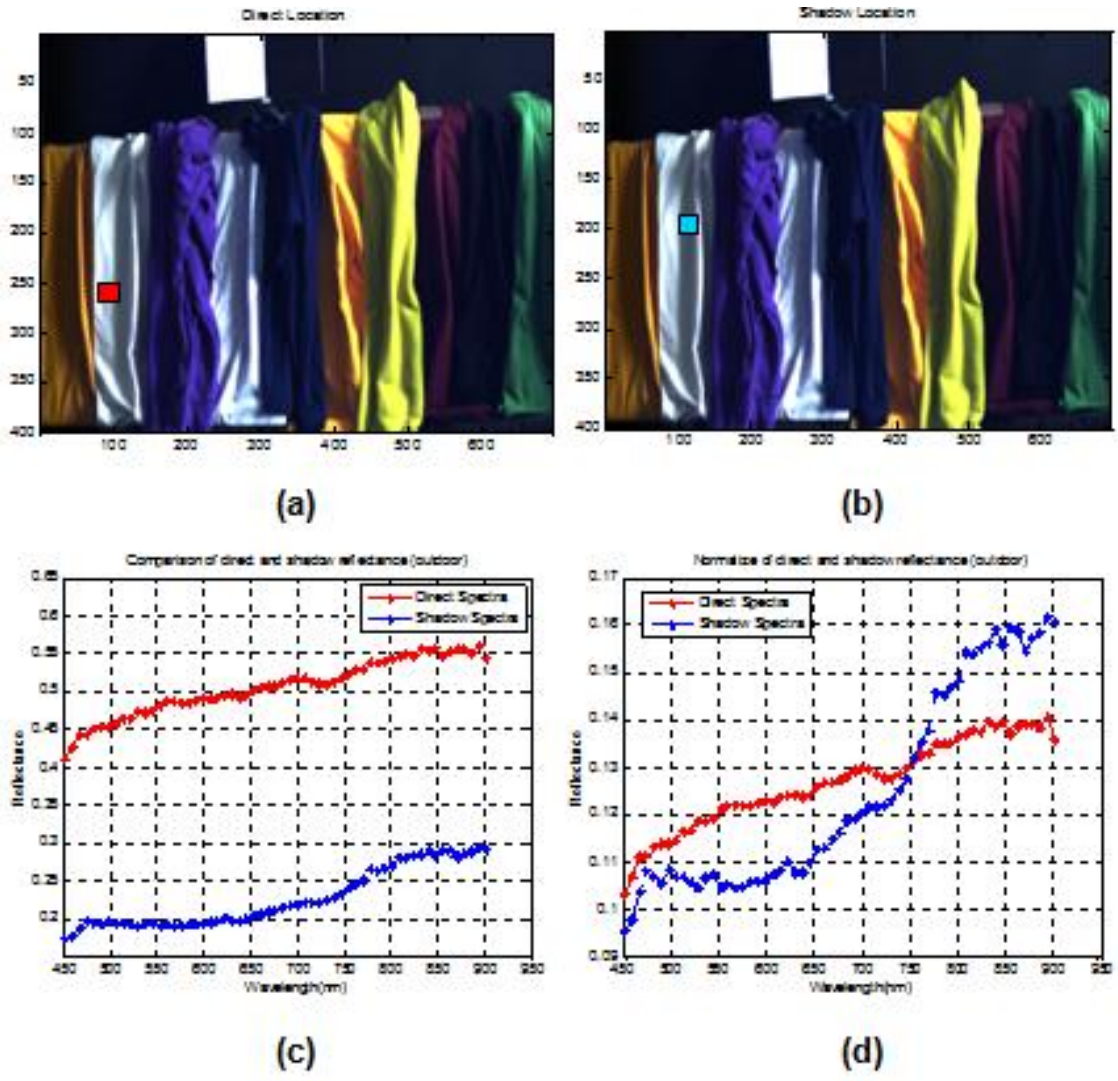

Figure 4-6 (a) red square and (b) blue square represent the location extracted from the image for fully illuminated pixel and shadow pixels respectively, (c) the spectra shaped of shadowed pixel changed due to the complicated background (d) normalised spectra showing completely different spectral shapes between the directed and diffusely irradiated surfaces.

4.2 Previous Work on Shadow Compensation

Previous work by Franklin et al. (53) and Ranson and Daughetry (54) have shown that shadow can influence classification accuracy significantly. Several methods have been developed for correcting the shadows in hyperspectral remote sensing. One de-shadowing method has been implemented in the ATCOR atmospheric correction by Rolf Ritcher and Andreas Muller (55). This technique detects shadows using several spectral bands that are sensitive to shadows and then matched filter detection is employed to segment the shadows from the scene. However, there are some restrictions on implementations of this method. It is restricted to outdoor environments with cloud cover of less than 25%; therefore it is more suitable for satellite or airborne hyperspectral imaging. Other works that employ the matched filter concept have also been reported (56) with slightly different rescaling methods for shadow compensation. For MF method, sufficient number of bands is required for better estimation of the covariance metric.

Another popular method in shadow removal applications is the band ratio approach (57, 58 and 59). Band ratioing is an enhancement process in which the DN values of one band is divided by that of any other band (58) or adjacent bands (59). Given B_1 and B_2 are two different spectral bands of hyperspectral data, band ratioing is deployed as,

$$Band\ \ Ratio = \frac{B_1(x,y)}{B_2(x,y)} \qquad \textbf{(4-7)}$$

where B_2 may be either an adjacent band of B_1 or any other band that is not similar to B_1. When B_1 and B_2 have similar radiance or reflectance values, the resulting band ratio will be close to 1. The disadvantage of this method is that two different targets may exhibit similar reflectance after ratioing even though they are completely different materials and therefore this method may not be always applicable.

Besides ratioing, normalization techniques have also been deployed among hyperspectral communities for shadow compensations (60). This has been a simple and rather efficient way to suppress topographic and atmospheric effects on the HSI satellite data. This method is often implemented by normalizing the radiance or apparent reflectance R_d by the spectral norm of the pixel:

$$R_d(\lambda) = \frac{r_d(\lambda)}{\frac{1}{N}\sum_{j=1}^{N} r_d(\lambda)} \quad \textbf{(4-8)}$$

where N is the number of bands. Alternatively the normalization can be performed through the magnitude of the spectral vector, such as the difference between the maximum and minimum values in each band. Normalization has also been examined under indoor lightning scenario hoping to achieve illumination invariance for HSI data (61). However, the method was found sensitive to outliers and could not achieve spectral constancy.

Another similar method using a threshold of the radiance has been reported for large percentage of shadows in the scene (62). This method is applicable for highly homogeneous background and that when >50% of the scene is under direct illumination. The reflectance of the pixels under full illumination is firstly calculated using an equation based on a simplified radiometric transfer function and this reference value is then used for the correction of shadow pixels. This methodology has achieved some sort of illumination-invariant motion detection and object tracking in real time.

The other popular method in shadow correction is linear and nonlinear unmixing for shadow correction introduced by Boardman (87, 88). This method chooses the endmember pixels to improve the target reflectance that is under shadow. For this method, the choice of endmembers should be selected properly for better shadow pixel characterization. More work in hyperspectral shadow compensation has been reported by Edward Ashton et al. (63). This method classifies the scene by using a Spectral Angle Mapper (SAM) which is insensitive to the illumination. Then a clustering method such as K-means is

used to identify the shadow pixels from the image. The correction is carried out on the shadow pixels by subtracting the mean from each class based on the equation,

$$x'_{i,j} = x_{i,j,c} * \left(\frac{(\overline{\mu}_{NSC} * \overline{w}_{i,j}) + (\overline{\mu}_{SC} * (1 - \overline{w}_{i,j}))}{\overline{\mu}_{sc}} \right) \quad \textbf{(4-9)}$$

where $x'_{i,j}$ = current pixel with classification c

$\overline{\mu}_{SC}$ = mean vector for all shadow pixels in class c

$\overline{\mu}_{NSC}$ = mean vector for all non-shadow pixels in class c

$\overline{w}_{i,j}$ = weight mask at pixel (i, j)

The only limitation for this method is that the user needs to have a prior knowledge of target class before correcting the shadow pixels based on the assign class.

The latest work has been reported by Friman et al. that combines passive and active imaging for illumination and shadow compensation on hyperspectral imageries (89). This work segments the illumination invariance map using the Digital Surface Model (DSM) generated from an airborne LIDAR (Light Detection and Ranging). Upon the establishment of the map, the shadow pixel is identified and corrected using the non-linear squares estimation. Similar work has been done by Nischan et al. that also combines passive and active imaging for illumination and shadow compensation on hyperspectral imageries (92). A laser illuminator such as white laser source is attached on the front of the hyperspectral camera. By placing an illuminator in front of the imaging system, this technique is able to eliminate illumination and viewing angle factors for retrieving target reflectance of pixels that are under the shadow. Although the method has shown good result in shadow compensation it requires hyperspectral images to be combined together with images captured by a LIDAR system.

5 HSI EQUIPMENT

5.1 HSI Camera

Two types of hyperspectral imaging systems have been used for image acquisition during the course of this PhD research: a Headwall spectrograph for Visible Near Infra-red (VNIR) wavebands and a Specim spectrograph for Short Wave Infra-red (SWIR) spectral range as shown in Figure 5-1. The Headwall VNIR camera has a spectral sensitivity between 400 and 1000 nm and it is capable to deliver excellent image quality through a high sensitive silicon charge couple device (CCD) detector. This type of photon detector converts absorbed photon energy from incident light to an electrical signal. The changes in the electrical signal determine the amount of the incident optical power. The SWIR camera utilises an infrared thermal detectors, Hg1-xCdxTe (Mercury Cadmium Telluride - MCT) combined with a high performance thermo electrical cooler (TEC) for data collection within the 900 to 2500 nm spectral range.

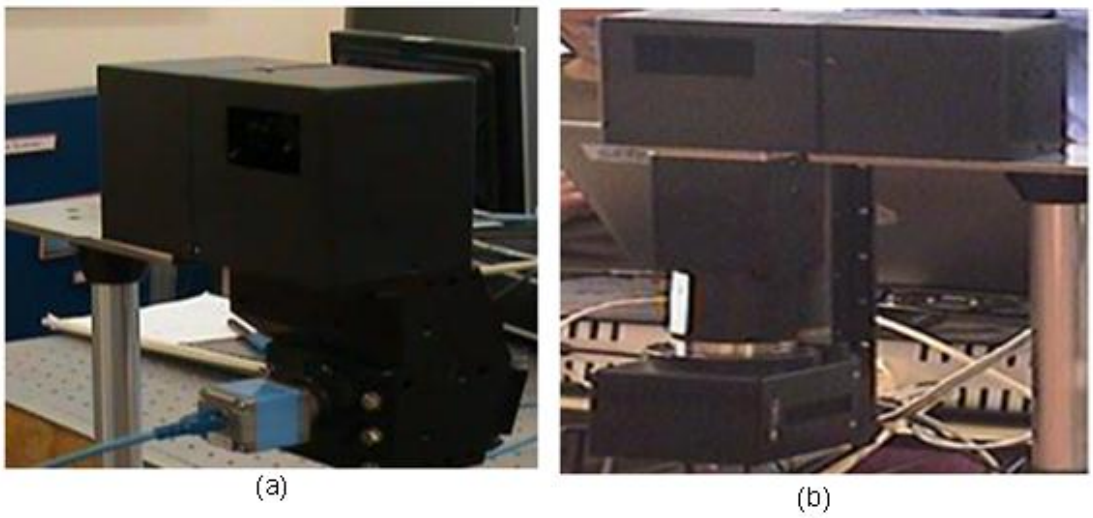

Figure 5-1 Picture of (a) The Headwall Visible Near Infra-red (VNIR) imaging system and (b) the Specim & Xenics Short Wave Infra-red (SWIR) imaging system.

In the heart of the hyperspectral imaging system is a spectrograph which provides the spatial and spectral information simultaneously. The spectrograph

disperses the incoming light into its constituent wavelengths. There are many ways to disperse the light. Grating technology is the most common spectrograph used in early generation hyperspectral cameras, such as that built by Kaiser Optical System Inc. (55) as depicted in Figure 5-2. This technology works by passing the incoming light through a single high-dispersive holographic grating element.

The second type of spectrograph technology uses a prism-grating-prism (PGP) configuration. This spectrograph consists of a transmission grating sandwiched between two prisms. It is deployed widely such as that employed by the ImSpector™ (57) spectrograph manufactured by the Spectral Imaging Ltd. of Finland (Figure 5-3).

The third type of spectrograph uses a convex grating designed in an Offner configuration (58, 59) as shown in Figure 5-4. An Offner configuration consists of two concentric spherical mirrors for projecting a telecentric image onto an image sensor such as a semiconductor focal plane array. With a secondary convex mirror and a diffraction grating relay it can form an efficient imaging spectrometer (60). The incoming light that passes through the input slit is reflected by a mirror then collected and focused onto the reflective grating by a collimating mirror. This technology is utilised by the Headwall VNIR spectrograph which is employed exclusively in this PhD research.

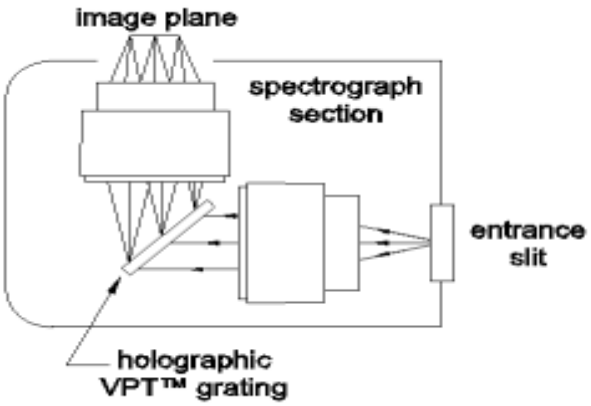

Figure 5-2 Holospec™ Spectrograph (77).

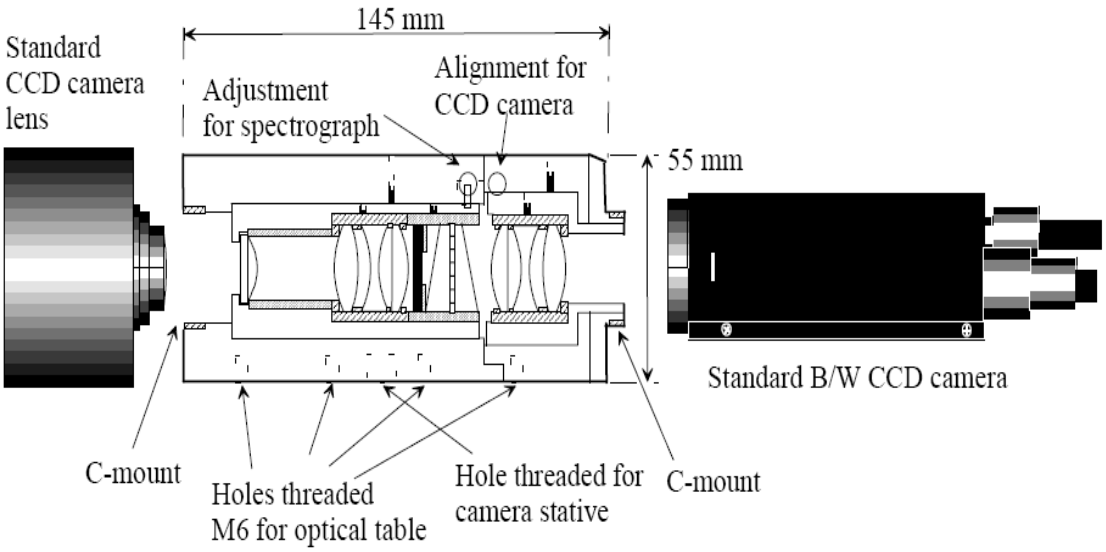

Figure 5-3 Diagram of the ImSpector™ camera (78).

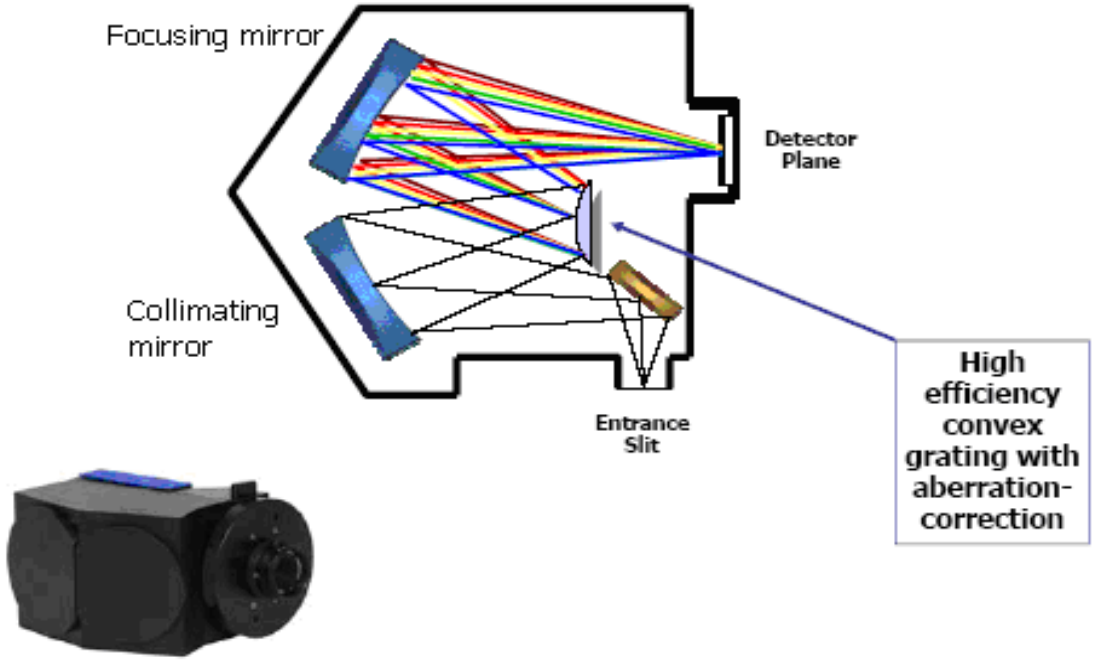

Figure 5-4 Diagram of an Offner Imaging Spectrometer and photo of the Headwall Photonics' spectrograph Hyperspec (78).

As a commercial hyperspectral imaging system is normally extremely expensive and our lab has chosen to develop our own hyperspectral imaging systems by assembling spectrographs, scanners, and related driver circuits (Figure 5-5) for a more economic and yet efficient HSI system. The optical scanner consists of

a rotating mirror which guides the light through the slit into the camera head. Two software systems, VNIR_2.0 and SWIR_2.0 (Figure 5-6) have been produced as controllers for the scanners of the Headwall VNIR and SWIR hyperspectral imaging systems for image acquisitions respectively.

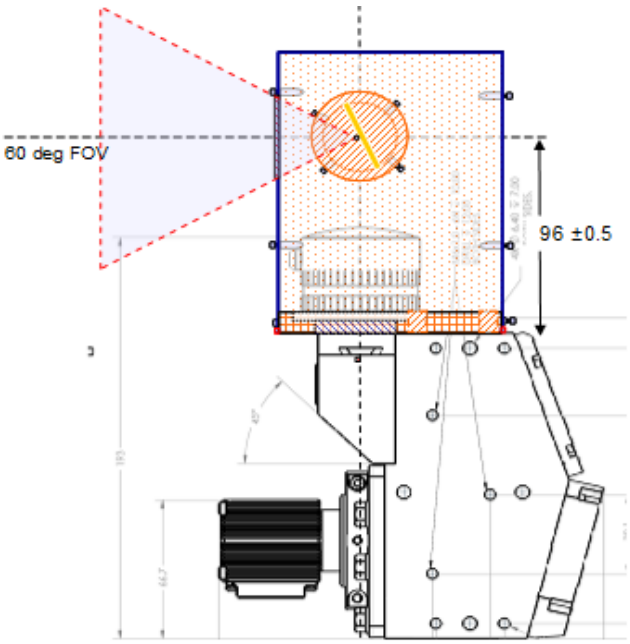

Figure 5-5 The rotating mirror system made by our lab (78).

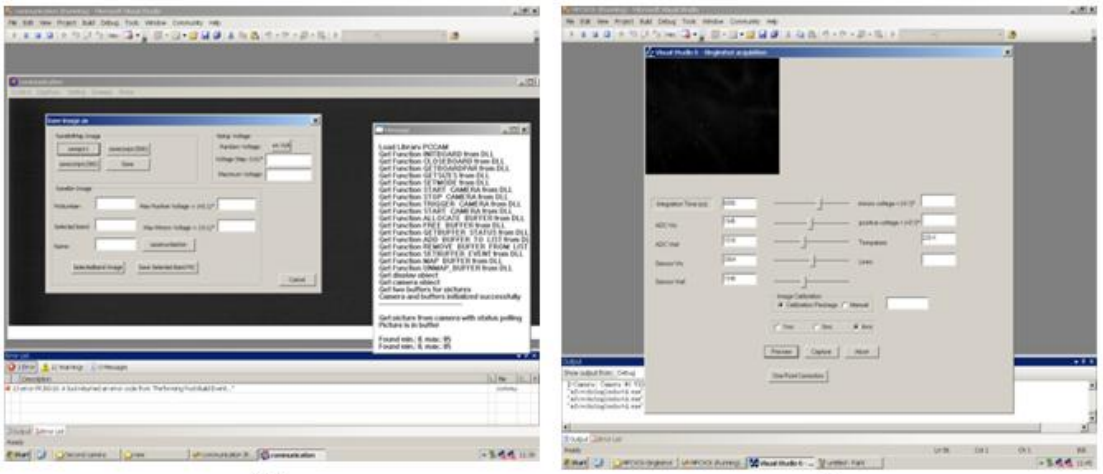

Figure 5-6 Pictures of the GUI for (a) VNIR_2.0 and (b) SWIR_2.0 program (78).

5.2 Radiometric Calibration

Radiometric calibration is frequently used to correct for sensor malfunctions or atmospheric effects. For sensor that works in visible to near infrared region, this system will record two kinds of radiant energies. One is the energy reflected from the target and the other is the energy reflected from the atmosphere due to scattering by the aerosols within the atmosphere.

For this research, all hyperspectral data that is recorded is corrected for sensor characteristics and atmospheric effects by using Empirical Line Method (ELM). In order to utilize this method, two calibrated panels, white and black spectralons, are placed in the scene during the experiment (Figure 5-7). The spectralon exhibits constant diffuse reflectance independent of the viewing angle. The mean spectra of both calibration panels (white and black panel) are used to generate the linear fit to solve for gain and offset in converting the digital number data to apparent reflectance data. For this research, all data that is converted to apparent reflectance data is denoted as RW data.

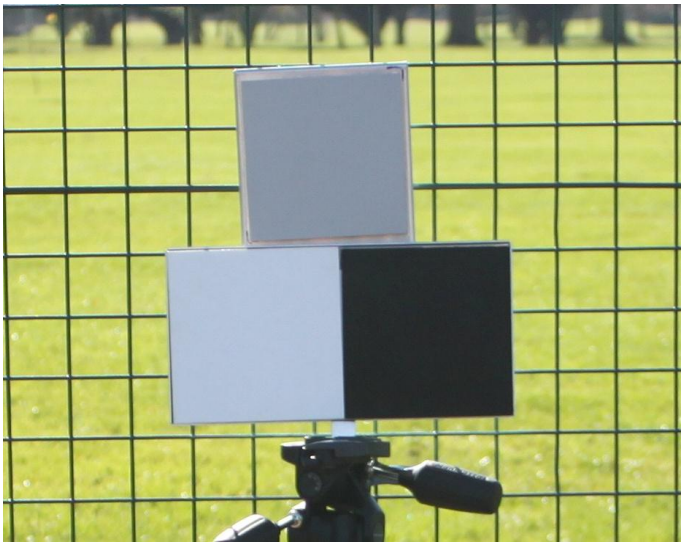

Figure 5-7 The calibrated panels used in this PhD research: top- gray panel (50% reflectance), bottom left- white panel (98% reflectance) bottom right- black panel (2% reflectance).

6 DIFFUSE IRRADIANCE COMPENSATION (DIC) METHOD FOR SHADOW COMPENSATION

Most work within the HSI community commonly assumed full illumination of the scene. The irradiance due to diffuse light (E_{diff}) and multiple scattering by the background have been ignored or treated as a very minor factor. This approach will lead to errors on the assessment of shadows which normally result in exhibiting lower 'apparent' reflectance values than that of the same target under directed illumination. Consequently, the same target can be mistakenly classified into two different classes heavily jeopardises the classification accuracy.

The diffuse irradiance in the outdoor case behaves quite differently from that of the indoor one due to the different scatters and scattering mechanisms. In the outdoor case it is the particles and air (O_2) molecules in the atmosphere dominates the scattering events particularly in the blue region (400 ~ 550 nm) which gives an effective bluer spectrum in the diffuse irradiance. In the indoor case, multiple scattering of the NIR wavelength by the surroundings in the room is more effective, inducing a higher proportion of NIR spectrum in the diffuse irradiance. Unlike in the outdoor case where the concentration of the particles in the atmosphere remains fairly constant, the diffuse irradiance of the indoor case is strongly dependent on the exact background surroundings as well as the distributions of the objects or targets in the scene. It is impossible to model the diffuse irradiance in the indoor case without prior information of the environment. The purpose of this work is to develop a method to compensate the shadow effect for the indoor hyperspectral scenario by modelling the diffuse irradiance of the indoor scene.

6.1 Experiment Setup

The experiment was recorded by using the Headwall VNIR hyperspectral imaging system within a laboratory environment of predominantly white and yellow background. Two sets of data with 88 bands that consists of different coloured t-shirts have been chosen to represent multiple targets. Figure 6-1

shows the first data set that has been taken under uniform illuminations and Figure 6-2 shows the data taken under oblique illuminations at a range of ~4m from the halogen illumination lamps. This data consists of 10 different coloured t-shirt and they are labelled from 1 to 10. Self shadows have been seen from the data and a method known as diffuse irradiance compensation (DIC) (see below) is applied for shadows removal in this section. This experimental set-up has also been repeated by using 5 coloured t-shirts as targets and they are labelled from 1 to 5 as shown in Figure 6-3. The reflectivity spectra for all the 10 and 5 different coloured t-shirts under direct and diffuse irradiance is given in Appendix A and B respectively.

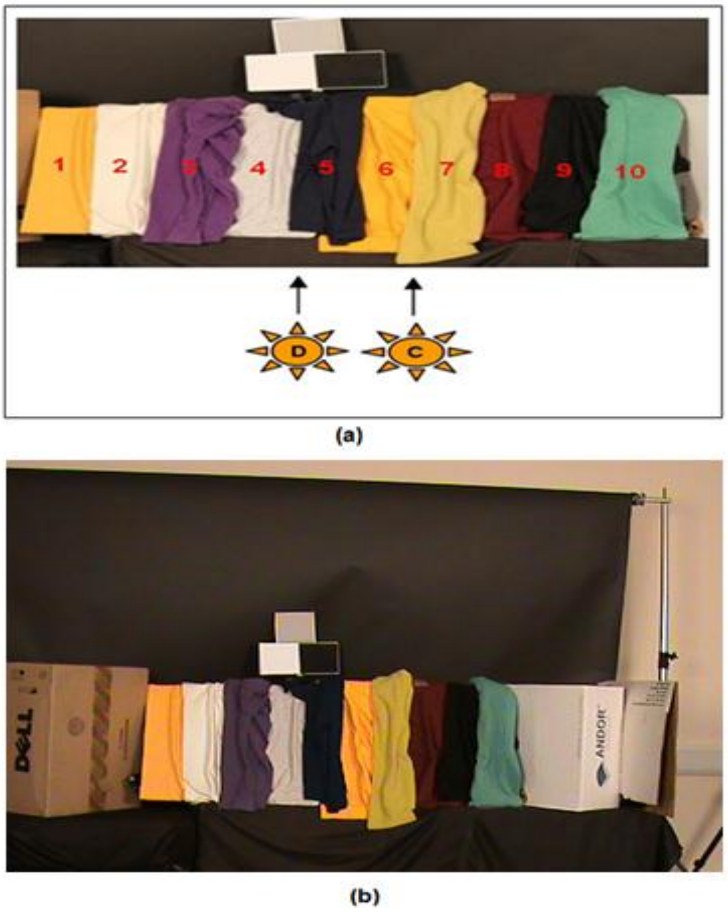

Figure 6-1 Shows (a) the data of 10 coloured t-shirts under uniform illuminations by light sources placed at the front of the scene denoted as C and D in the figure and (b) the RGB image of the experimental set-up showing the light blocker at both ends for shadows simulation.

(a)

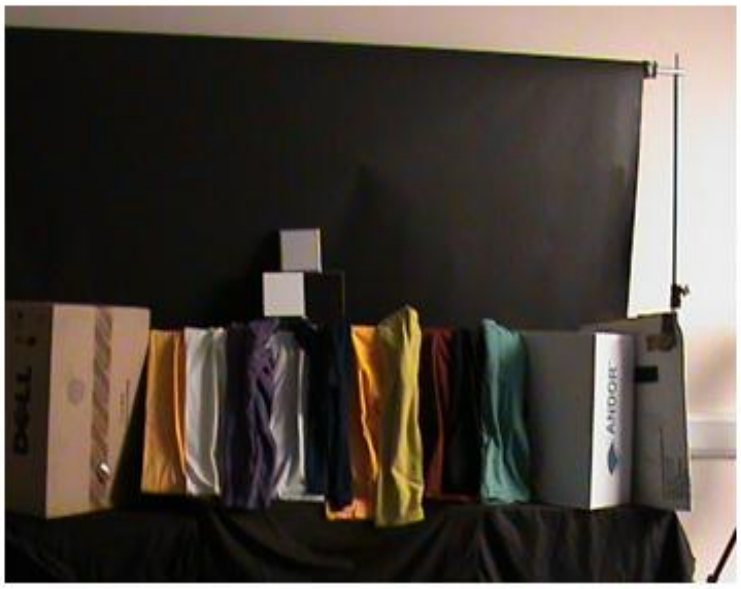

(b)

Figure 6-2 Shows (a) under oblique illumination casting self shadows in parts of the 10 coloured t-shirts (b) the RGB image of the complete scene under oblique illumination.

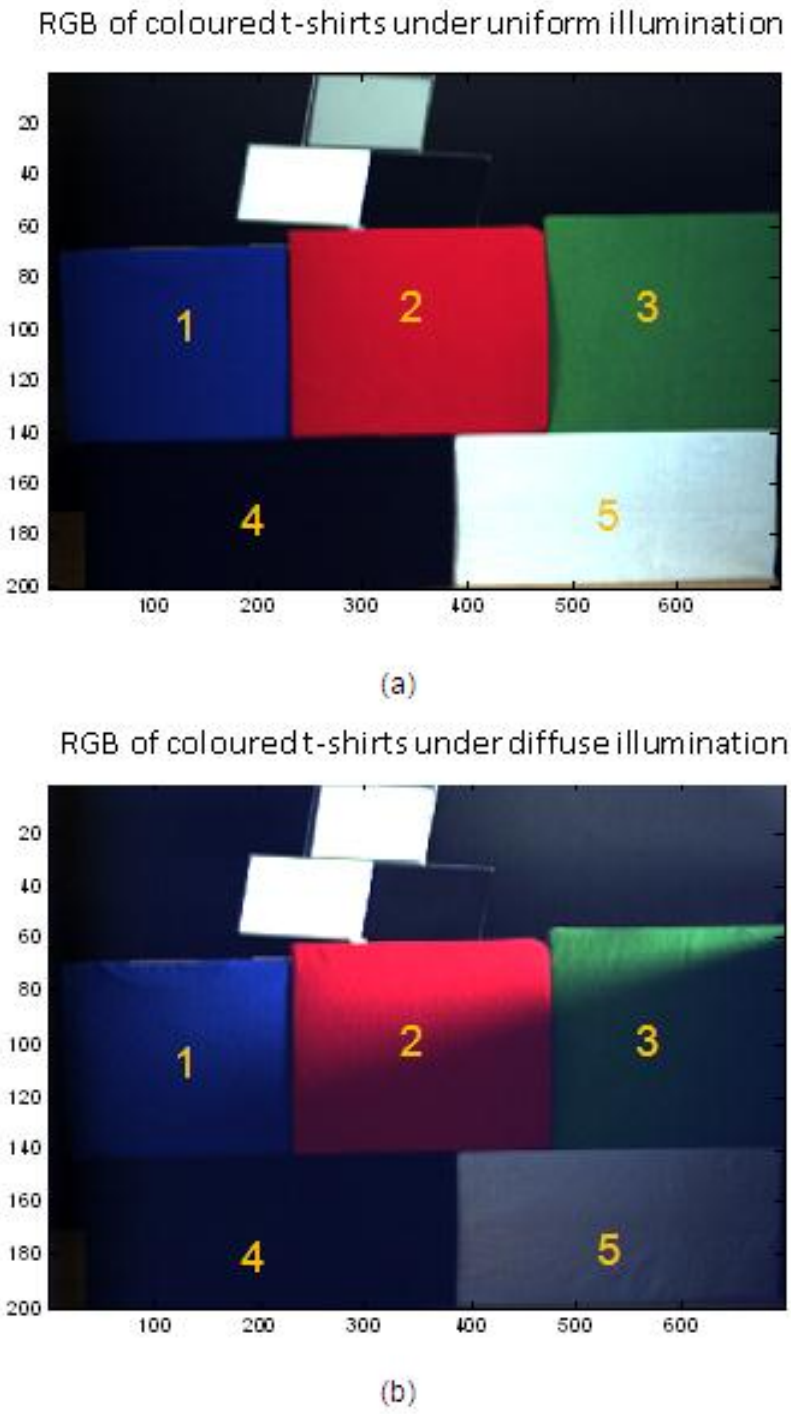

Figure 6-3 Shows (a) the RGB image of 5 coloured t-shirts under uniform illumination (labelled from 1 to 5) and (b) when it is under oblique illumination casting shadows on part of the targets.

6.2 Low Reflectance and Shadow Mask

The irradiance of a target under shadow is difficult to assess due to the various degree of the softness of the shadows throughout the scene. The only signal that is seen by the sensor from the target under complete shadow is the small reflected energy due to the diffuse irradiance from the adjacent targets, background or environment. The direct illumination is completely blocked by clouds or objects that cast the shadow.

Since shadow pixels have lower reflection intensity it is necessary to differentiate them from the low reflectance objects that may be present in the scene. In both cases the digital number (DN) of these pixels appears to be small; however, it is the shadow pixels and not the low reflectance objects that are needed to correct. In order to differentiate between low reflectance target and shadow pixels two different masks using spectral variance and spectral means, have been utilized for the classification of low reflectance objects and the shadowed pixels respectively. Figure 6-4 shows the flow chart to obtain the final mask.

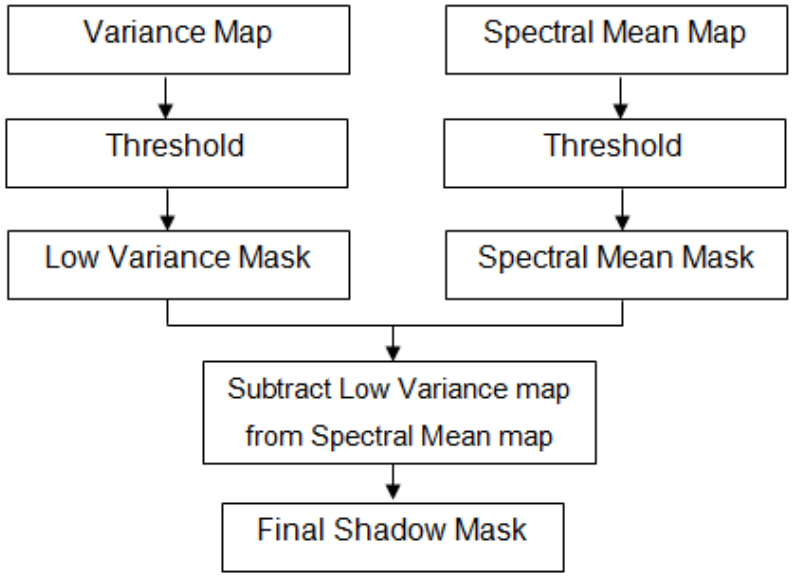

Figure 6-4 Shows the flow chart to obtain the final mask.

Figure 6-5 shows the spectral variance map of 10 coloured t-shirt data with the scale 0 to 0.7 to represent the value of variance. A low value of scale

represents the low variance of target pixels. The threshold is arbitrarily selected to define the low reflectance mask and for this data the value of 0.001 has been chosen as threshold value as shown in Figure 6-5 (b). The black coloured pixels represents low variance pixels.

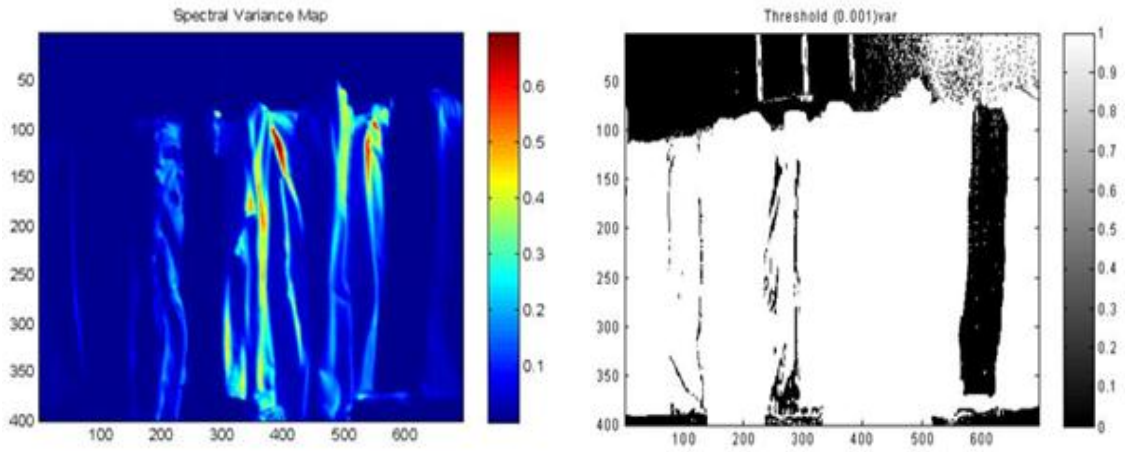

(a) (b)

Figure 6-5 The low variance mask calculated from the image under oblique illumination; (a) the false colour variance map and (b) the threshold of (a) used as the flat reflectance mask. This threshold map shows low variance target (indicated by scale equal to 0).

Then the spectral mean map is performed to get the shadow mask as in Figure 6.6 (b). In this map, the black pixels represent the low spectral mean pixels. Then, the final shadow mask is obtained by the subtraction of the low variance mask from the spectral mean mask as shown in Figure 6-6 (c). This procedure also has been repeated for 5 coloured t-shirt data as shown in Figure 6-7.

Masking of the flat reflectance (low variance) and shadow (low means) areas is important to avoid mis-correction of non-shadow pixels or overcorrection on shadow pixels. However, like any threshold process, a large threshold could potentially include non-shadow pixels or a too small of the threshold could miss some shadow pixels. In order to avoid this problem, the threshold is selected arbitrarily at about 0.001 and 0.2-0.26 in the variance and spectral means masks respectively. One drawback of this masking technique is that it may not

be able to identify the shadows pixels correctly for the shadows in the low variance materials (Figure 6.7(c)).

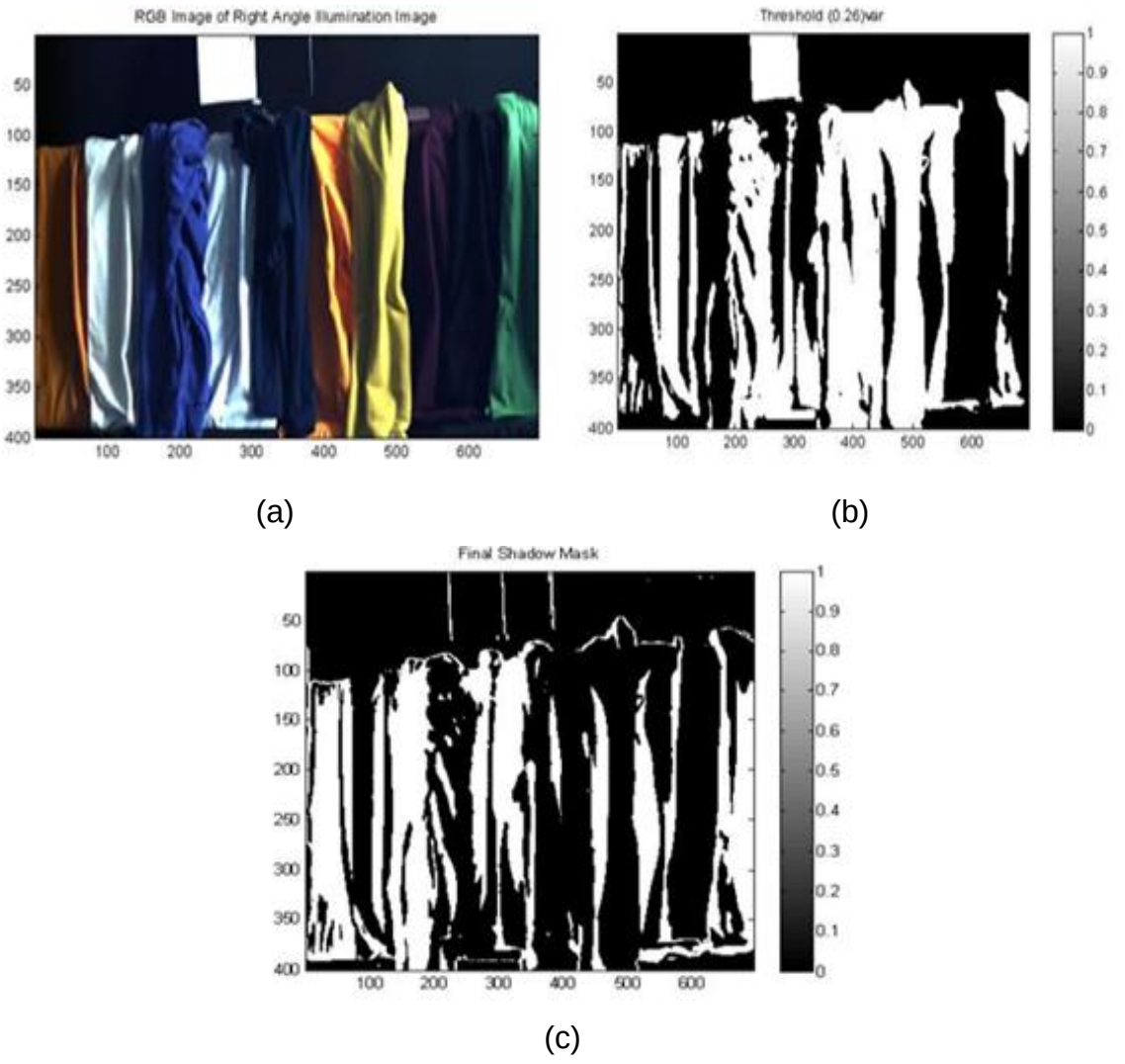

(a) (b)

(c)

Figure 6-6 The procedure for obtaining the final shadow mask: (a) the RGB image under oblique illumination, (b) threshold (0.26) of the spectral mean of the image which represents the low reflectance pixels in the scene (c) final shadow mask (bright areas) after the flat reflectance pixels are removed. White scale colour on the final shadow map (c) indicates the shadow pixels whereas black scale colour represents the direct illumination pixels.

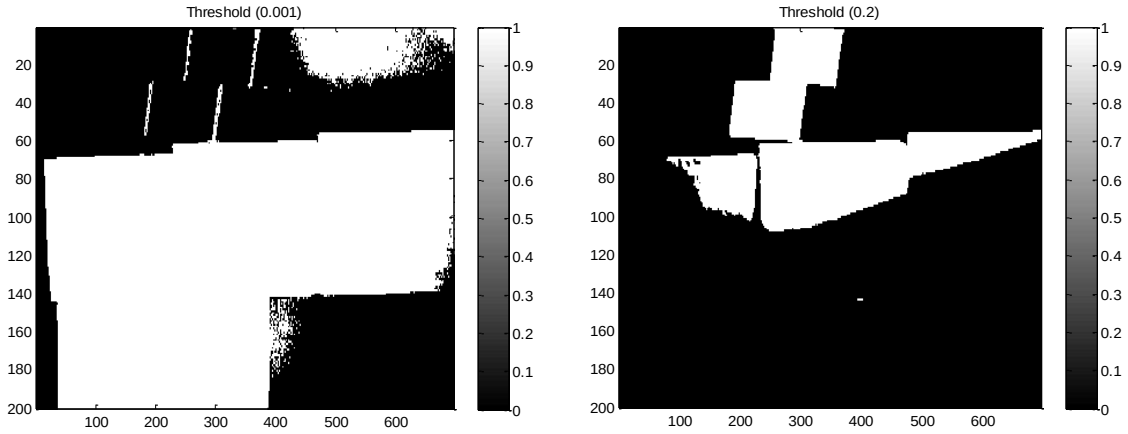

(a) (b)

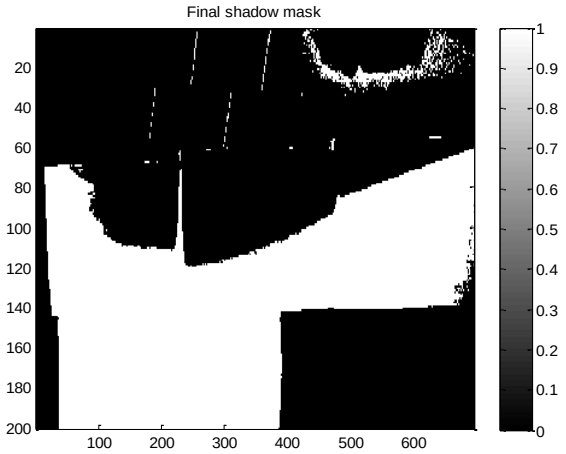

(c)

Figure 6-7 Shows the (a) flat reflectance mask (black areas) for the 5 coloured t-shirt experiment, (b) low reflectance pixels in the scene (black areas) and (c) final shadow mask (bright areas). Note that although

6.3 DIC Shadow Compensation Method

After the final shadow mask of the scene is established the DIC shadow compensation method can be applied for a better assessment of the intrinsic reflectivity from the hyperspectral data. In this method the spectral shape of the diffuse irradiance (E_{diff}) is estimated from a standard panel, in a way similar to that of assessing the direct irradiance (E_{dir}). To achieve this the E_{diff} is deduced from an experimental set up such that the standard panel receives both direct and diffuse illumination as shown in Figure 6-7 (circled in red). Figure 6-8 (b) illustrates the normalized spectral characteristics of direct (E_{dir}) and diffuse

irradiance (E_{diff}) estimated from this scene; the difference of the spectral characteristics between these two is quite apparent. The shadow compensation is carried out in the following procedure:

(a) The digital numbered (DN) values of the pixels inside the shadow mask are ratioed with the E_{diff}.

(b) For pixels outside of the shadow mask, which are directly illuminated, their DN values are ratioed with E_{dir}.

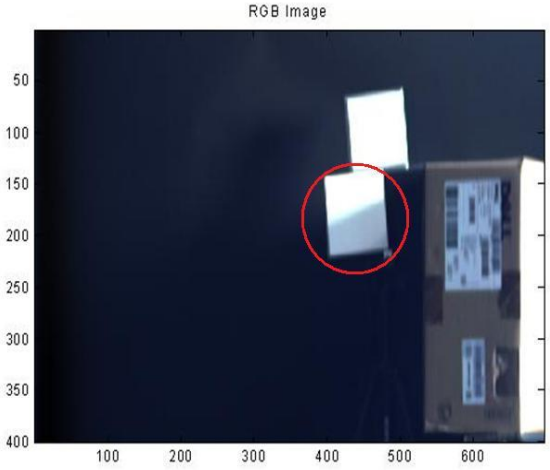

Figure 6-8 Shows the RGB image of the experimental set up for assessing E_{dir} and E_{diff}.

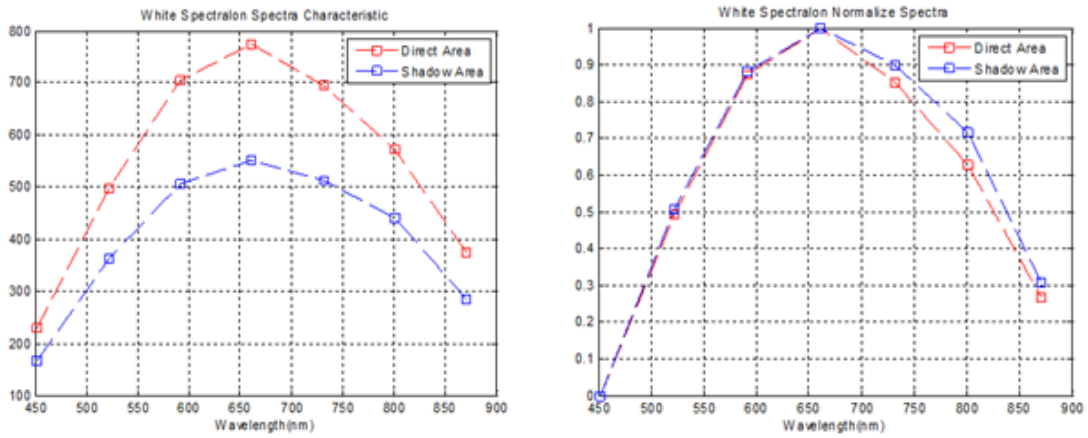

(a) (b)

Figure 6-9 Shows (a) spectral characteristics of E_{dir} and E_{diff} in DN values and (b) to highlight the difference in the spectral characteristics of the E_{dir} and E_{diff}.

6.4 Assessments Methods

The effectiveness of these shadow compensation algorithms is assessed using Quadratic Likelihood (QD) classifier. All the training data is selected from the direct illuminated pixels as shown in Figure 6-10. The training data size 100x40 pixels has been selected from each different coloured t-shirt. Based on this training data the target map is produced, as shown in Figure 6-11. The classification accuracy is evaluated using the following equation,

$$Accuracy(\%) = (PP - PN - NP)\frac{100}{N} \quad \textbf{(6-1)}$$

where PP, PN, NP and N are positive-positive, positive-negative, negative-positive and the total number pixels in the class respectively. The classification accuracy of the DIC method is compared with the same data but processed using other shadow compensation methods:

(a) Raw data without conversion into reflectance (denoted as Raw Image)

(b) The 'apparent' reflectance: the conversion of raw data into 'apparent' reflectance image using ELM method and the image is denoted as RW Image. All pixels are assumed to have received direct irradiance.

(c) Normalization: The albedo of the scene is calculated from the RW and every pixel is then normalized by its spectral norm (denoted as Norm RW and Norm DIC).

(d) Band Ratio: Every pixel in the RW is ratioed with respect to (i) its 870nm band (denoted as RW R870) and (ii) adjacent bands (denoted as RW RAdj).

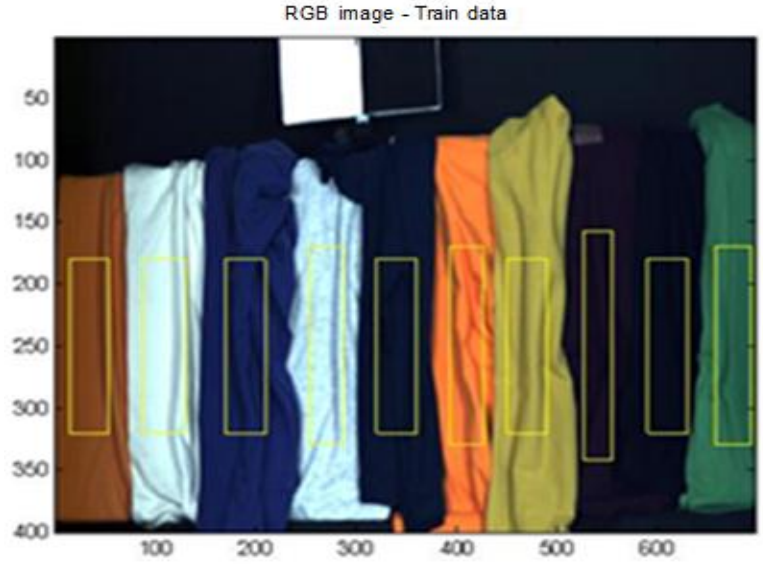

(a)

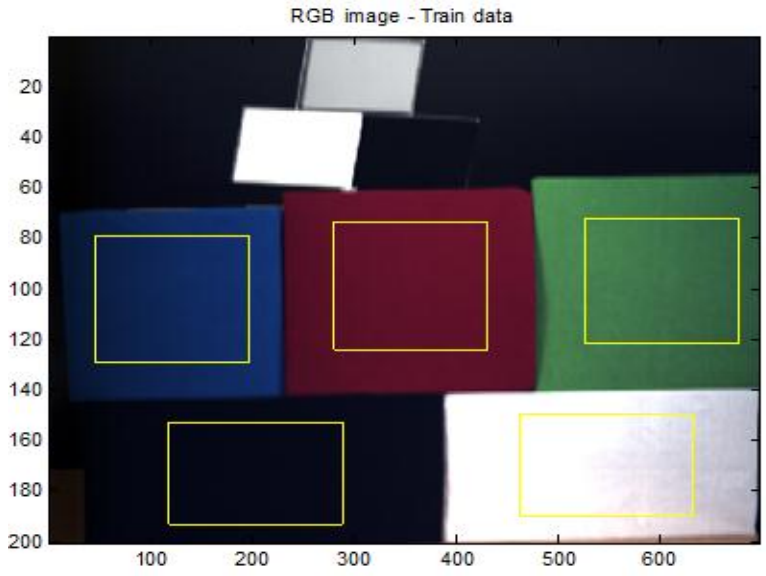

(b)

Figure 6-10 Shows (a) the RGB image of 10 different t-shirts data under direct illumination and (b) the RGB image of 5 different t-shirt data and the yellow box depicts where the training data pixels are extracted for classification.

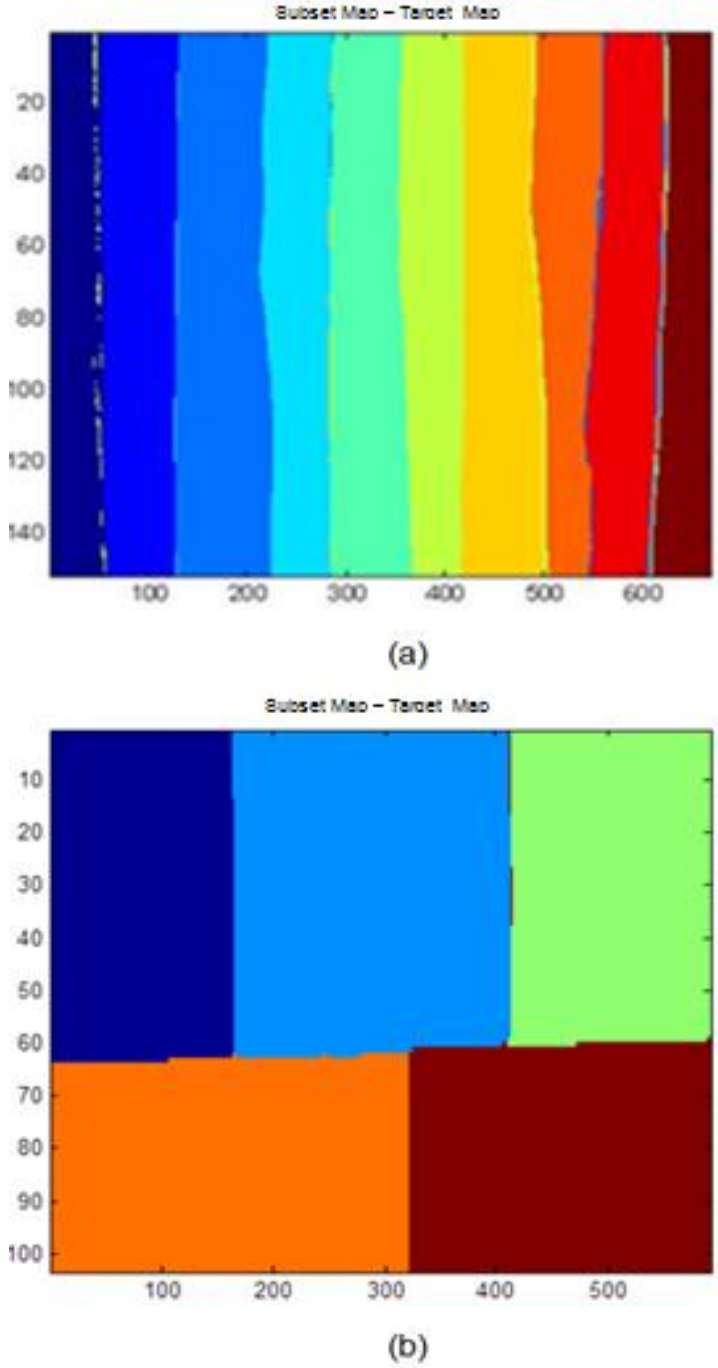

Figure 6-11 Shows the target map in false colours for (a) 10 different colours t-shirts and (b) 5 different colours t-shirts. These target maps are used to evaluate the accuracy of classification.

6.5 DIC Shadow Compensation Results

6.5.1 10 different coloured t-shirt data

Previous work has reported that affine transformations of data, such as that using ELM method, will not affect the separability and classification efficiency when using Quadratic classifier methods (62, 63). However, other studies (27, 64) have shown an improvement in inter-class separabilities when reflectance data is used. Figure 6-12 shows the classification results for the raw (DN) data together with the same image but transformed into 'apparent reflectance' via ELM based method (RW). DN data achieved 38% classification accuracy whereas the RW data attained 68% accuracy. Note the substantial misclassifications in the DN data particularly in classes 1 and 2. By transforming the raw data into apparent reflectance data, it helps to remove the sensor characteristics and to compensate some of the illumination artefacts, resulting in a better classification due to the enhancement of inter-class separation.

The classification result of DIC method is shown in Figure 6-13. It is seen that the DIC method has achieved the best overall classification accuracy of 70% compared to that of the RW image (68%). It is also perceived that most shadows, particularly those in the deep shade, can be compensated by the DIC method. However, it falls short for the lightly shadowed regions such as that in class 1. This is mainly caused by the deficiency of the present method which corrects all shadows by using the same E_{diff}.

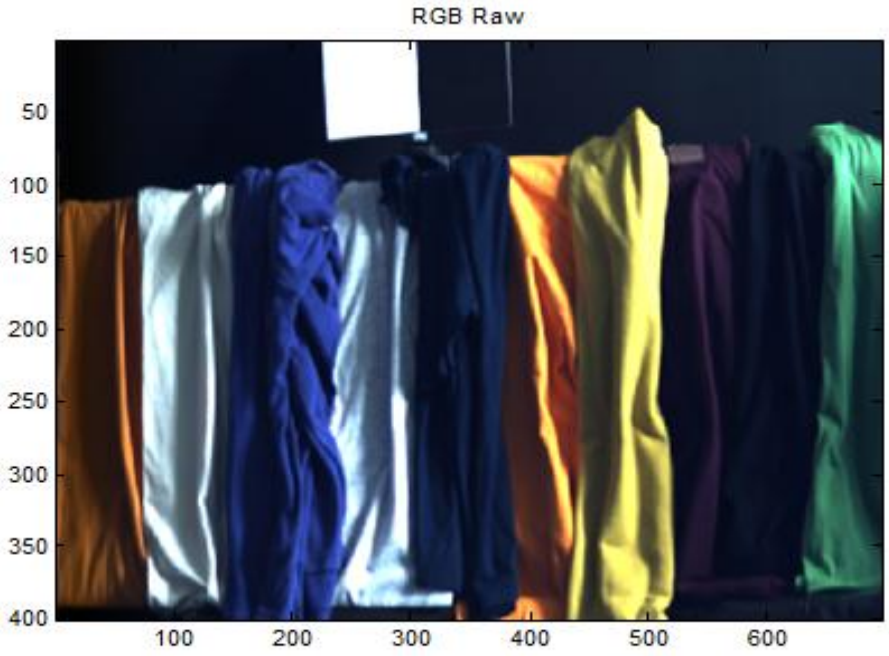
RGB Raw
50
100
150
200
250
300
350
400
100
200
300
400
500
600

(a)

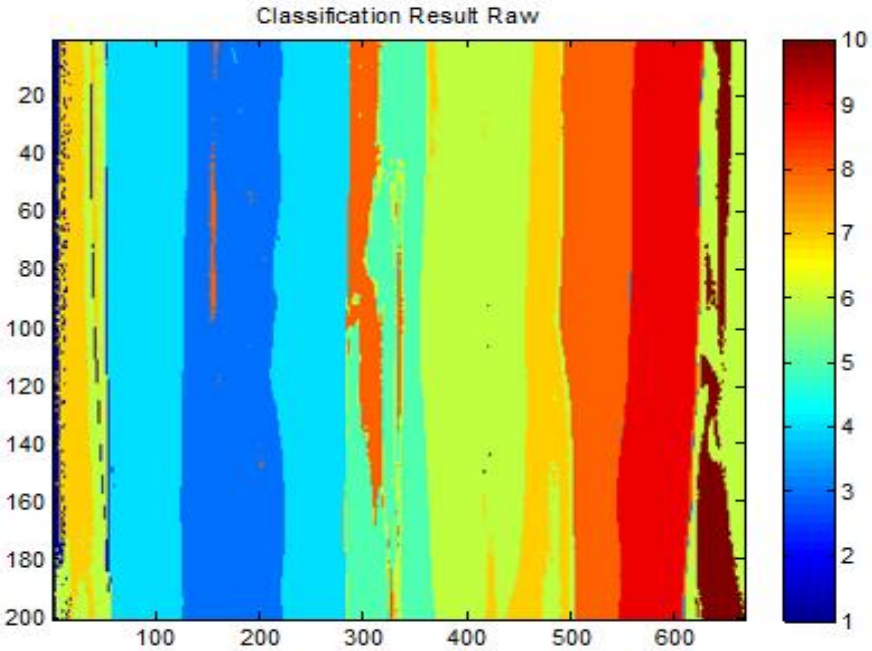
Classification Result Raw
20
40
60
80
100
120
140
160
180
200
100
200
300
400
500
600
10
9
8
7
6
5
4
3
2
1

(b)

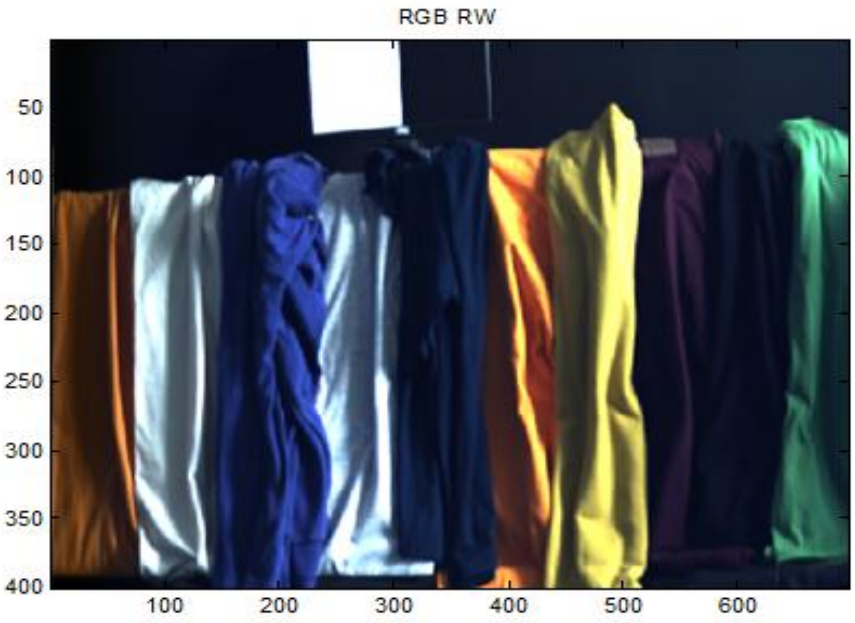

(c)

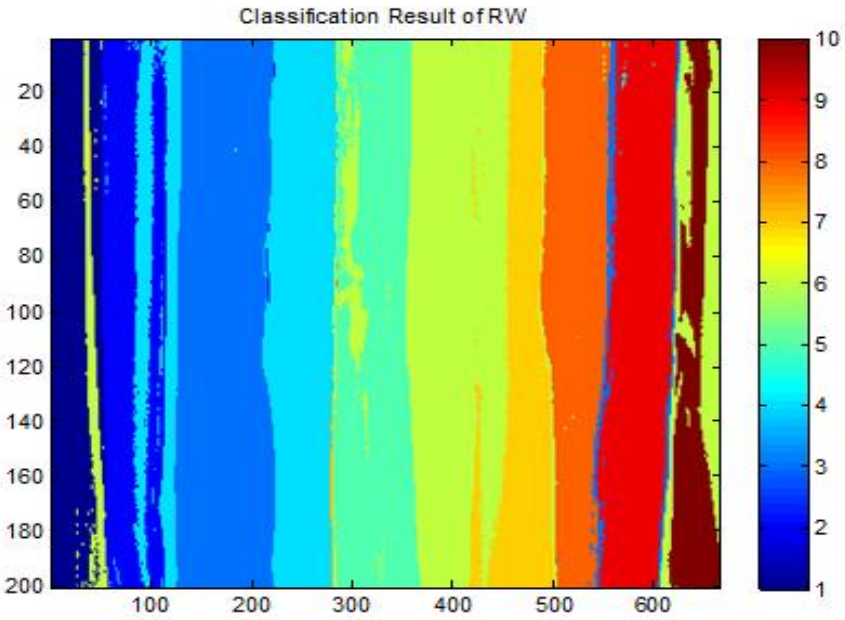

(d)

Figure 6-12 Shows RGB images of (a) Raw data, (c) RW data, (b) and (d) are the false colour image of the classification results for the respective Raw and RW data. The overall accuracies in these cases are respectively 38% & 68%, and note the large misclassifications in the classes 1 and 2 in the Raw data as shown in (b).

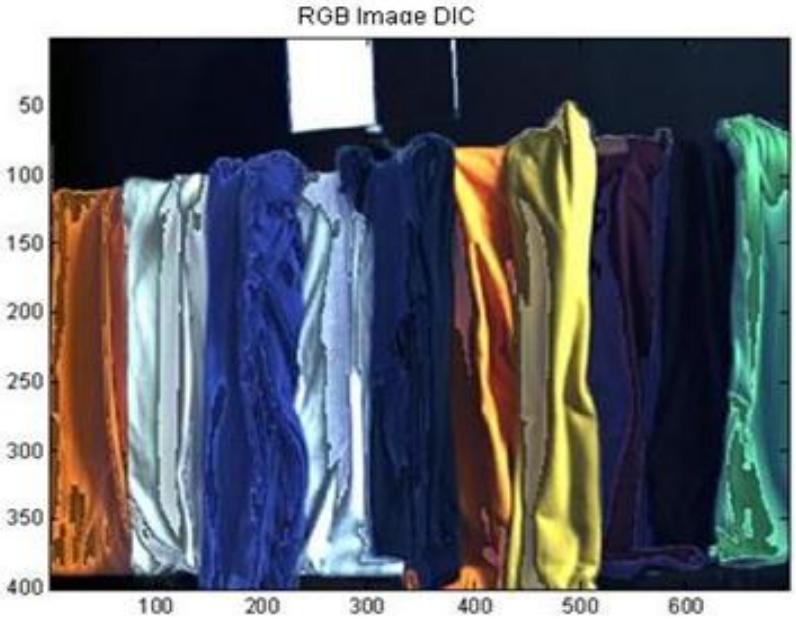

(a)

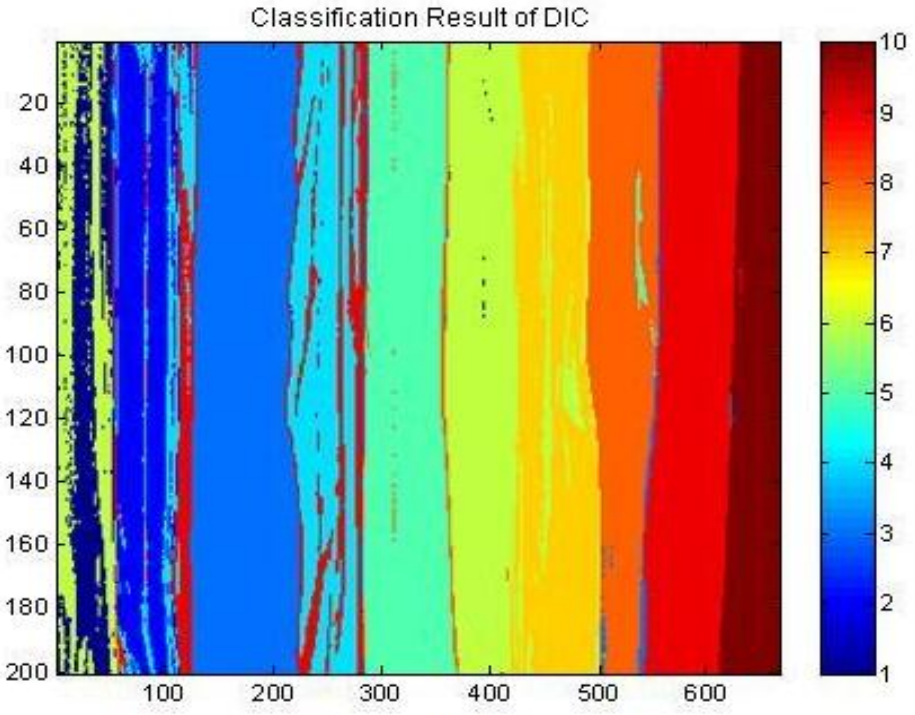

(b)

Figure 6-13 Shows (a) RGB image and (b) the classification result after DIC shadow compensation exhibit 70% of classification accuracy. Note that the DIC has achieved the best overall accuracy in comparison to that of the Raw and RW results.

6.5.2 Previous work on shadow compensation: Normalization and band ratio

Pixel vector normalisation has been a popular method for ‘flattening’ the illumination artefact within the HSI community (37, 59, 60 and 67). It is shown here that normalisation is not sufficient for this purpose and in many cases, such as indoor situations, the diffused irradiance is strongly affected by the background in the scene. Figure 6-14 shows the (a) RGB image of the targets taken under oblique illumination after normalisation (RW Norm) and (b) its classification result. This method results in large classification errors particularly in the shadow regions after the data is normalized. The classification accuracy is reduced from 68% (by RW) to 50% after the image is normalised, demonstrating the inefficiency of pixel vector normalisation for shadow mitigation in HSI processing. The DIC result is also compared with RW ratioed with band 870 (RW R870) and ratioed with adjacent band (RW RAdj). The band ratioing methods (RW R870 and RW RAdj) achieve only 62% of classification accuracy as shown in Figure 6-15 and Figure 6-16. This has shown that DIC method has achieved the best classification accuracy in comparison to the normalization and the two band ratioing methods which have been commonly adopted by the HSI community for shadow compensation.

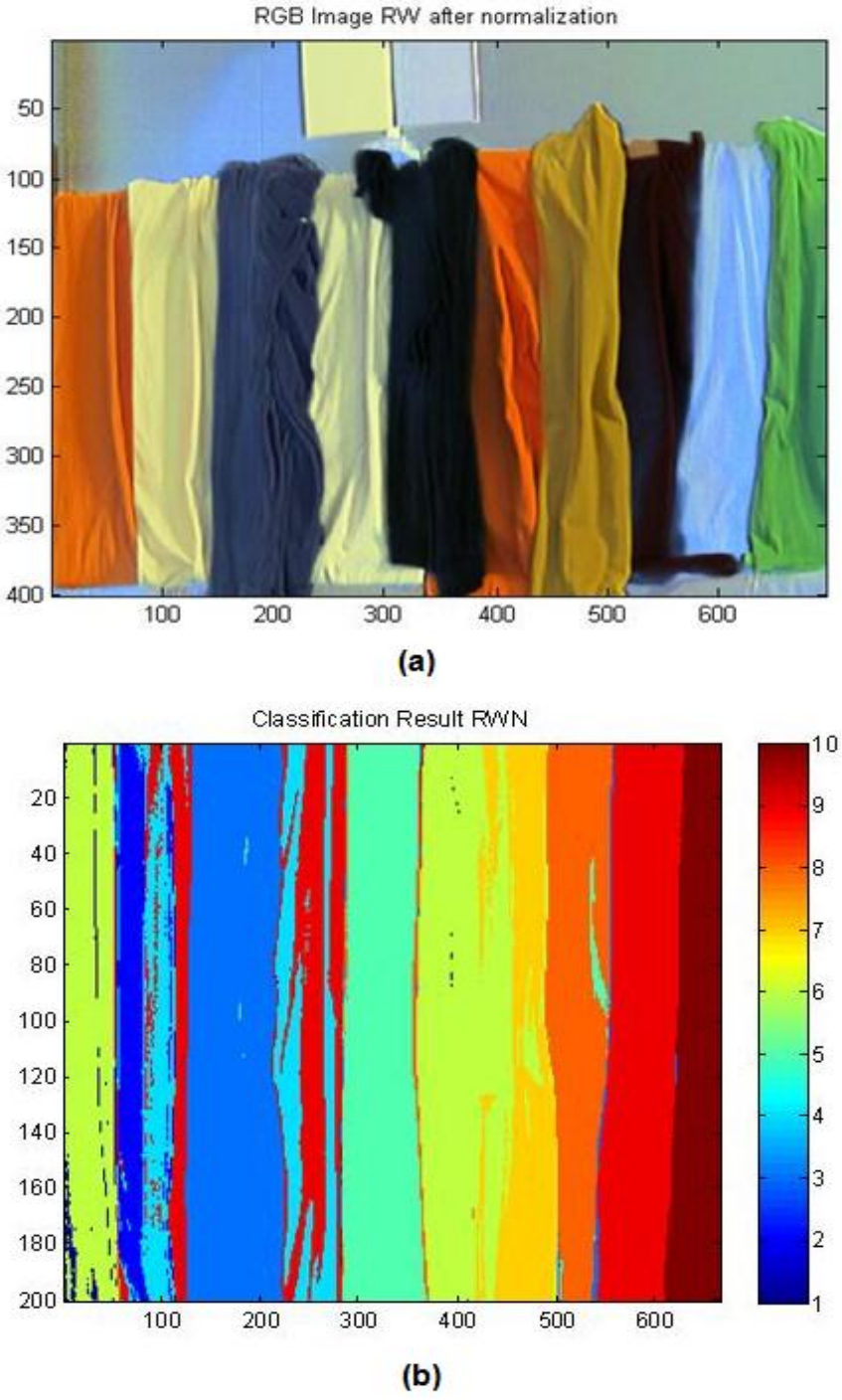

Figure 6-14 Shows the RGB images of the image taken at oblique illumination (a) after normalisation (RW Norm), and (b) the false colour classification results of RW Norm. Note that target classes 1, 2 and 4 have been substantially misclassified in the RW Norm data.

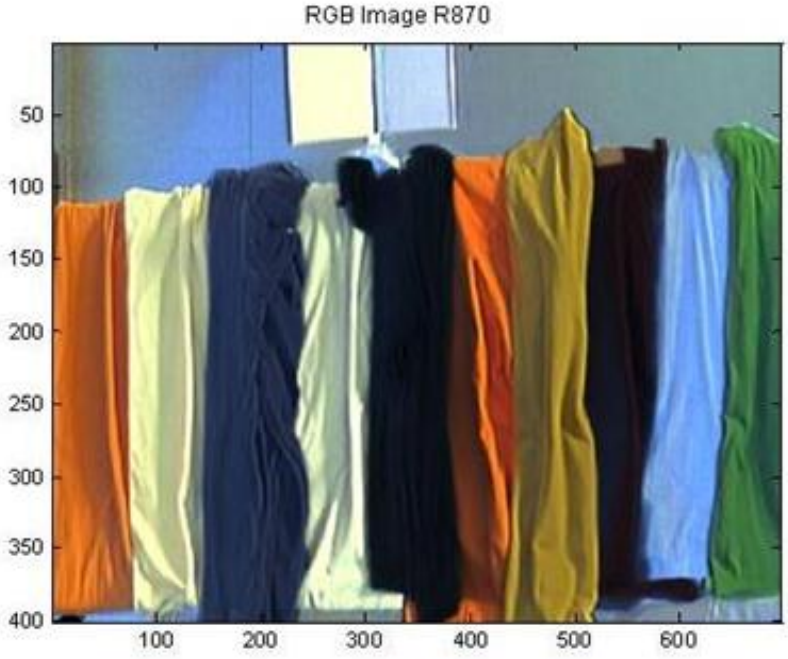

(a)

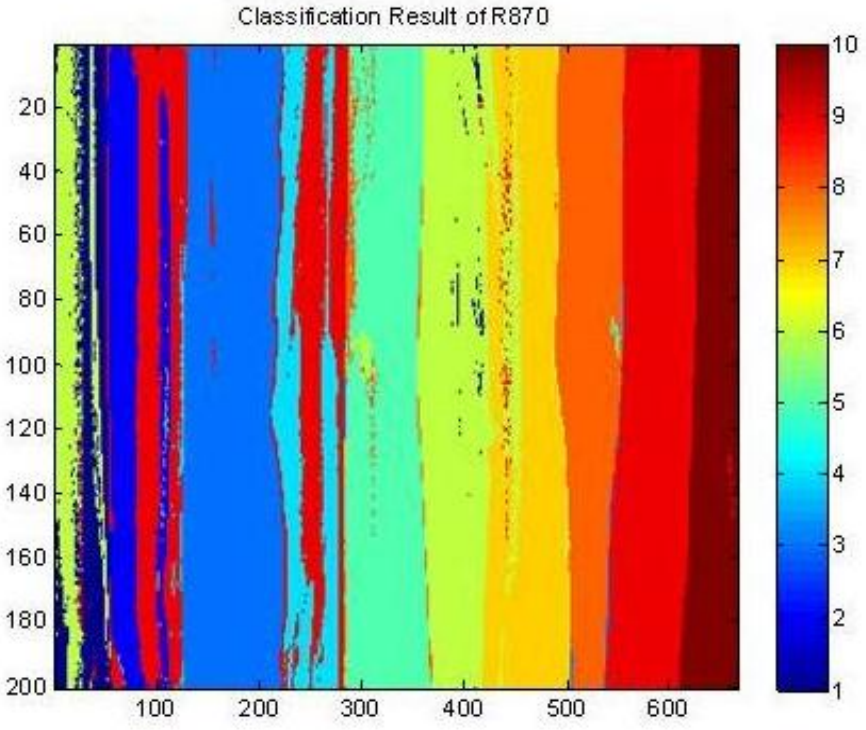

(b)

Figure 6-15 Shows (a) the RGB image and (b) the false colour classification result of RW R870 giving 62% accuracy.

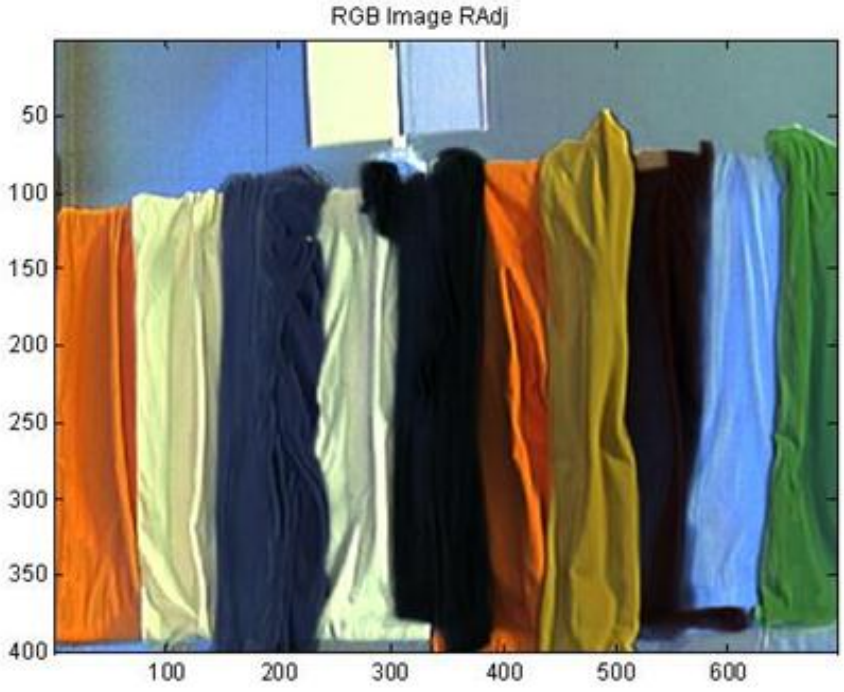

(a)

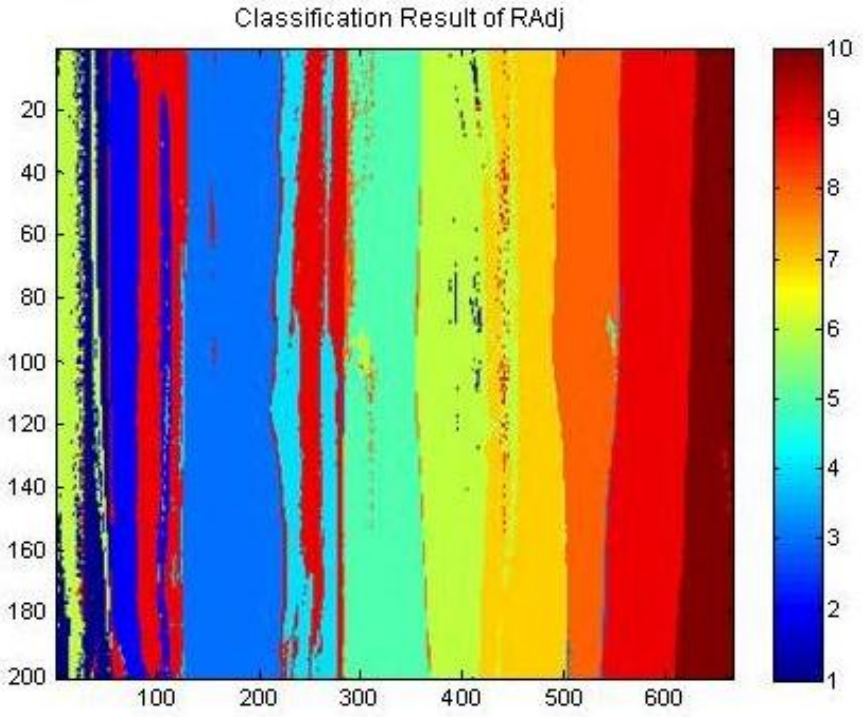

(b)

Figure 6-16 Shows (a) RGB image and (b) the false colour classification result of RW RAdj giving 62% accuracy.

6.5.3 DIC Method for 5 t-shirts data

In this section the DIC method has been applied on the 5 different coloured t-shirt data to check for reproducibility. As depicted in Figure 6-17, it is seen that the raw data can only achieve 31% of classification accuracy whereas the RW has attained 43% of accuracy. Similar to the previous result, the affine transformed data set after RW exhibit ~30% better than that using the raw data for the classification. This may suggest that by removing the sensor and atmospheric transfer functions one can achieve much better target recognitions from HSI imagery.

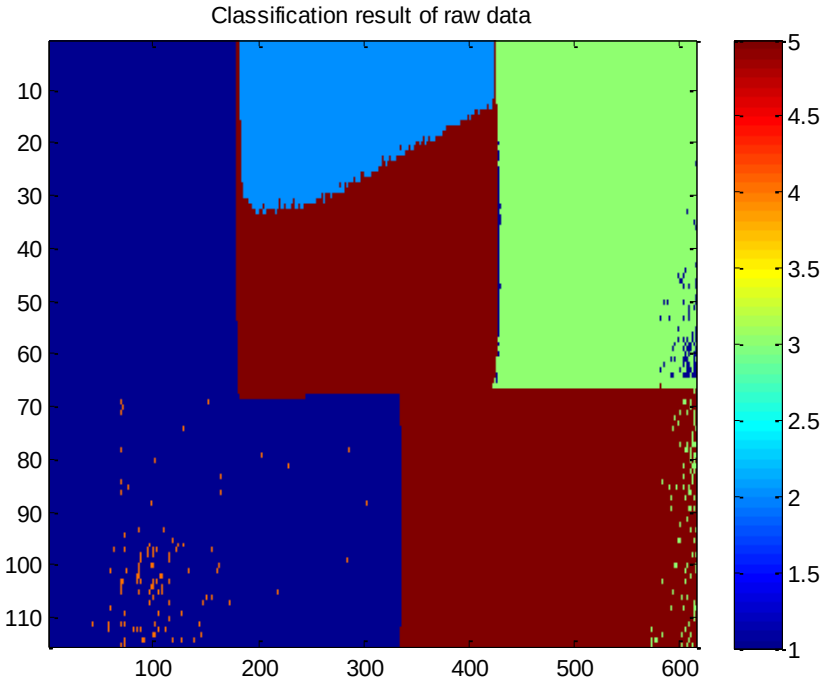

(a)

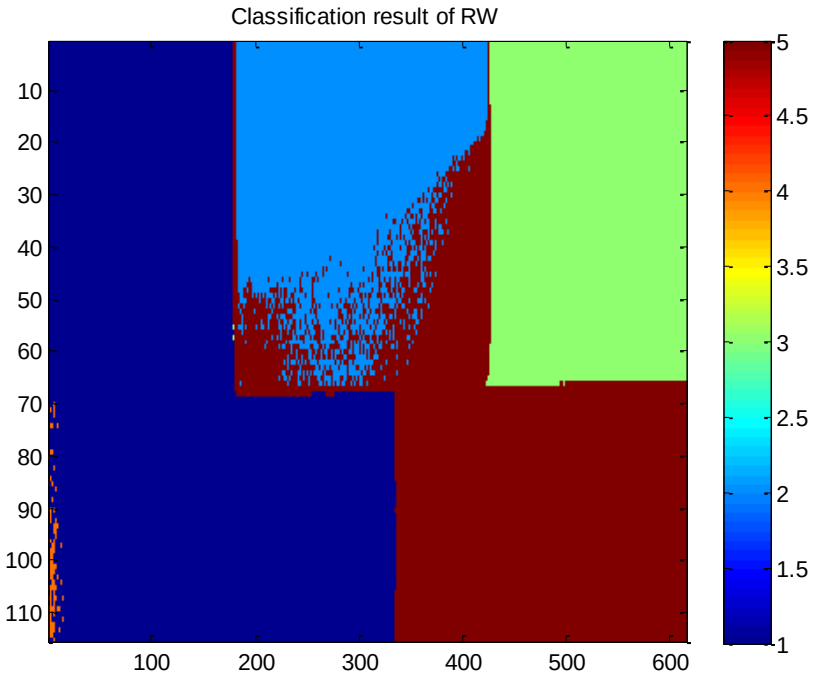

(b)

Figure 6-17 Shows the classification result of (a) the raw data and (b) RW data of 5 different coloured t-shit.

The results for the normalization and band ratio techniques also exhibit large errors with only 35% classification accuracy as shown in Figure 6-18 and Figure 6-19, respectively. These results thus suggest that previous illumination flattening methods such as the normalization and band ratio techniques in fact do not perform very well for shadow eliminations in HSI imagery.

On the other hand, the DIC method has produced the best result with 58% classification accuracy for this 5 coloured t-shirt data as shown in Figure 6-20. This result thus shows that the DIC method is capable to compensate the shadow artefact in hyperspectral processing much better than other techniques reported in the literature. Figure 6-21 shows the plot of the apparent reflectance for 3 selected shadowed targets before correction (RW), after correction via DIC method and to compare with that under direct illumination. From these plots it can be seen that the DIC method can help to restore ~80% of shadows

producing much better apparent reflectance characteristics of targets and to enhance classification accuracy rather significantly

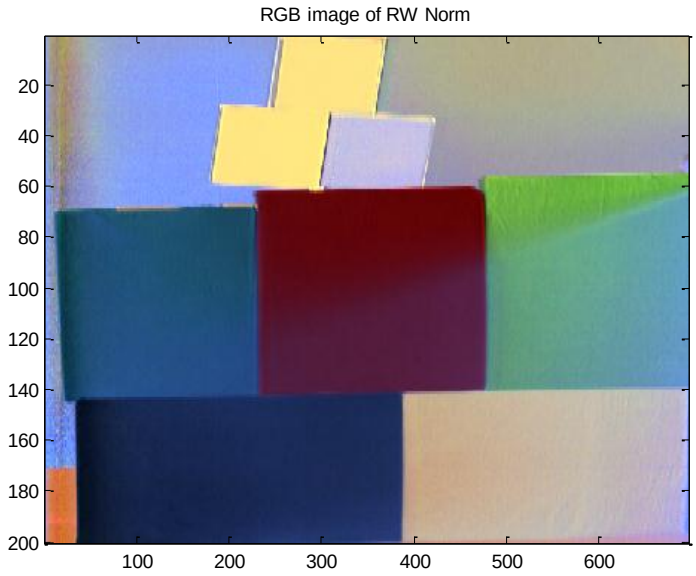

(a)

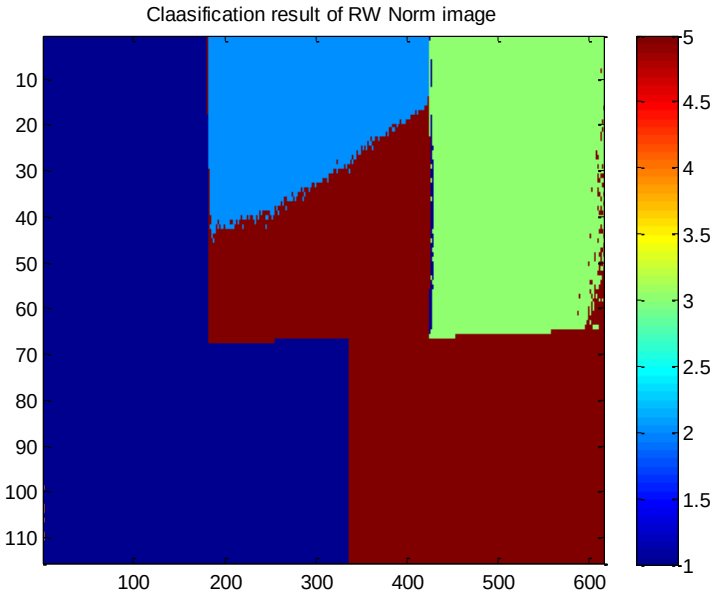

(b)

Figure 6-18 Shows (a) the RGB image of RW Norm for the 5 different coloured t-shirts and (b) its classification result exhibiting 35% accuracy.

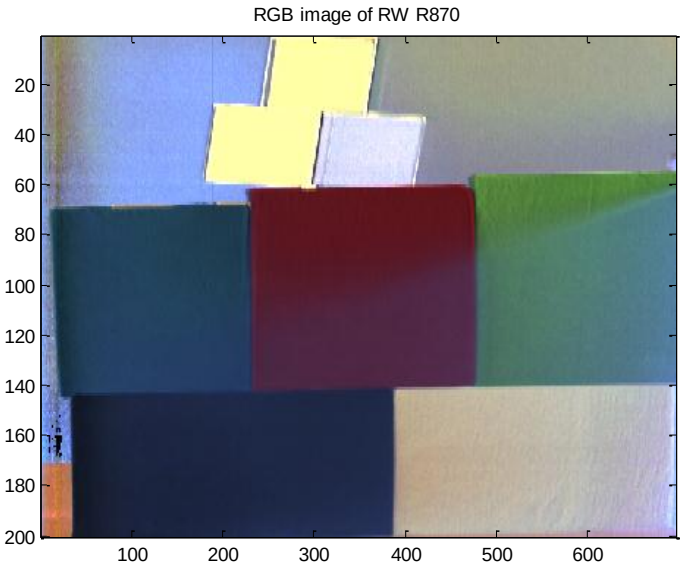
RGB image of RW R870
20
40
60
80
100
120
140
160
180
200
100
200
300
400
500
600

(a)

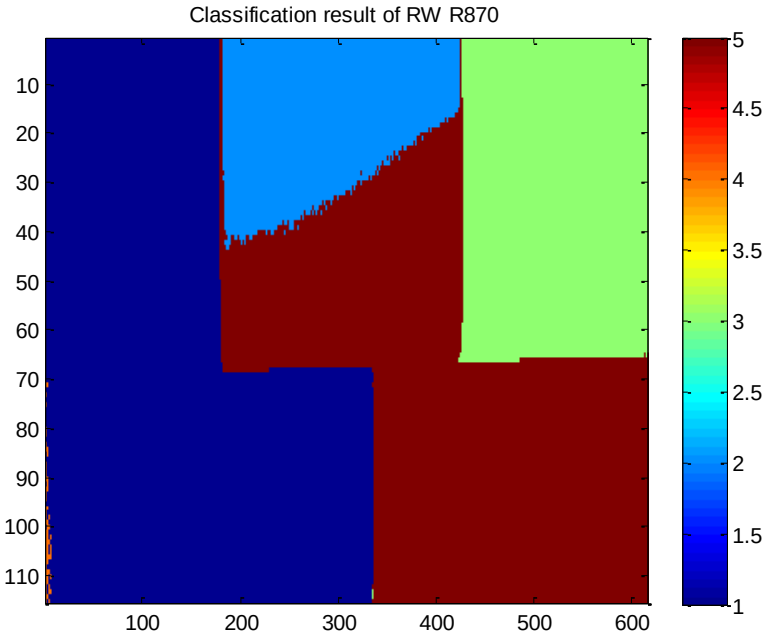
Classification result of RW R870
10
20
30
40
50
60
70
80
90
100
110
100
200
300
400
500
600
5
4.5
4
3.5
3
2.5
2
1.5
1

(b)

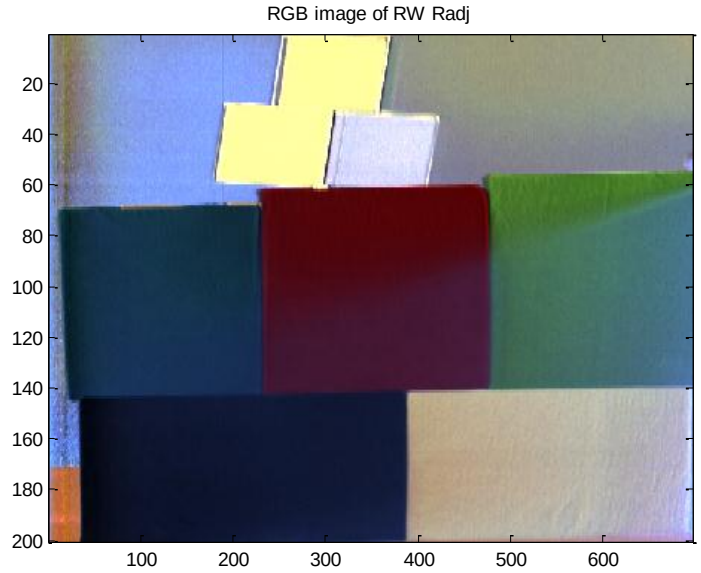

(c)

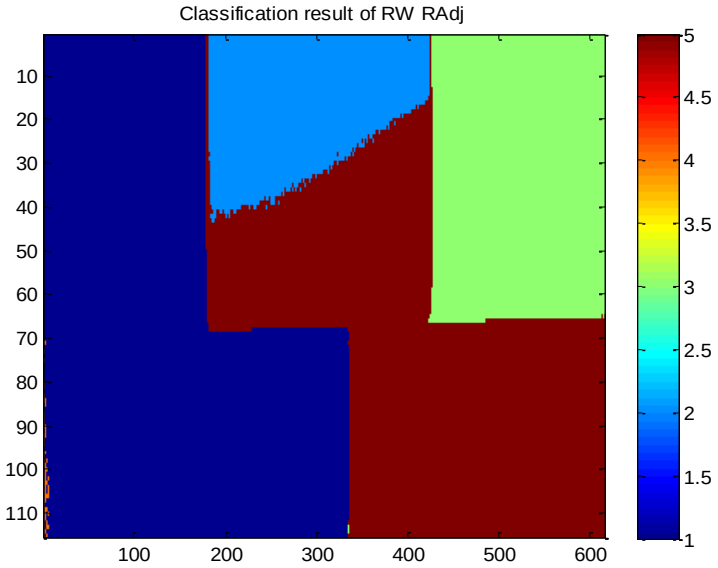

(d)

Figure 6-19 Shows the RGB image of (a) RW R870 and (c) RW RAdj data of 5 different coloured t-shirt data together with their classification results shown in ((c) and (d)) respectively.

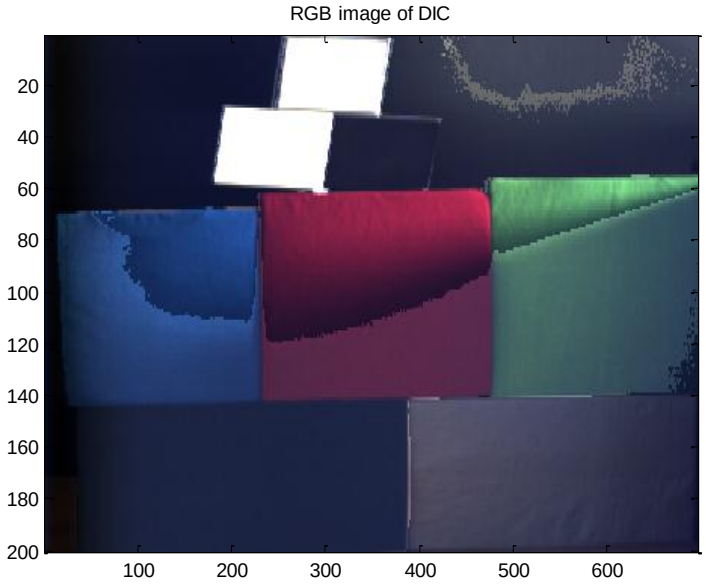

(a)

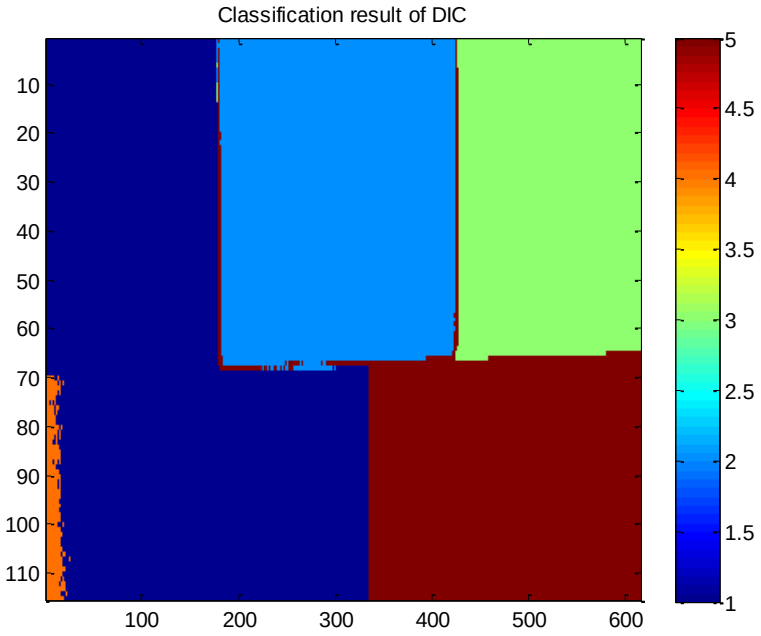

(b)

Figure 6-20 Shows (a) the RGB image of the 5 different coloured t-shirts after DIC correction and (b) its classification result with 58% accuracy. Note that the correction is far from perfect as it can be seen from the RGB image.

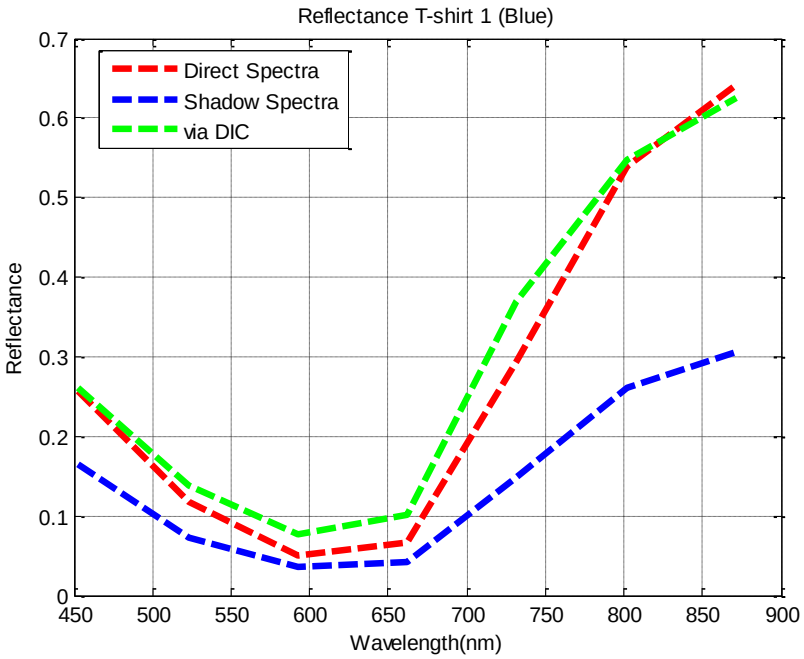
Reflectance T-shirt 1 (Blue)
Direct Spectra
Shadow Spectra
via DIC
Reflectance
Wavelength(nm)
0
0.1
0.2
0.3
0.4
0.5
0.6
0.7
450
500
550
600
650
700
750
800
850
900

(a)

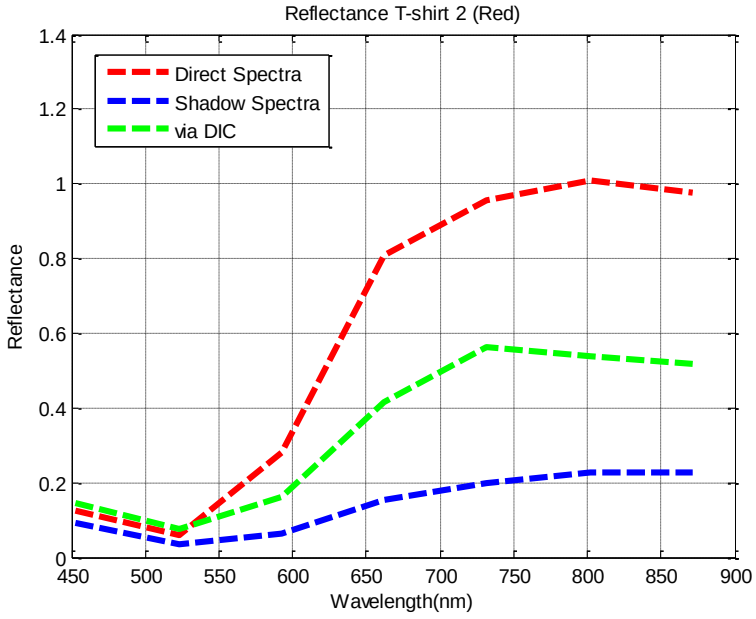
Reflectance T-shirt 2 (Red)
Direct Spectra
Shadow Spectra
via DIC
Reflectance
Wavelength(nm)
0
0.2
0.4
0.6
0.8
1
1.2
1.4
450
500
550
600
650
700
750
800
850
900

(b)

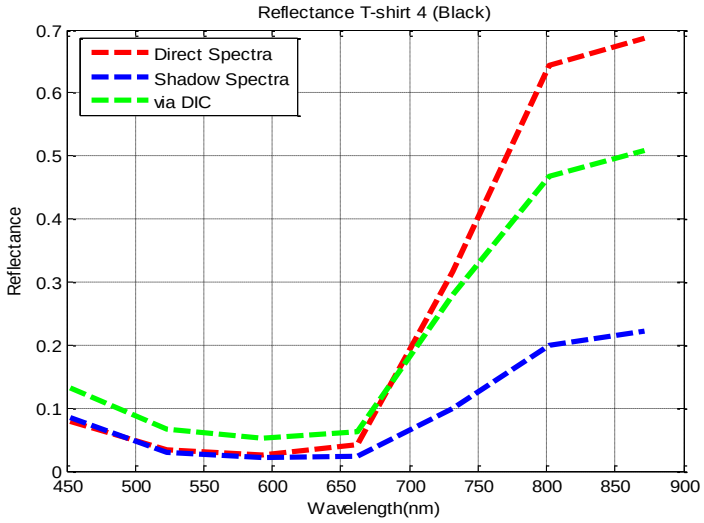

(c)

Figure 6-21 Shows the spectral plot of the apparent reflectance of the shadowed targets: without correction (RW) in blue, after correction by DIC in green, and comparison with that under direct illumination in red for (a) blue t-shirt (target 1), (b) red t-shirt (target 2) and (c) black t-shirt (target 4).

6.5.4 Conclusion

The Diffuse Irradiance Compensation (DIC) method has been proposed for reducing shadow effect by modelling the diffuse irradiance using a standard panel placed in the scene. It is found that the diffused irradiance compensation (DIC) is capable to compensate certain extent of illumination and shadow effects resulting in improved target inter-separability and much better classification accuracy.

A summary of the overall classification result for these two data sets of 10 and 5 t-shirt is given in Table 6-1. This study has demonstrated that RW data can achieve better classification result in comparison to the raw data that includes the sensor characteristics and illumination artefacts. This study also demonstrates that the naive spectral normalisation for 'flattening' illumination artefacts is unable to compensate shadows especially when the data consists of complicated geometry and background. This work has demonstrated that if

diffuse irradiance somehow can be estimated directly from the scene, the shadow compensation can be achieved much better than any known method reported in the literature.

Table 6-1 Summary of the classification results.

	Raw	RW	Norm	R870	RAdj	DIC
10 t-shirt data	38%	68%	50%	62%	62%	70%
5 t-shirt data	31%	43%	35%	35%	35%	58%

Although the DIC method shows the best classification performance there are still some areas which are needed to improve in order to make it more robust. In the following are some of the limitations of the present algorithm which are needed to attend in the future research:

(a) The DIC utilize shadow mask to differentiate between direct and diffuse reflectance. The implementation of shadow mask in this research is based on the threshold that is selected arbitrarily from the variance and mean maps. The selection of the threshold value varies somewhat dependent on the complexity of the scene. Too large of the threshold may include the direct illuminated pixels to be in the shadow area. Robust shadow segmentation is essentially important to avoid over or under-corrections.

(b) The DIC method models the diffuse irradiance by placing a standard panel in the scene such that it samples the diffused illumination directly from the scene. This will require user knowledge and arrangement to place the panel in the scene.

(c) Hyperspectral images always contain various degree or softness of shadows, and the presently DIC method does not take the softness of shadows into account. The present method employs the same extent of corrections over the entire image regardless of the shadow depth.

7 COLOUR TRANSFER LINEAR REGRESSION METHOD

The DIC method proposed in Chapter 6 works by modelling the diffuse irradiance of the scene using a standard panel in which it may not be practical in many real scenarios. Therefore, in order to overcome this limitation a linear regression (LR) method is proposed.

LR has been used widely in HSI processing to improve statistics of the hyperspectral imagery particularly when it is needed to repeat the measurement at different times (68). Variations due to sensor calibration errors, solar irradiance and atmospheric effects can impose errors on the interpretation of HSI imagery. In this chapter, the LR method has been adopted for the correction of shadows through the statistics of the image pixels under direct illumination. This methodology is also known as colour transfer which has been deployed in machine vision for colour constancy. This linear transformation adjusts the mean and the offset of the shadow characteristics to match with that of the fully illuminated pixels statistically.

Similar to that of the DIC method, this LR approach firstly segments the scene into shadow and non-shadow region using the same shadow masking method as presented in Chapter 6 and an example of the final shadow mask is given in Figure 7-1.

7.1 Linear Regression Method

The reflection intensity of targets under shadow is normally weak due to the relatively weaker diffuse irradiance impinging on them. However, for targets under direct illuminations the reflection is generally higher. Shadow compensation can therefore be achieved by applying a linear transfer between the fully illuminated pixels (direct_pixels) and shadowed pixels (shadow_pixels) for each band n in a statistical way using the equation as below:

$$Corrected\_shadow_n = m_n * (shadow\_pixels)_n + c_n \quad \textbf{(7-1)}$$

In this equation m_n is defined as,

$$m_n = \frac{std\_deviation \quad (direct\_pixels)_n}{std\_deviation \quad (shadow\_pixels)_n} \quad \textbf{(7-2)}$$

and c_n as,

$$c_n = mean \quad (direct\_pixels)_n - m_n * mean \quad (shadow\_pixels)_n \quad \textbf{(7-3)}$$

7.2 Experimental Setup

The data sets used for this experiment is the same as that used for the DIC experiments. To recall, the hyperspectral data with 88 bands of 10 and 5 different coloured t-shirts have been used as targets as shown in Figure 7-2 and Figure 7-3 in this experiment. In addition a 102 bands hyperspectral outdoor data set without the ground truth information is also included as shown in Figure 7-4. This data set was taken on a clear and sunny day on 2nd October 2011 at 2 pm.

QD classification has been employed here for the evaluation of the shadow removal performance and the training data and the ground truth are obtained from the data set of the same scene under direct illumination as explained in Chapter 6. Since the ground truth image is not available for outdoor data, the effectiveness of the shadow compensation using LR method is evaluated using the angle and distance metric of the apparent reflectance obtained before and after shadow correction with respected to that of the same targets under direct illuminations. Given 2 spectra vector, v_1 and v_2, the spectral angle mapper (SAM) metric can be defined as (22),

$$angle = \cos^{-1}\left(\frac{\sum_{n}^{N} v_{1,n} v_{2,n}}{\left[\sum_{n}^{N} v_{1,n}^2\right]^{1/2} \left[\sum_{n}^{N} v_{2,n}^2\right]^{1/2}} \right) \text{ where } n=band\ 1,....,N \quad \textbf{(7-4)}$$

Equation (7-4) involves normalization by the norm of the vectors thus making SAM to be insensitive to their magnitudes (72). Therefore, this SAM metric is normally used for the evaluation of the similarity between two vector spectra. The degree of dissimilarity in spectral shape is measure by the increase of the angle between the two vectors.

Euclidean Distance (ED) has also been employed for assessing the magnitude similarity of two vector spectra and it is given by (22),

$$ED(v_1, v_2) = \left[\sum_{n}^{N} (v_{1,n} - v_{2,n})^2\right]^{1/2} \text{ where } n=band\ 1,....,N \quad \textbf{(7-5)}$$

A small distance represents a close match between the two vector spectra.

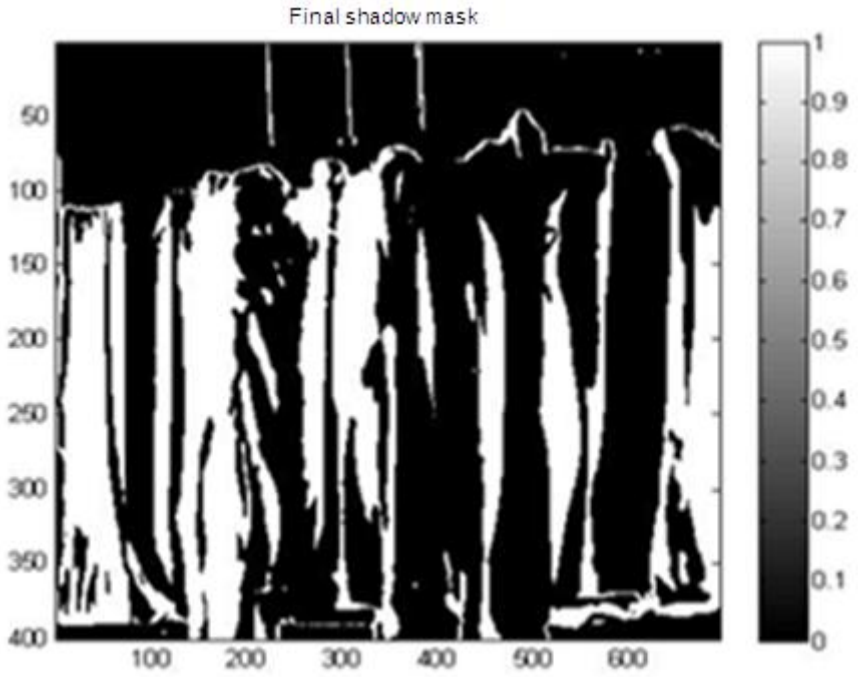

(a)

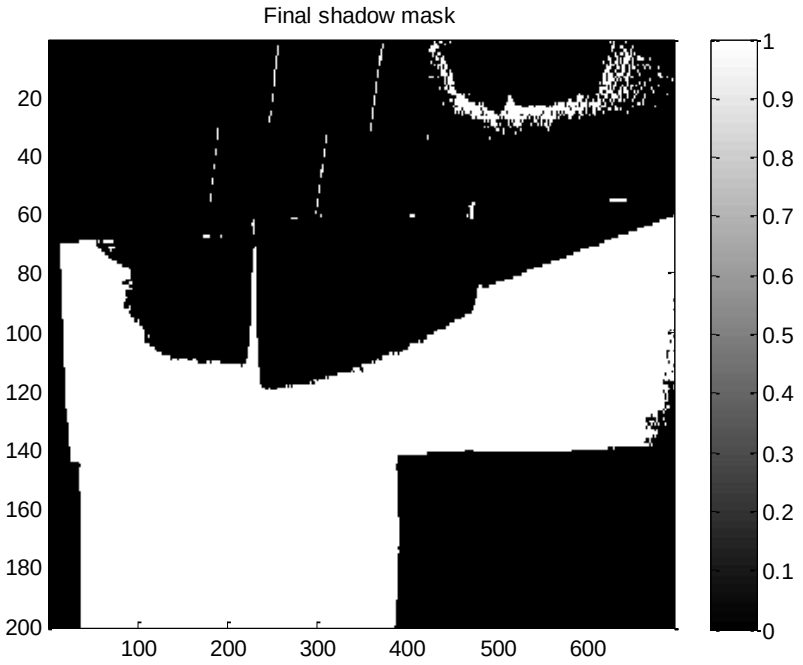

(b)

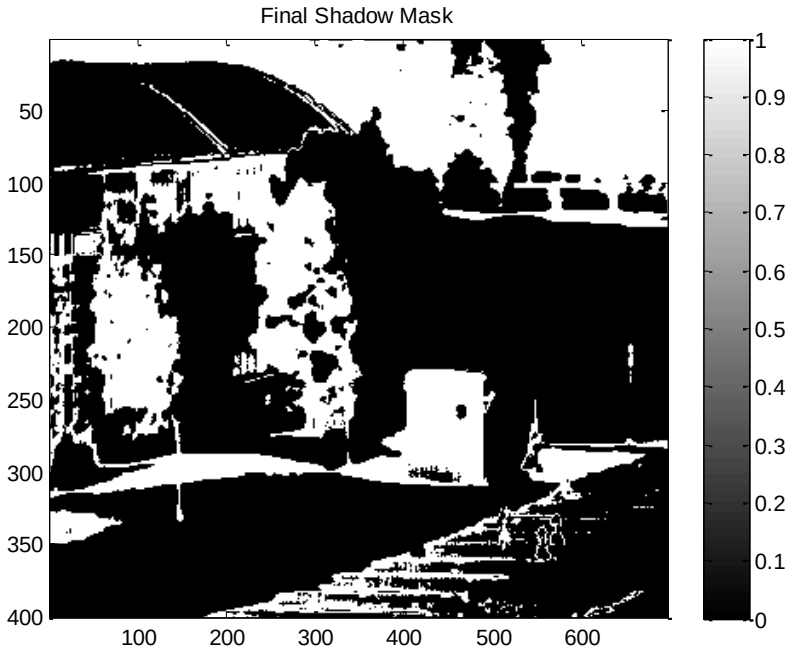

(c)

Figure 7-1 Shows the final shadow mask (bright areas) (a) for the 10 coloured t-shirt indoor data, (b) the 5 coloured t-shirt indoor data and (c) the outdoor scene data.

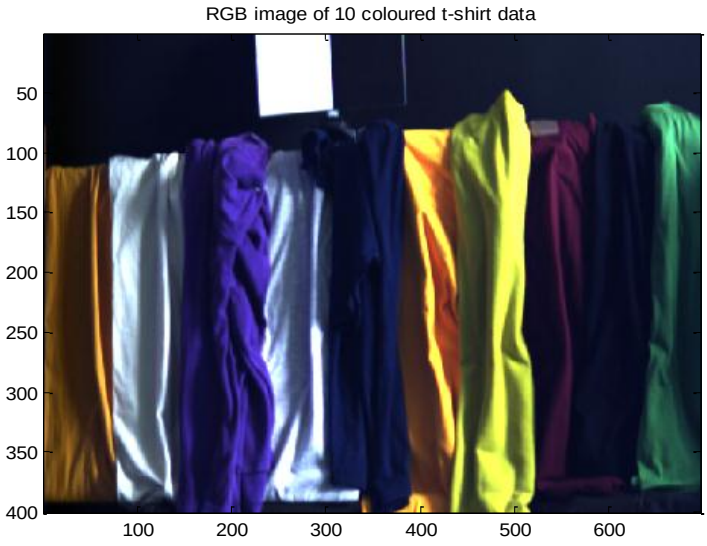

Figure 7-2 Shows the RGB image of a hyperspectral data with 88 spectral bands that consists of 10 different coloured t-shirts indoor data used in the LR experiment. This data set is similar to that used in the DIC experiment.

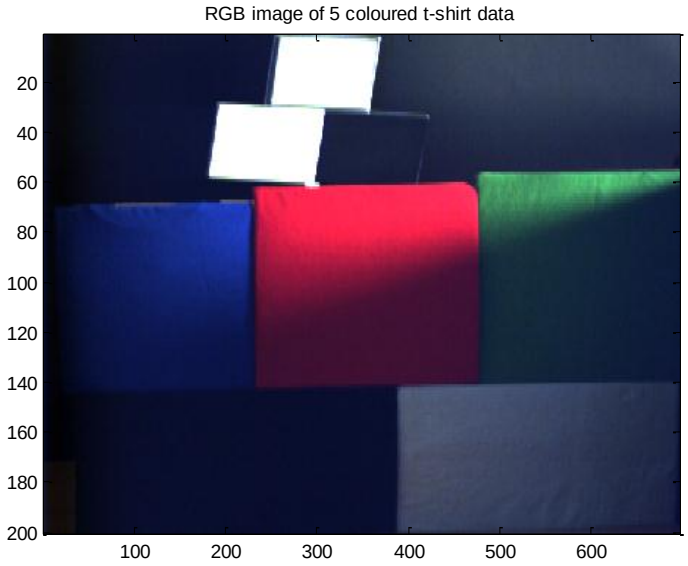

Figure 7-3 Shows the RGB image of a hyperspectral data with 88 bands that consists of 5 different coloured t-shirts indoor data used in the LR experiment. This data set is again similar to that in the DIC experiment.

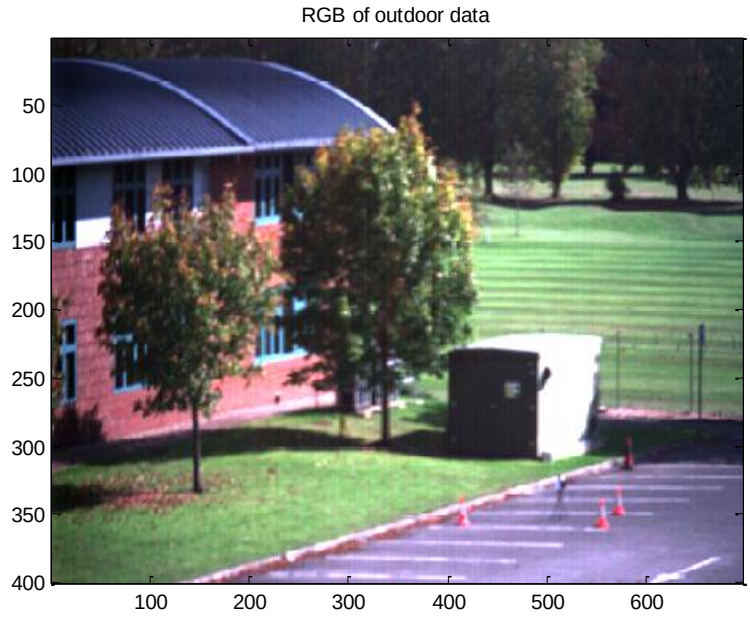

Figure 7-4 Shows the hyperspectral data of outdoor scene with 102 spectral bands taken at a range of ~100m on a clear and sunny day on the 2nd October 2011 at 2 pm GMT.

7.3 Linear Regression Result

7.3.1 Ten T-Shirt Indoor Data

The RGB image of the shadow compensation via LR method is shown in Figure 7-5. Recall that the classification accuracies of RW and DIC have achieved 68% (Figure 7-6 (a)) and 70% (Figure 7-6 (b)) respectively for this data set. However, it is seen that the LR method for shadow compensation has achieved 75% classification accuracy as shown in Figure 7-6 (c).

Figure 7-7 shows the spectral plot of 2 shadowed targets before correction RW (in blue), after correction via DIC (in green), LR (in light blue) methods and compared with that under direct illumination (in red). It is seen that the shadow compensated spectra by the LR method is closely resemble to that by the DIC correction. However, one advantage of using the LR method is that it is easier and simpler to apply in practise as it does not require prior knowledge of the diffuse irradiance. In the DIC method it requires the standard panel to be in the

scene while the LR uses the statistics to compensate for shadow effect on the hyperspectral images. However this may also mean that the LR method may be sensitive to the statistics of the scene, for example, the proportions of the shadowed and non-shadowed regions and the variability of targets in these regions.

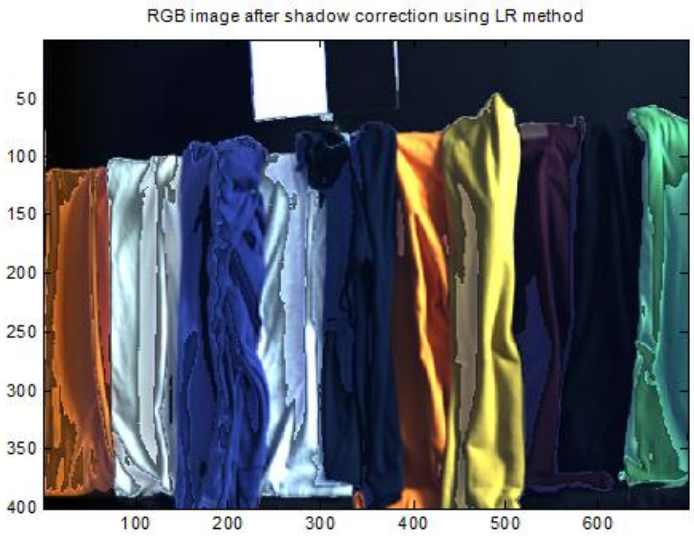

Figure 7-5 Shows the RGB image of the 10 coloured t-shirt data after LR compensation.

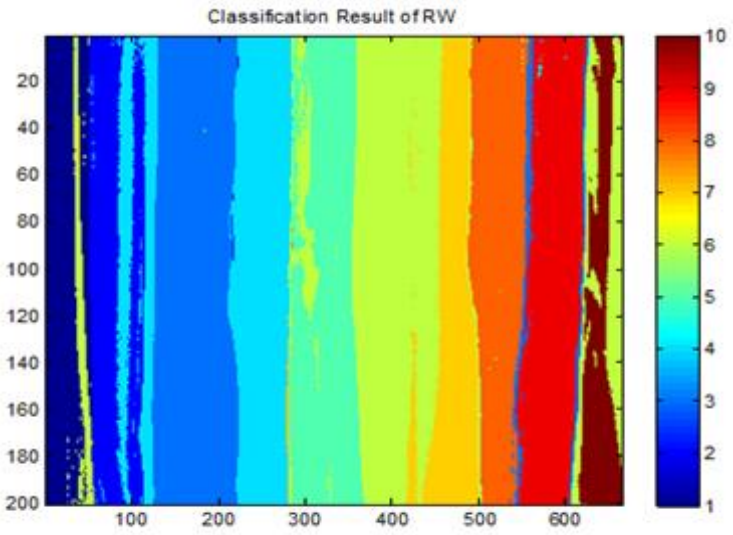

(a)

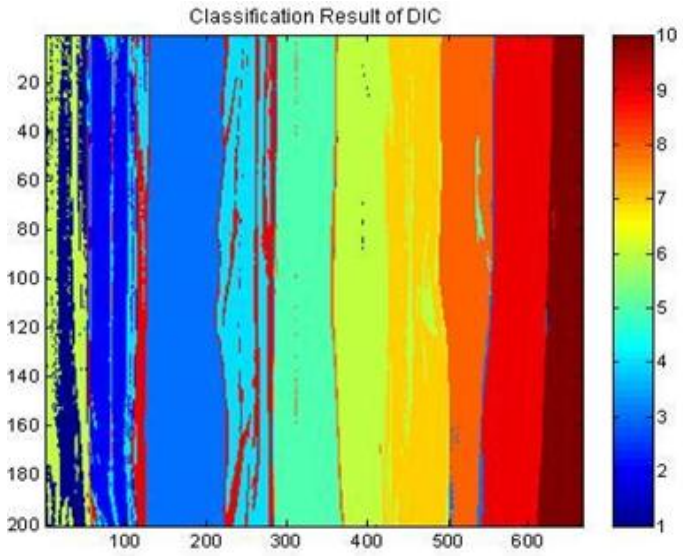

(b)

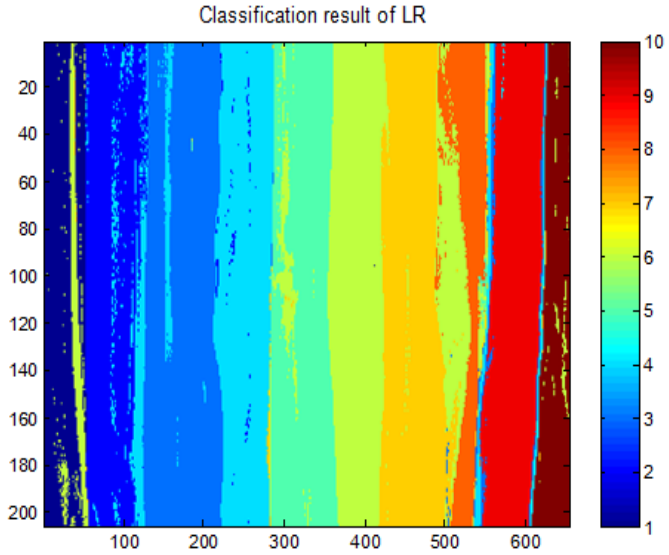

(c)

Figure 7-6 Shows the false colour images of the classification result for the 10 coloured t-shirt data (a) after RW correction with 68% accuracy, (b) after DIC compensation with 70% accuracy and (c) after LR compensation with 75% accuracy.

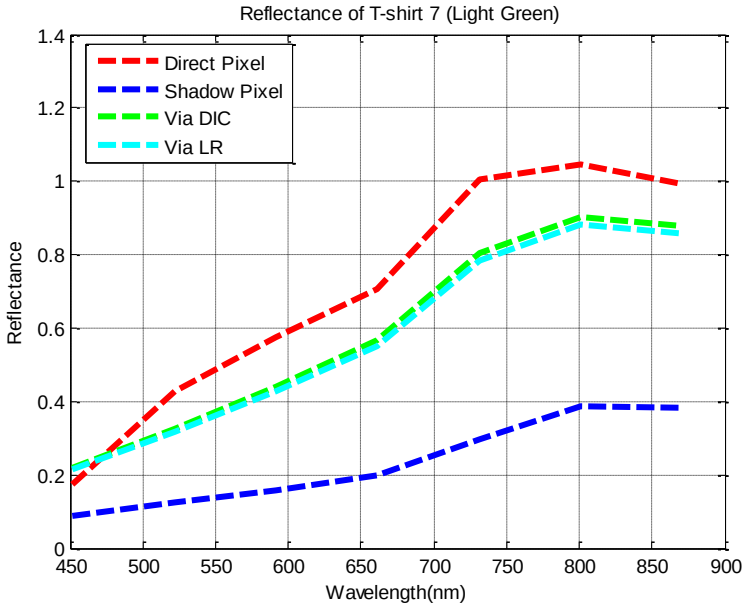

(a)

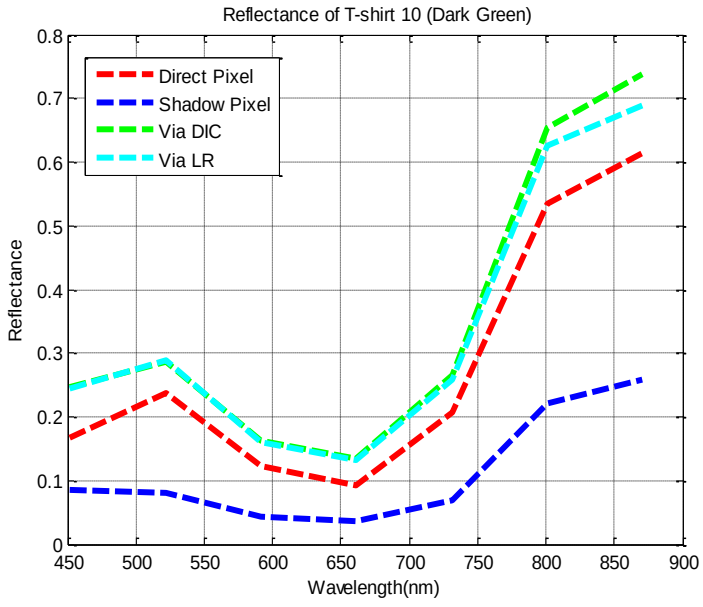

(b)

Figure 7-7 Shows the spectral plot of shadowed pixels for two targets of (a) light green t-shirt (target 7) and (b) dark green t-shirt target 10) obtained from i) apparent reflectance without correction (RW in blue), ii) after correction via DIC (DIC in green)), iii) after LR (in light blue) iv) under direct illumination(in red).

7.3.2 Five T-Shirt Indoor Data

Figure 7-8 shows the RGB image of the 5 t-shirt data after LR compensation. From the previous chapter it is recalled that the classification accuracy of RW and DIC methods have achieved 43% (Figure 7-9 (a)) and 60% (Figure 7-9 (b)) for this data set respectively. Half of the target class 2 (red t-shirt) has been misclassified as target class 5 in the untreated RW result. However, the QD classifier is capable to classify the target class 2 correctly after the DIC operation. The only error in this classification occurs in target 4. However, almost all targets can be classified correctly after the LR compensation (Figure 7-9 (c)). The LR method has achieved 97% of classification accuracy which demonstrates the effectiveness of LR method for shadow compensation.

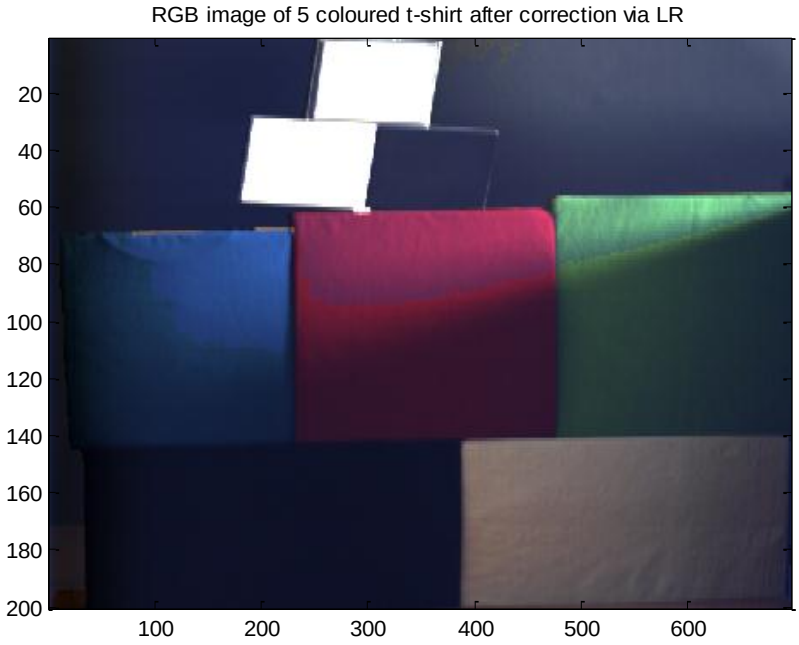

Figure 7-8 Shows the RGB image of the 10 coloured t-shirts data after LR operation.

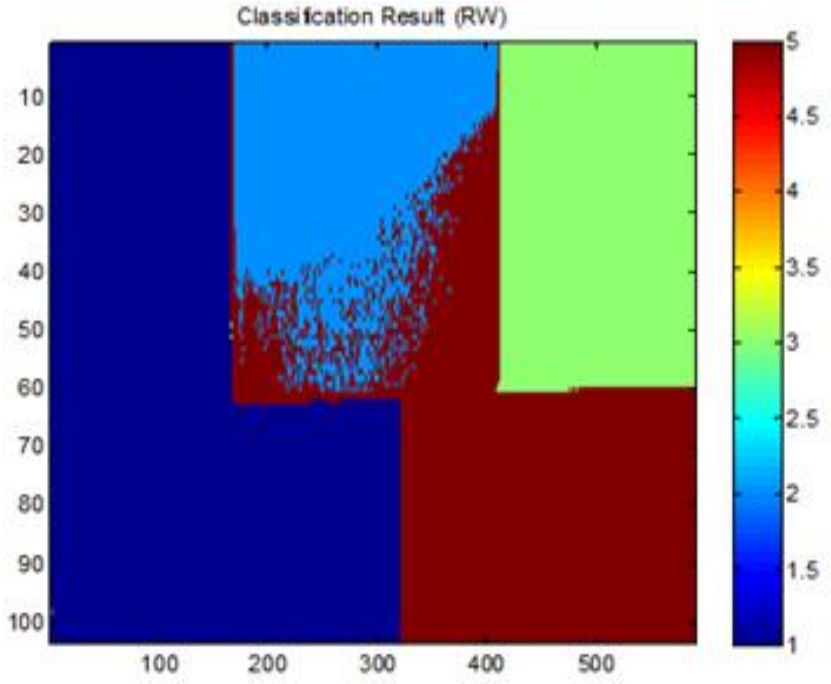
Classification Result (RW)
10
20
30
40
50
60
70
80
90
100
100
200
300
400
500
5
4.5
4
3.5
3
2.5
2
1.5
1

(a)

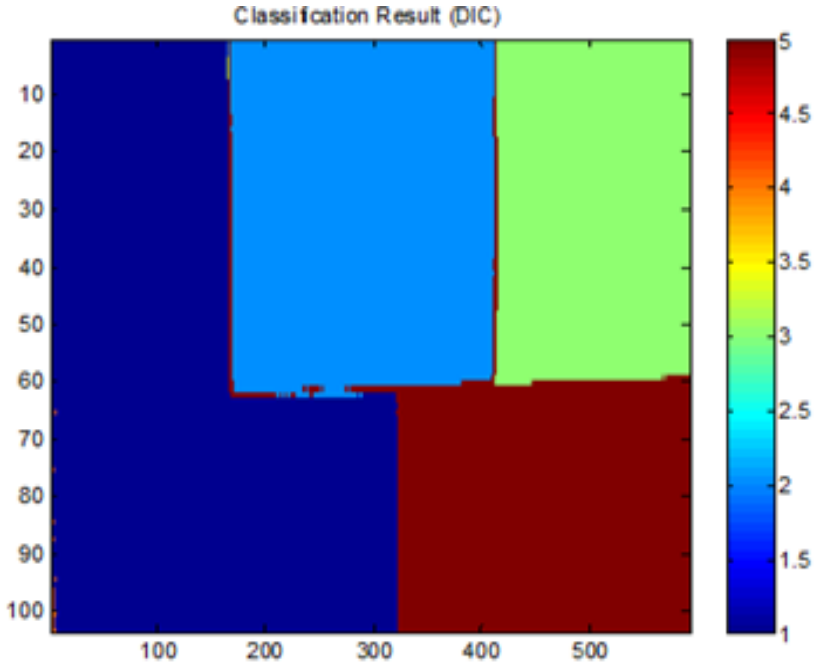
Classification Result (DIC)
10
20
30
40
50
60
70
80
90
100
100
200
300
400
500
5
4.5
4
3.5
3
2.5
2
1.5
1

(b)

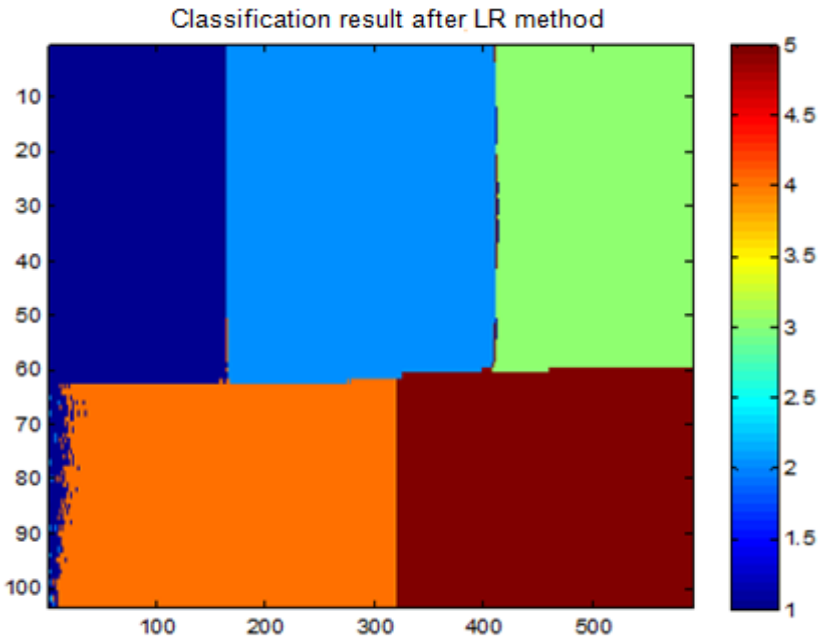

(c)

Figure 7-9 Shows the false colour classification result of the 5 coloured t-shirt data set after (a) RW with 43% accuracy, (b) DIC compensation with 58% accuracy and (c) LR correction with 97% accuracy.

Figure 7-10 shows the spectral plot of 3 selected shadowed targets before correction (RW), after correction via DIC and LR methods and a direct comparison with that of under direct illumination. From this graph, it is seen that the target reflectance under shadow has been improve after the correction and it is seen to be closer to the target reflectance under direct illumination than before the correction. Also, it is observed from this plot that the performance of the shadow compensations by the LR is very close to that of the DIC and more tests using a range of different data sets will be needed for a thorough understanding of the exact potential of the LR method.

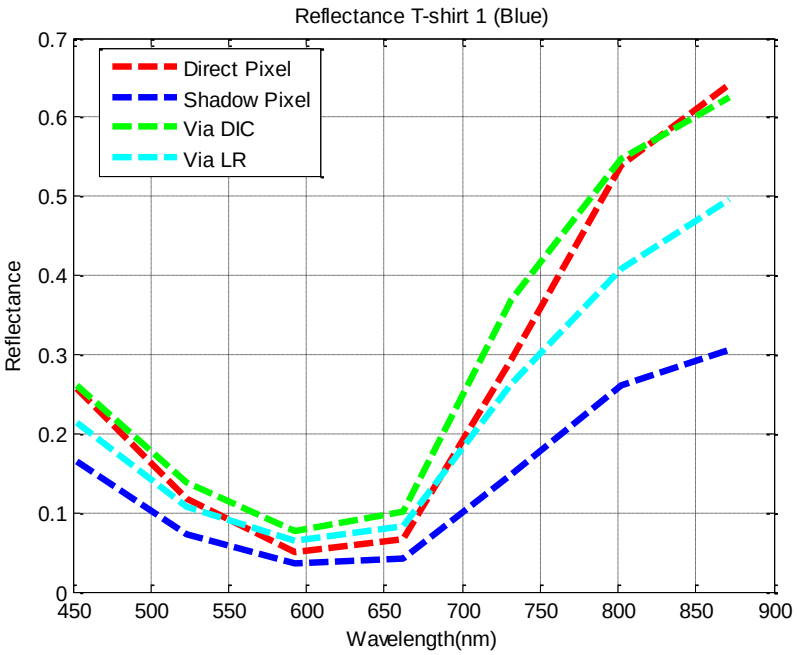
Reflectance T-shirt 1 (Blue)
Direct Pixel
Shadow Pixel
Via DIC
Via LR
Reflectance
Wavelength(nm)
0
0.1
0.2
0.3
0.4
0.5
0.6
0.7
450
500
550
600
650
700
750
800
850
900

(a)

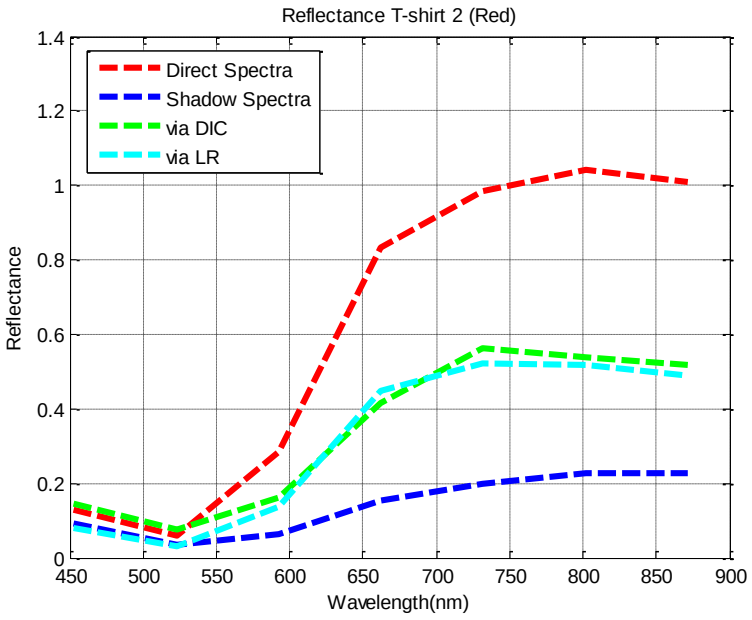
Reflectance T-shirt 2 (Red)
Direct Spectra
Shadow Spectra
via DIC
via LR
Reflectance
Wavelength(nm)
0
0.2
0.4
0.6
0.8
1
1.2
1.4
450
500
550
600
650
700
750
800
850
900

(b)

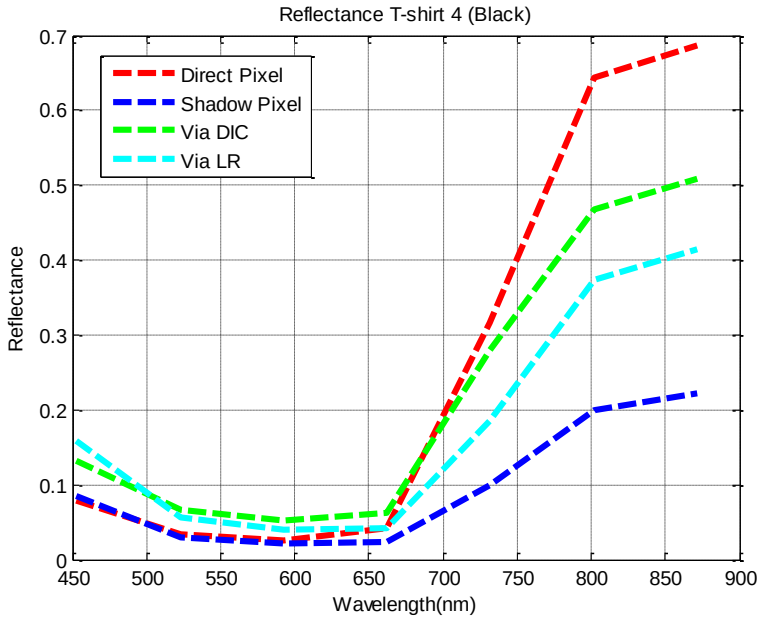

(c)

Figure 7-10 Shows the the spectral plot of the shadowed pixels from (a) blue t-shirt (target 1), (b) red t-shirt (target 2) and (c) black t-shirt (target 4) after i) no correction (RW in blue), ii) after correction by DIC (in green), iii) after LR (in light blue) and iv) the same targets under direct illumination.

7.3.3 Outdoor Data set

The SAM and the ED distance metrics have been used as the performance metric to evaluate the shadow compensation for the outdoor data set due to the lack of the target map information for this data set. Figure 7-11 shows the RGB image of the outdoor data after correction by using LR method, Table 7-1 and Table 7-2 show the SAM and the ED distance metric of the shadowed pixels before and after LR operation with respected to that under direct illumination. The smaller of the angle and distances may represent a better shadow compensation performance.

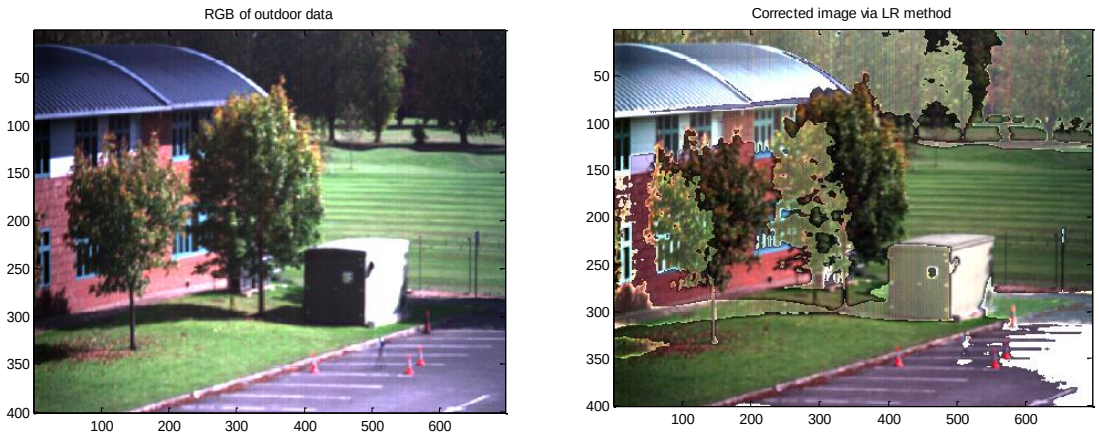

(a) **(b)**

Figure 7-11 Shows the RGB image of an outdoor scene (a) before and (b) after correction by the LR method.

The SAM result shown in Table 7-1 indicates an average of ~20% improvement on the shadow compensations, with rather significant improvements on the golf course, the bunker and the red bricks targets. There is relatively small change in the compensation of the grass spectra which gives ~3% improvement. In Table 7-2 it is also seen that the shape of the compensated spectra resembles quite closely to that of the grass and the lawn of the golf course. This is mainly due to the fact that the scene is dominated by the vegetation materials (grass, tree & lawn) and therefore the spectral statistics is skewed towards the most abundant materials in the scene. The ED distance measure as shown in Table 7-2 shows more significant improvements with average of ~57% closer to that of under direct illumination.

Table 7-1 The SAM of the outdoor data with respected to that under direct illumination.

	Grass	Bunker	Bricks	Golf	Average
Before correction	0.12°	0.36°	0.18°	0.18°	**0.20°**
After correction	0.12°	0.30°	0.12°	0.09°	**0.16°**
Percentage of improvement	3.35%	19.32%	33.09%	47.34%	**20.42%**

Table 7-2 The distance similarity for outdoor data.

	Grass	Bunker	Bricks	Golf	Average
Before correction	2.15	1.96	1.80	1.92	**1.96**
After correction	0.60	0.88	1.17	0.68	**0.83**
Percentage of improvement	72.35%	55.30%	34.69%	64.78%	**57.58%**

This enhancement can also been seen from the spectra plot depicted in Figure 7-12. The value and shape of reflectance that is under shadow almost match the direct reflectance as we can see in Figure 7.12 (a) and (d). However, from Figure 7.12 (b) and (e), although the shadow reflectance has been improved the shape tends to follow the major materials in the scene which is grass. The changes of the shape after the correction can be clearly observed within the band 500 to 700. This is due to the fact that this method is based on the statistic approach which is sensitive to the statistical distributions of objects in the shadow and non-shadow portions of the scene.

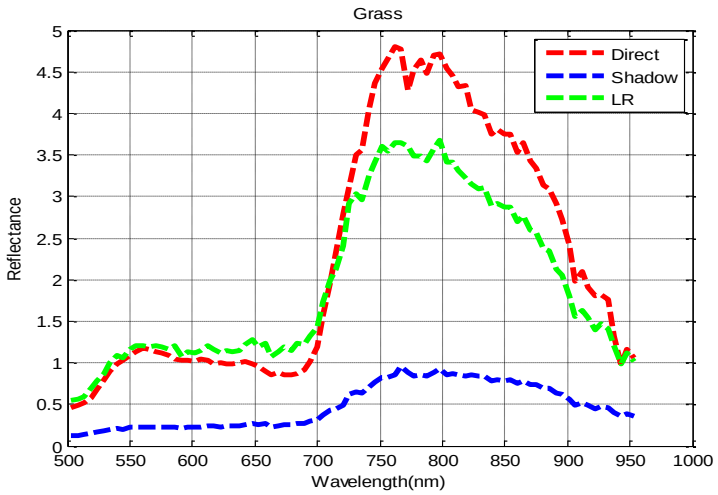

(a)

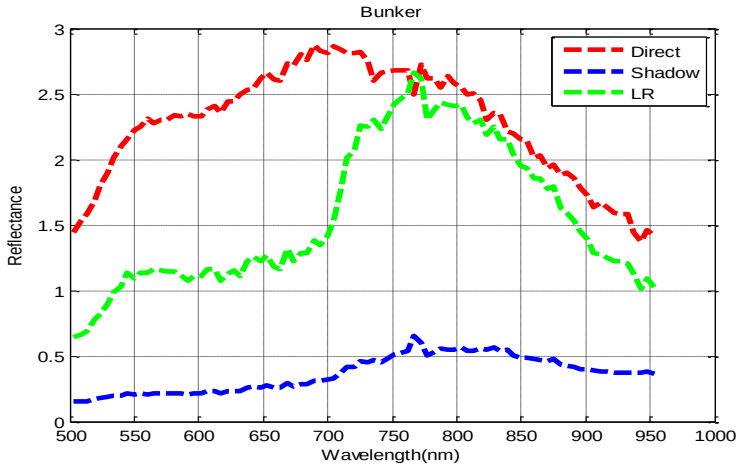

(b)

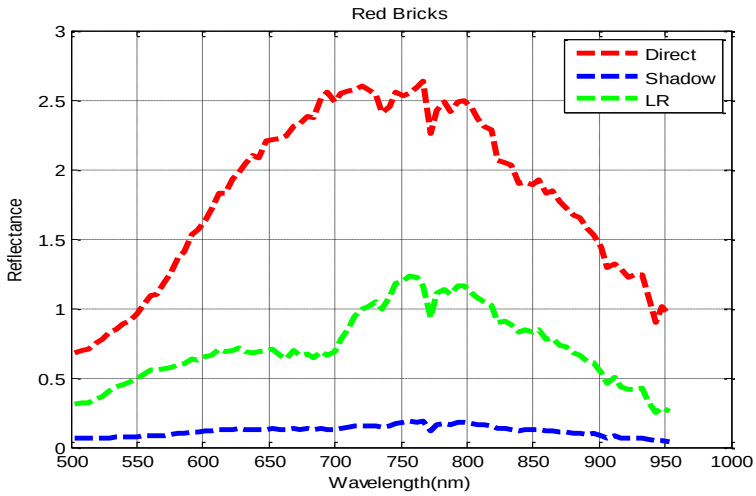

(c)

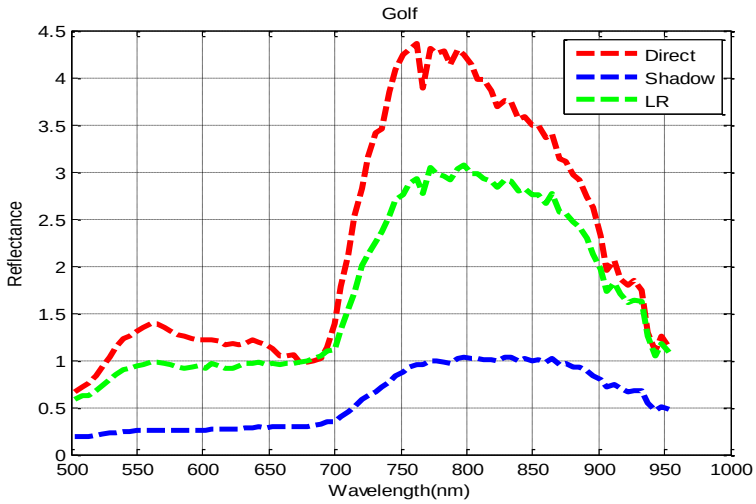

(d)

Figure 7-12 Shows the apparent reflectance of various targets (a) grass (b) bunker, (c) red bricks and (d) the lawn of the golf course before (in blue) and after (in green) correction by LR and to compare with that under direct illumination (in red).

7.4 Conclusion

The DIC method has shown some improvements for shadow compensation in hyperspectral processing. This method requires a standard panel to probe the diffuse irradiance from the scene which is difficult to realise in practise. Alternatively, a new method which transfers statistics from the non-shadow region into the shadow region through Linear Regression (LR) method has been proposed to achieve illumination invariance and shadow compensation for hyperspectral imagery processing. Since this method is based on statistics the performances will be sensitive to the statistical distributions of objects in the shadow and non-shadow portions of the scene.

Preliminary classification results for two indoor data sets are given in Table 7-3 and it is found that:

(a) The LR shadow compensation improves classification accuracy by ~7% and ~5% better that of the RW and DIC method for the 10 coloured t-shirt indoor data respectively.

(b) The LR method is found to improve ~54% and ~39% with respected to the RW and the DIC method for the 5 different coloured t-shirt indoor data respectively.

(c) The LR method attains on average of about 0.04 degree better than the RW over 4 targets in an outdoor scene which is dominated by trees and lawn.

(d) The LR method reduces the distance by ~57% over 4 targets in the outdoor scene

Although the LR method shows the best classification accuracy from these few data sets without the need of the diffuse irradiance information, there are limitations of the technique which will be addressed in the future work:

(a) This method utilizes the same shadow masking technique which requires threshold in the variance and the spectral means as in the DIC method.

(b) This method does not correct the shadow according to the depth or softness of the shadow.

(c) The performance of the LR method is strongly dependent on the distributions of the target and backgrounds in the shadow and non-shadow regions.

Most of these limitations will be addressed in the next chapter by using a more robust illumination independent processing for shadow compensation in hyperspectral imagery.

Table 7-3 The overall result of classification accuracy.

	Raw	**RW**	**DIC**	**LR**
10 t-shirt data	38%	68%	70%	75%
5 t-shirt data	31%	43%	58%	97%

8 SPECTRO-POLARIMETRY METHOD (SP)

Most of the previous effort on shadow compensation has been based on image processing techniques. In this work we have attempted a new approach of shadow compensation for hyperspectral imagery by employing a mixture of Electro-optical (EO) hardware and image processing methods. The EO hardware method is based on the spectral polarization and it is also known as spectro-polarimetry technique (SP). Spectro-polarimetry can be deployed in a system which polarises the light for the illumination and samples the properties of the reflected light over some defined polarised spectral regions (79). In this work we have adopted the illumination by a single light source and the reflected light is collected under a range of polarisation angles. This technique does not require the standard panel to sample the diffuse irradiance, and the shadow mask can be deduced more accurately by using two HSI images with and without polarizer.

The principle underlying in this work makes use of the fact that the reflections from objects under diffuse irradiance is relatively more unpolarised than that under direct illumination. We have employed Spectral Angle Mapper (SAM) algorithm to differentiate between the shadowed and fully illuminated pixels. SAM measures the spectral angle for each pixel between the non-polarized and polarized images. These SAM values represent the fraction of the diffuse irradiance across the images and they are then used for correcting shadows of the hyperspectral images. This method is evaluated using QD classification and spectral similarity measure, such as angle and distance metric. The results of indoor and outdoor tests have shown that the direct and diffuse irradiated pixels can be differentiated by using the SP technique.

8.1 Introduction and background

Hyperspectral imaging systems collects the spectral energy which is emitted or reflected from the target in hundreds or more contiguous spectral channels. However, by combining spectral and polarimetric techniques, more information

about the scene such as surface features and shading can be gathered. The polarization technique was first used for stellar and planetary astronomy applications (70). It has been extended to standard (non-hyperspectral) image processing where a polarizer is used to sample the distribution of the reflected radiance from a target (76). Early work has applied polarimetric to separate the diffuse and specular components of reflection from the surface of objects (71, 72) so to improve the colour and brightness of the target. Lin et al. has developed a method to work with a polarization sensitive camera to separate shadows from different colour images (73). Wellems and Bowers have reported that the polarization technique has improved the target acquisitions (74) leading to better target separability and thus enhanced classification accuracy. Nowadays, there are many conventional broad band RGB cameras have been fitted with a polarizer filter for improving image quality, such as to reduce sky light effect or glare. This is exactly the same as the polarized sun glasses which have been commonly employed to minimize the specular reflection from the sun entering into our eyes.

Optical materials interact with light through scattering, absorbing or refractive action (75). They can be glass, plastics or metallic material such as silver or aluminium and scattering materials for the display or filters (30). Light wave transverses the E and H fields in all directions and when it passes through optical materials such as glass, the transmission of a particular E-H orientation is more preferable than others (75) and it is known as polarization effects. Shiny surfaces, such as mirror-like surfaces, have high specular reflection properties with the reflected beam highly polarised parallel to the surface of the reflector. Rough surfaces, or group of objects that are closely packed together, will exhibit low polarized reflections (72). Sky light resulting from atmospheric scattering of the solar irradiance will exhibit fewer polarisations than that of the direct solar light.

In 1852, the four Stokes vectors have been developed by Sir George Gabriel Stokes for the description of polarized or partially polarized light based on the intensity measurement defined as (80):

$$S = \begin{bmatrix} s_0 \\ s_1 \\ s_2 \\ s_3 \end{bmatrix} = \begin{bmatrix} \left\langle |E_x|^2 \right\rangle + \left\langle |E_y|^2 \right\rangle \\ \left\langle |E_x|^2 \right\rangle - \left\langle |E_y|^2 \right\rangle \\ \left\langle E_x E_y^* \right\rangle + \left\langle E_x^* E_y \right\rangle \\ -i\left\langle E_x^* E_y \right\rangle + i\left\langle E_x E_y^* \right\rangle \end{bmatrix} \propto \begin{bmatrix} I_0 + I_{90} \\ I_0 - I_{90} \\ I_{45} - I_{135} \\ I_R - I_L \end{bmatrix} \quad \textbf{(8-1)}$$

In this equation, s_0 is the total intensity of light, s_1 is the difference between horizontal and vertical polarization, s_2 is the difference between linear and non-linear polarization and s_3 is the difference between right and left polarization, the $E_{(x,y)}$ denote the electric field at (x,y). Note that the polarization of the reflected light is dependent on the propagation of radiation from the source to the scene and the scatter of the light by objects to the sensor. The exact content of the atmosphere, the illumination and viewing geometries may affect the polarization of the reflected beam. Multiple scattering by nearby objects of the scene can also affect the polarization of the reflected beam that ultimately sensed by the camera. To measure the entire Stokes polarization parameter one will need several sets of polarizer to incorporate with the HSI system.

8.2 Spectro-Polarimetry Technique (SP) for shadow compensation

The HSI system senses the reflections from both the diffuse irradiance, $E_{diffuse}$ and the direct irradiance, E_{direct}. The total flux of illumination is the sum of the direct and diffuse irradiance,

$$E_g = E_{direct} + E_{diffuse} \quad \textbf{(8-2)}$$

Polarisation of light can be sensed through a polarizer (82) and this is set up in our hyperspectral imaging system as shown in Figure 8-1. At a certain polarisation angle this polarizer filters the reflections due to the direct illumination E_{direct}. Shown in Figure 8-2 are the mean spectra of the white standard panel taken with and without polarizer. The polariser is set at 90

degree and it is seen that the polarisation varies non-linearly as functions of wavelength.

Two hyperspectral data, indoor data with 88 bands and outdoor data with 102 bands, are taken with and without the polarizer filter. The basic assumption in this experiment is that there is a difference in the polarization properties between direct and diffuse illumination. Therefore, the spectral contrast between the non-polarized and polarized images, denoted by I_{NP} and I_P respectively, can be evaluated by using measures such as Spectral Angle Mapper (SAM). Let x be the pixel vector for images I_{NP} and I_P for N bands, then the SAM algorithm is given as,

$$SAM(x) = \cos^{-1}\left(\frac{\sum_{n}^{N} I_{NP}(x)_n I_P(x)_n}{\left[\sum_{n}^{N} I_{NP}^2(x)_n\right]^{1/2}\left[\sum_{n}^{N} I_P^2(x)_n\right]^{1/2}} \right) \quad where\ n=band\ 1,...,N \tag{8-3}$$

SAM measures the spectral contrast between the non-polarized images, I_{NP}, with respected to the polarized image, I_P. This value is then normalised over the scene such as:

$$Scaled\ \_SAM(x) = 1 - \frac{SAM(x) - \min(SAM)}{\min(SAM) - \max(SAM)} \tag{8-4}$$

This Scaled_SAM values represents the extent of the reflections due to the diffuse irradiance in each pixels of the scene. Thus the shadow pixels for n bands can be corrected by re-scaling the scene by the Scaled_SAM values together with brightness compensation:

$$Corrected\ \_shadow_{x,n} = \frac{imageNP_{x,n}}{Scaled\ \_SAM_x} + \left(imageNP_{x,n} - imageP_{x,n}\right) \tag{8-5}$$

Figure 8-1 Shows the polarization set up in our system: a polarizer is is placed on the top of the camera's objective lens.

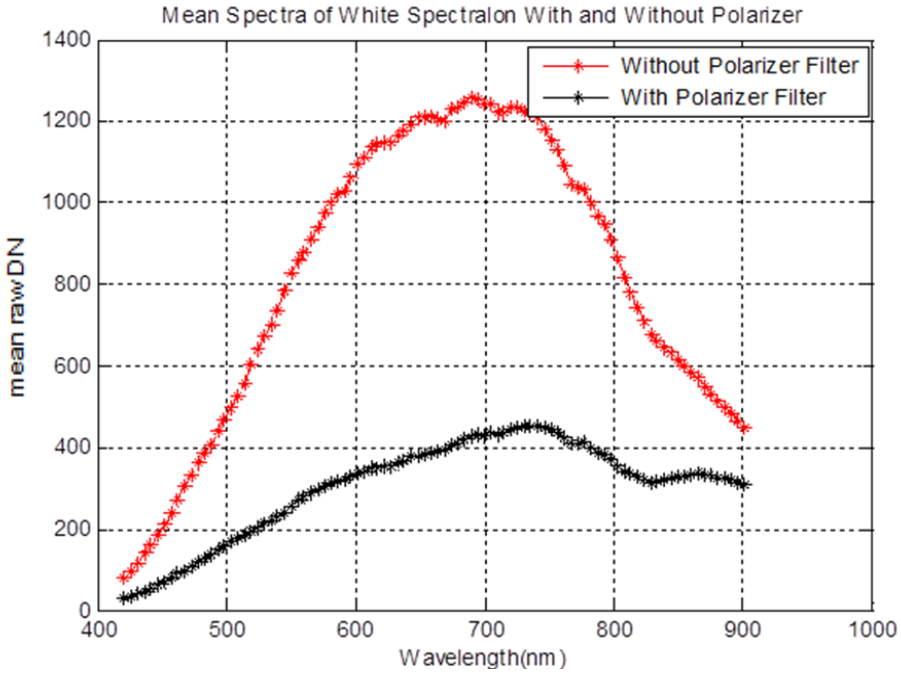

Figure 8-2 Shows the plot of the mean spectra from the white standard panel taken without and with (90degree) polarizer filter.

8.3 Experimental Setup

Two types of data sets, indoor and outdoor set, have been used for this experiment. The indoor data involves two sets data with 4 and 10 coloured t-shirts as targets, and two outdoor data sets with the lawn and a bunker as targets. All data sets have been taken without and with polarizer at various angles of polarization in this experiment. Figure 8.3 (a) shows the illumination source for taking the indoor data and (b) the 4 coloured t-shirts targets. The shadow is casted by an object placed between the target and the light source which is illuminated from one side of the scene. The shadow is casted such that it is deeper at the far left (on the green t-shirt) and softer towards the right (on the red t-shirt). The experimental set-up for the 10 coloured t-shirts data is similar to that in the previous DIC and LR experiments. The RGB images of 10 coloured t-shirts data is given in Figure 8-4.

Figure 8-5 and Figure 8-6 depict the RGB images of the outdoor lawn and bunker data sets which were taken on a clear and sunny day. The shadow of the lawn data is casted by the trees. The back side of the bunker is in the shade and the colour cannot be seen clearly from the raw data. Three standard panels consisting of the white and black spectralons, are also placed in both the indoor and outdoor scene for the E_{direct} estimation.

(a)

(b)

Figure 8-3 Shows the RGB picture of (a) the illumination Halogen lamp and the background, (b) the 4 t-shirt target and the shadow casted by a piece of cardboard placed at the left hand side of the targets.

Figure 8-4 Shows the RGB image of the 10 coloured t-shirt scene.

(a)

(b)

Figure 8-5 (a) Shows the RGB picture of the lawn that was taken on clear and sunny day at 1 pm and (b) shows the sky condition during the experiment.

(a)

(b)

Figure 8-6 (a) Shows the RGB image of the bunker that was taken on a clear and sunny day at 1 pm and (b) shows the environment condition of the scene.

8.4 Scaled SAM Result

The first step in the SP technique is the evaluation of the Spectral Angle Mapper (SAM) between the I_{NP} and I_P. Figure 8-7 shows the RGB images (a) without polarizer (I_{NP}), (b) with polarizer (I_P) and (c) the scaled_SAM map between I_{NP} and I_P for the 4 coloured t-shirts image. The scaled_SAM map shows a range of values in which the deep shadow is indicated by very small scale and it is presented in blue in the figure. While those pixels under direct illumination is presented by high SAM values shown in red colour in the figure. It is also perceived that the SAM of the polarized image is capable to detect the shadow pixels from the 10 coloured t-shirt data as shown in Figure 8-8. Note that this method can detect minute shadows such as the self-shadow due to wrinkles on t-shirt which can also easily be detected by this technique.

The same method also can detect shadows for the outdoor scene, as shown in Figure 8-9 and Figure 8-10. The pixels that are illuminated by the sky light is presented in blue colour on the SAM scaled map. A similar result has also been seen from the bunker data in which the back side of the bunker, and the near side of the car image, have been identified as shadows.

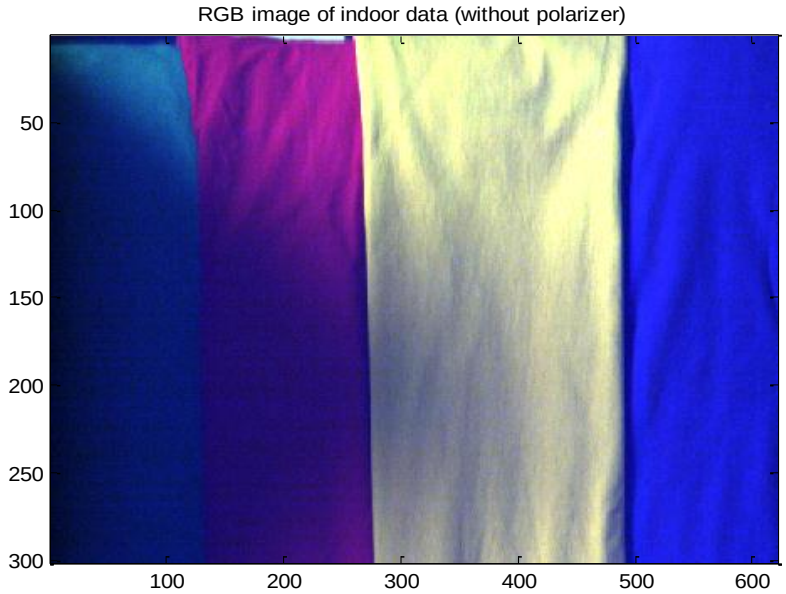

(a)

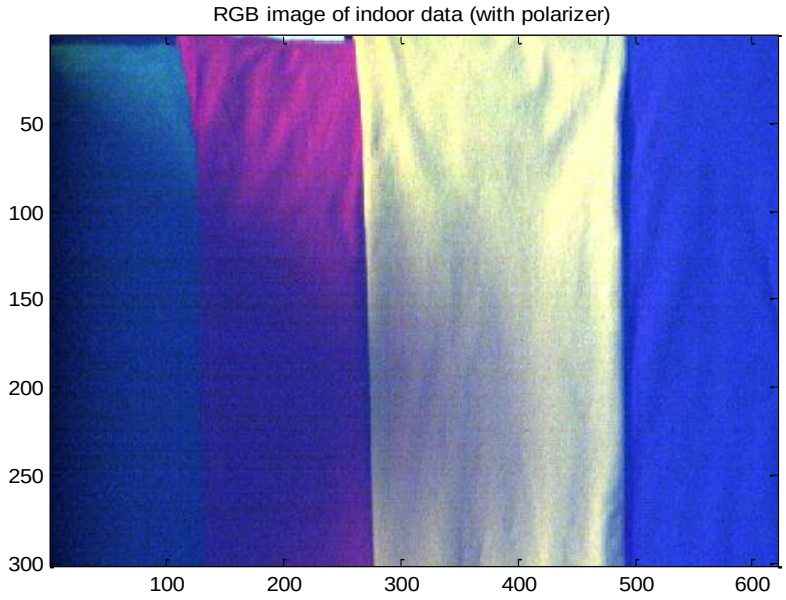

(b)

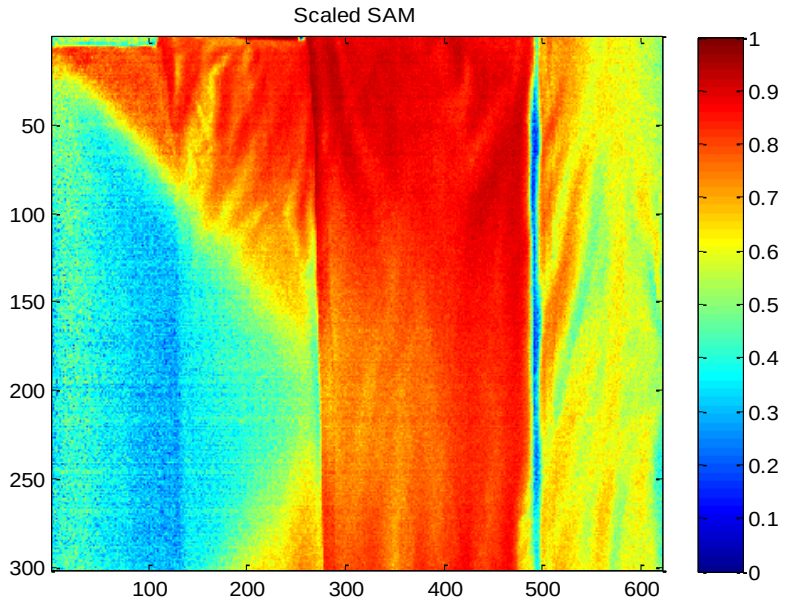

(c)

Figure 8-7 Shows the RGB images (a) without polarizer (I_{NP}), (b) with polarizer (I_P) and (c) the false colour scaled_SAM result of these two images for the indoor scene.

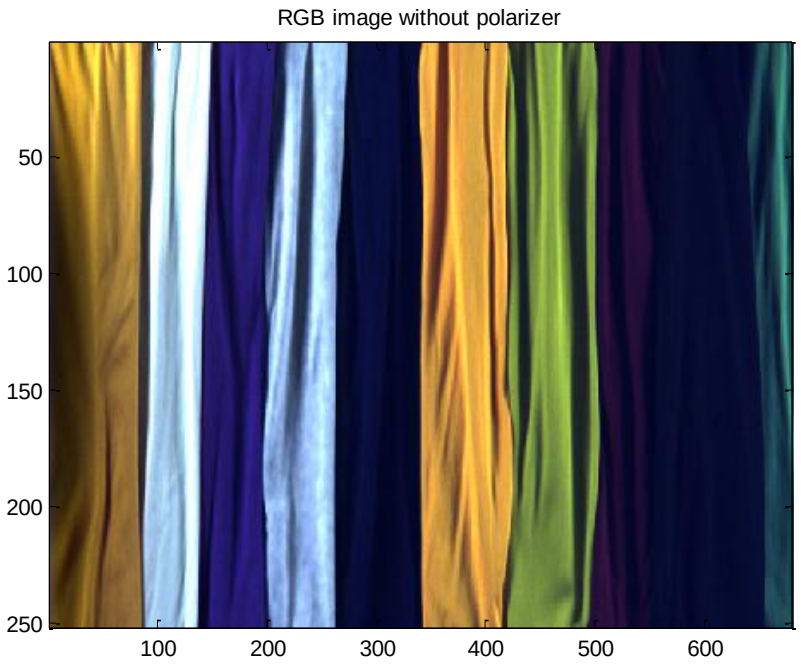
RGB image without polarizer
50
100
150
200
250
100
200
300
400
500
600

(a)

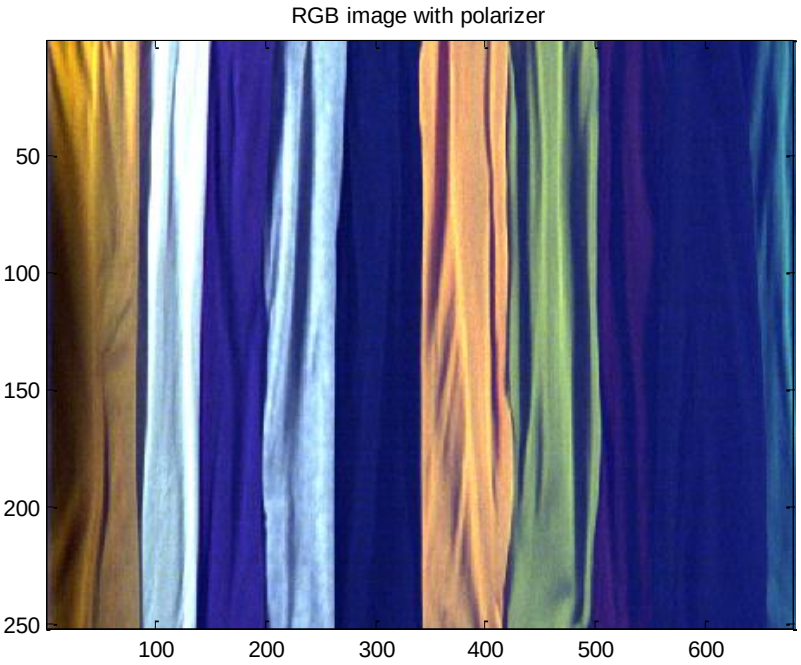
RGB image with polarizer
50
100
150
200
250
100
200
300
400
500
600

(b)

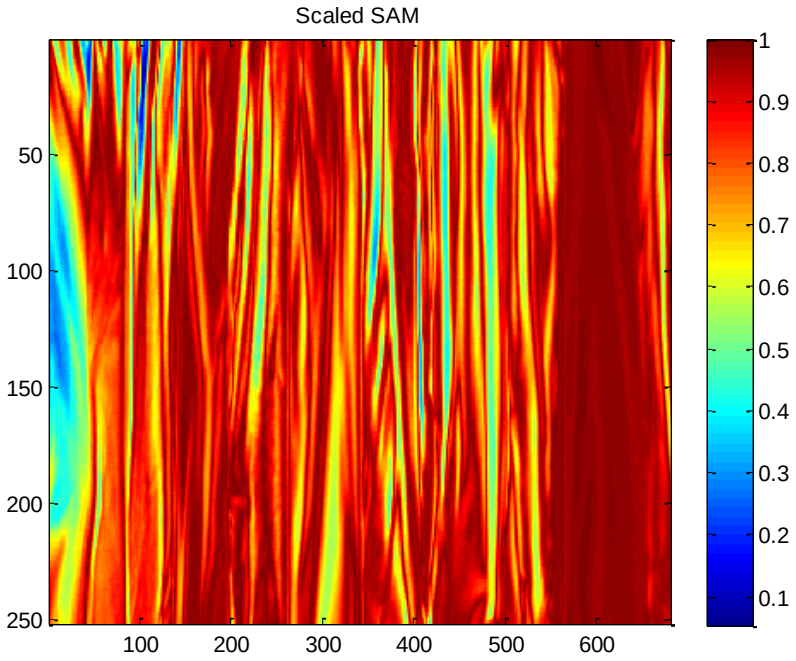

(c)

Figure 8-8 Shows the RGB images (a) without polarizer (I_{NP}), (b) with polarizer (I_P) and (c) the false colour scaled_SAM result of these two images for the10 coloured t-shirt indoor data. Note that the shadow is identified in blue.

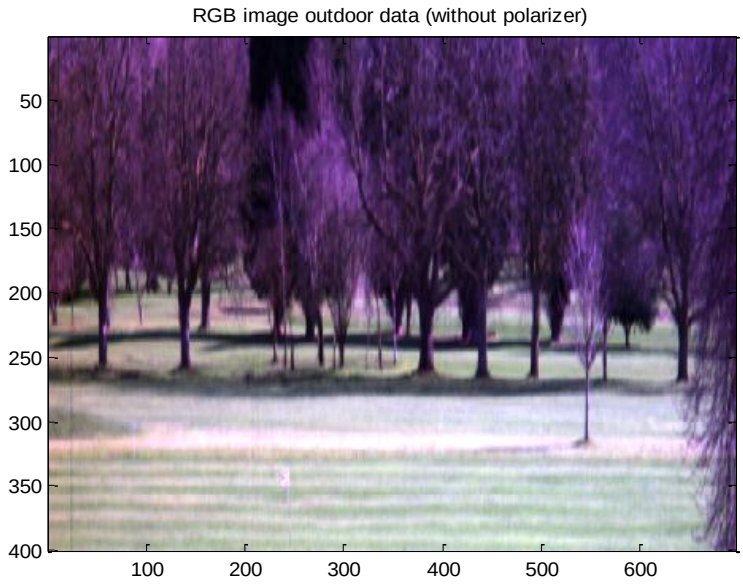

(a)

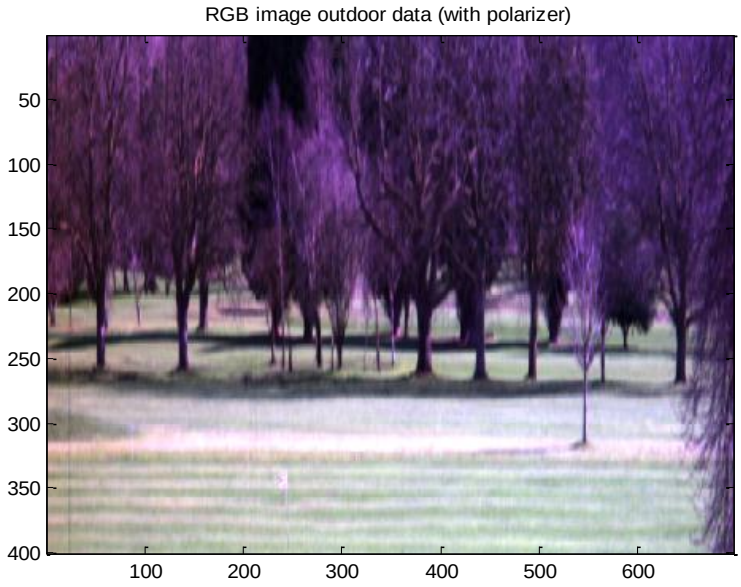

(b)

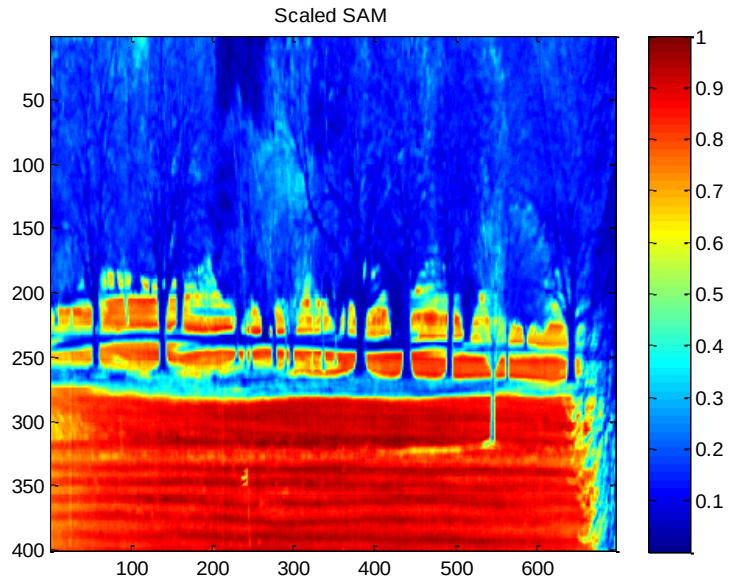

(c)

Figure 8-9 Shows the RGB images (a) without polarizer (I_{NP}), (b) with polarizer (I_P) and (c) the false colour scaled_SAM result of these two images for the lawn outdoor scene. Note that all trees and part of the lawn have been identified as shadows correctly.

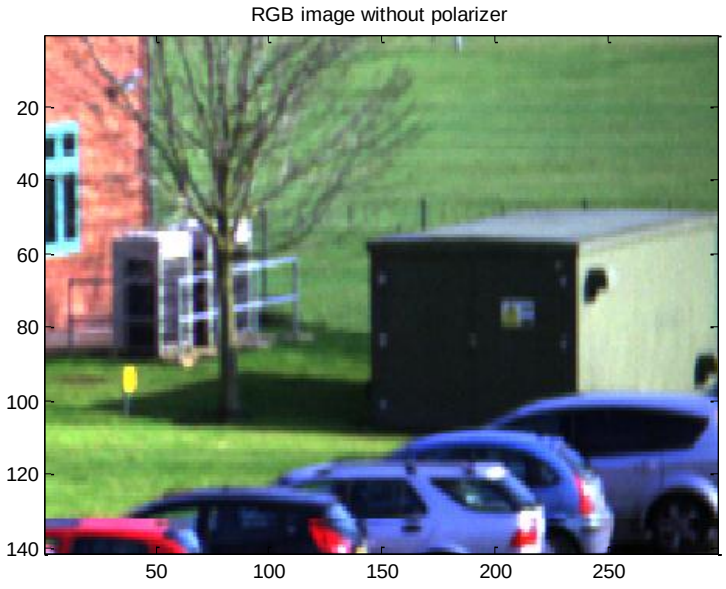
RGB image without polarizer
20
40
60
80
100
120
140
50
100
150
200
250

(a)

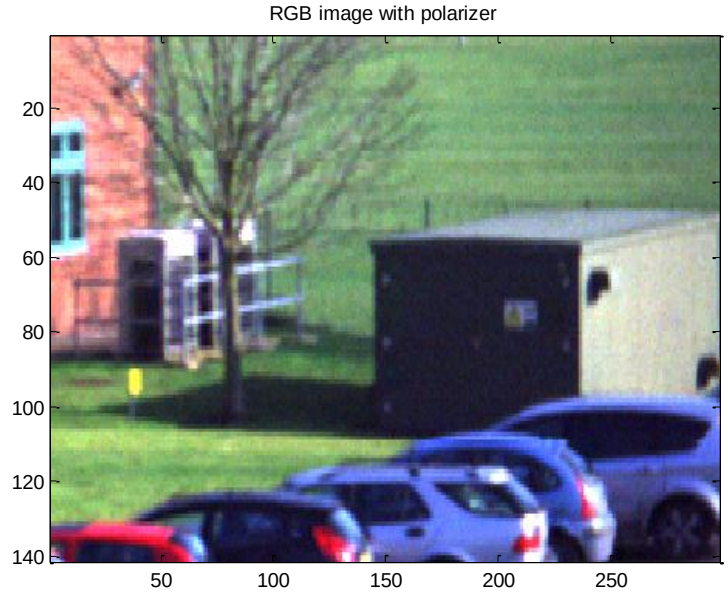
RGB image with polarizer
20
40
60
80
100
120
140
50
100
150
200
250

(b)

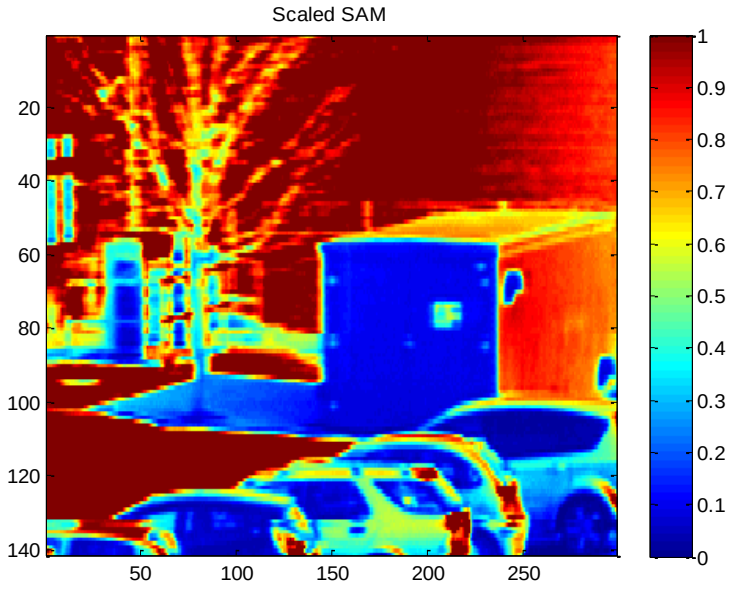

(c)

Figure 8-10 Shows the RGB image (a) without polarizer (I_{NP}), (b) with polarizer (I_P) and (c) the false colour map of the scaled_SAM result for the bunker outdoor scene. Note that the near side of the bunker and the cars have been identified as shadows correctly.

8.5 Spectro-polarimetry (SP) Method Assessments

To evaluate the effectiveness of the shadow compensation using polarization technique, the QD classifier has been employed for the 4 and 10 coloured t-shirt data sets. The angle and distance metric have been deployed for assessing the spectral similarity of the shadowed pixels with respected to that under direct illumination before and after correction by the SP.

8.5.1 Indoor scene

Figure 8-11 shows the training data and the ground truth map for the 4 coloured t-shirt indoor data. It can be seen from Figure 8-12 that the classification accuracy is almost 2 times better than that using the RW method which assumes the complete scene receives E_{direct} only. The QD result after the SPT correction has achieved ~98% accuracy far better than that by the RW (48%).

Figure 8-13 shows the spectral plots of the apparent reflectance of the shadowed pixels for the 4 coloured t-shirts to compare with that before (RW) and after correction by the SP method. It is seen that the SP corrected spectra (in green curves) have improved rather remarkably and they are a close resemblance to that under direct illuminations.

The QD result after SP correction image has achieved 90% classification accuracy for the 10 coloured t-shirt indoor data as shown in Figure 8-14. The spectral plots of the apparent reflectance of the shadowed pixels for the 4 selected t-shirt targets before and after compensation are given in Figure 8-15. It is seen that the corrected spectra by SP (in green curves) have improved substantially and they are a close resemblance to that under direct illuminations.

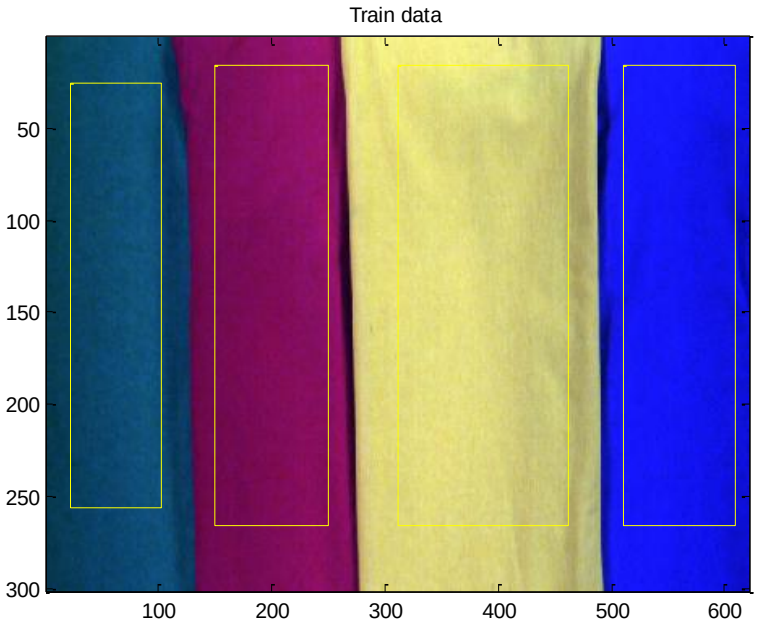

(a)

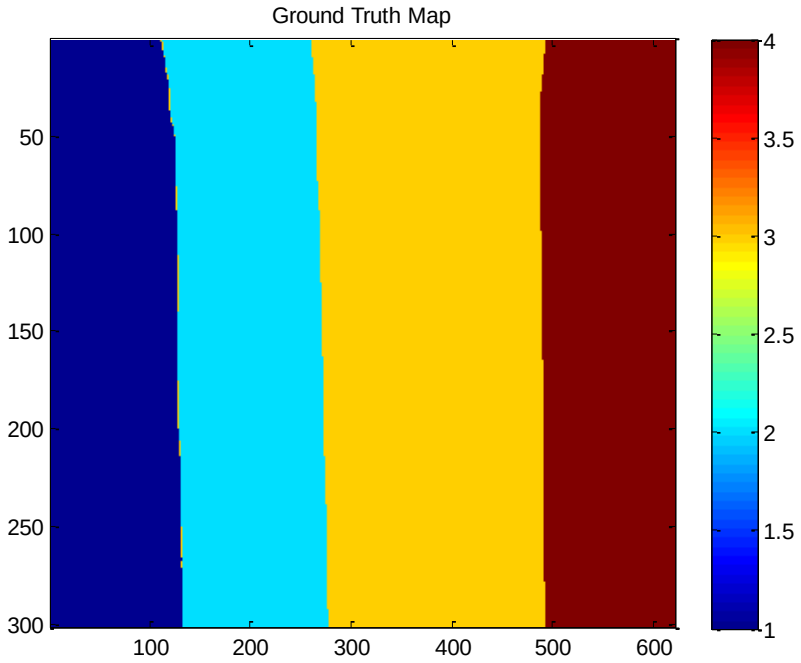

(b)

Figure 8-11 (a) Shows the RGB image of the baseline scene under direct illumination, and the yellow box depicts where the training data pixels are extracted from; (b) the ground truth target map in false colours.

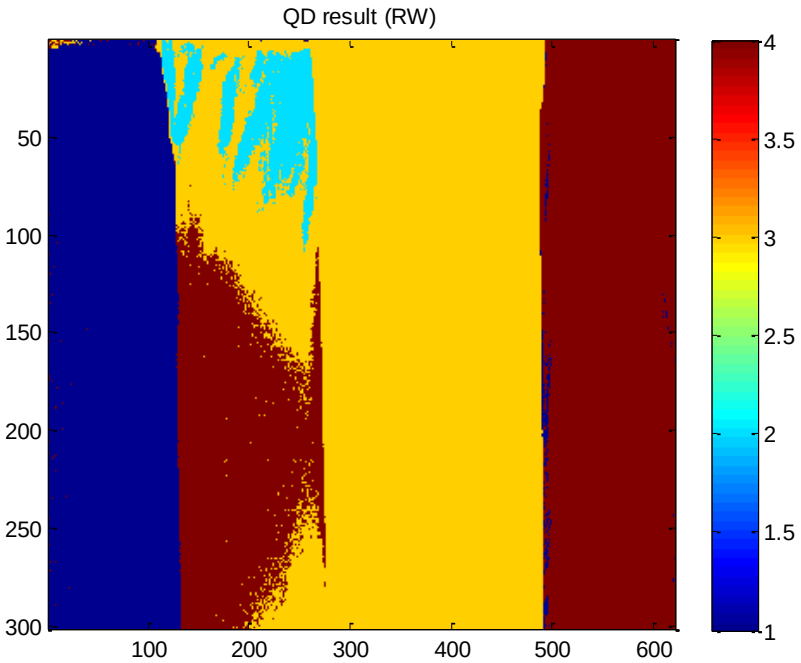

(a)

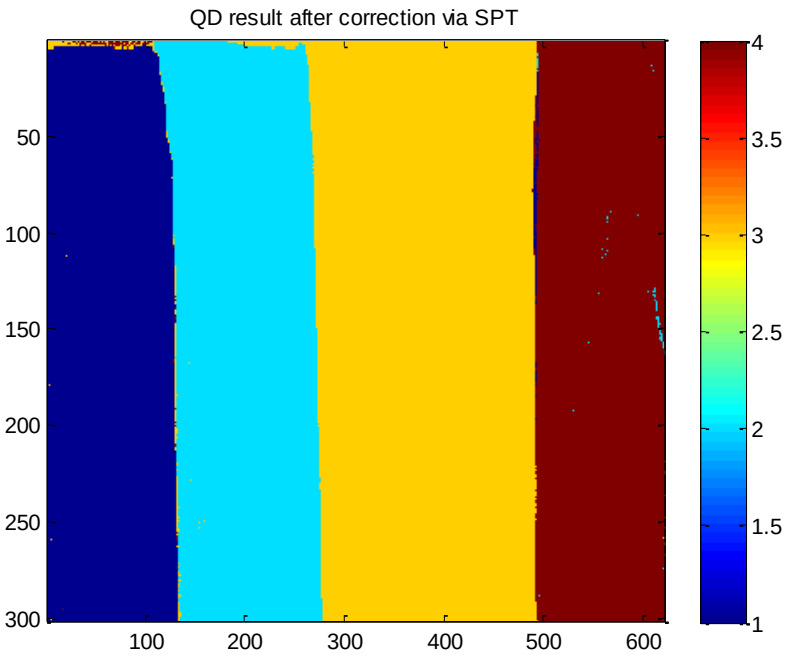

(b)

Figure 8-12 Shows the false colour map of the QD result (a) no correction by RW with accuracy 48%, (b) after correction by SP with 98% classification accuracy.

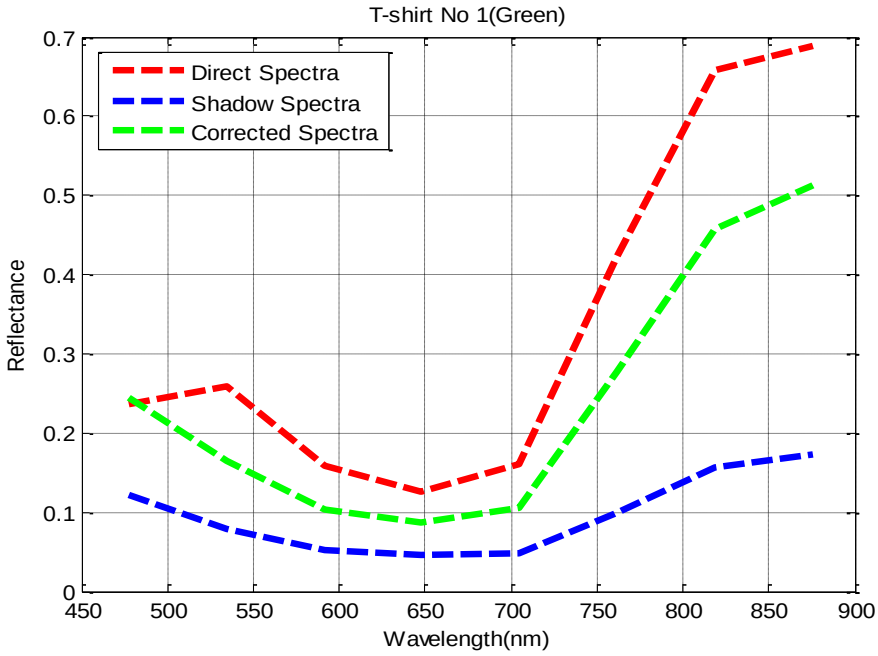

(a)

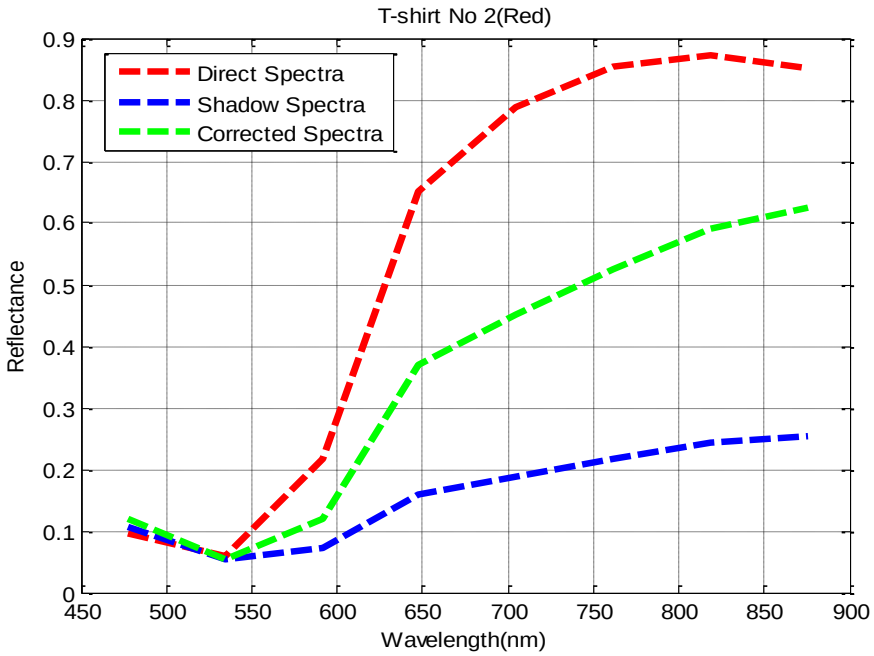
T-shirt No 2(Red)
Direct Spectra
Shadow Spectra
Corrected Spectra
Reflectance
Wavelength(nm)
0
0.1
0.2
0.3
0.4
0.5
0.6
0.7
0.8
0.9
450
500
550
600
650
700
750
800
850
900

(b)

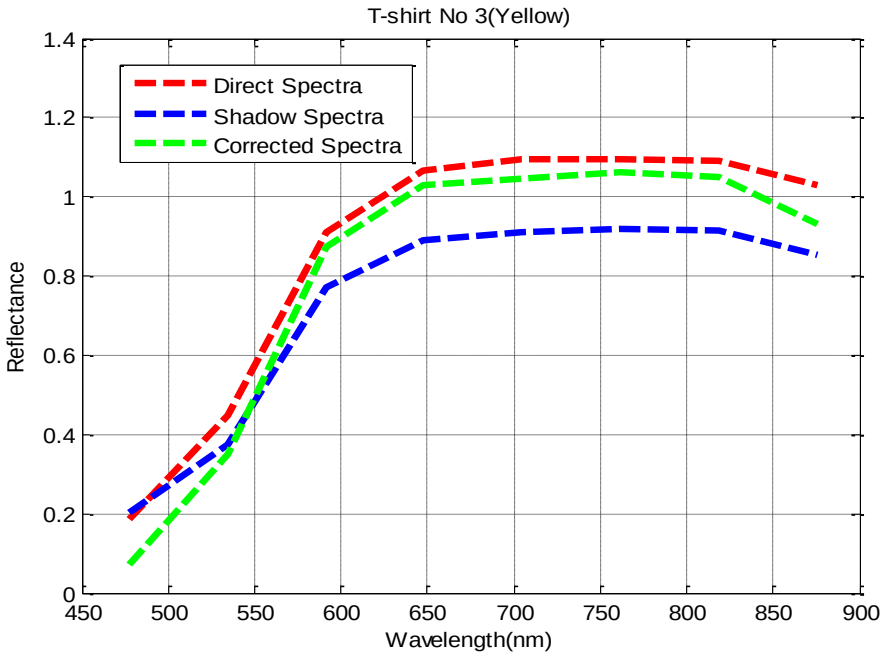
T-shirt No 3(Yellow)
Direct Spectra
Shadow Spectra
Corrected Spectra
Reflectance
Wavelength(nm)
0
0.2
0.4
0.6
0.8
1
1.2
1.4
450
500
550
600
650
700
750
800
850
900

(c)

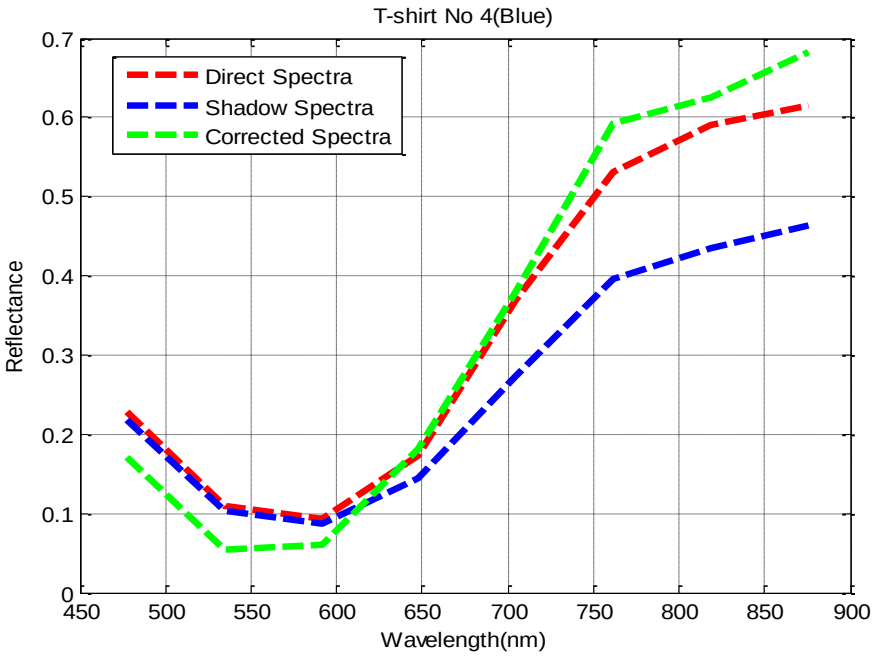

(d)

Figure 8-13 Shows the spectral plot of (a) Green t-shirt 1 (b) Red t-shirt 2 (c) Yellow t-shirt 3 and (d) Blue t-shirt 4 for the pixels i) no shadow compensation (RW in blue), ii) after SPT correction (in green) and iii) direction comparison with that under direct illumination (in red).

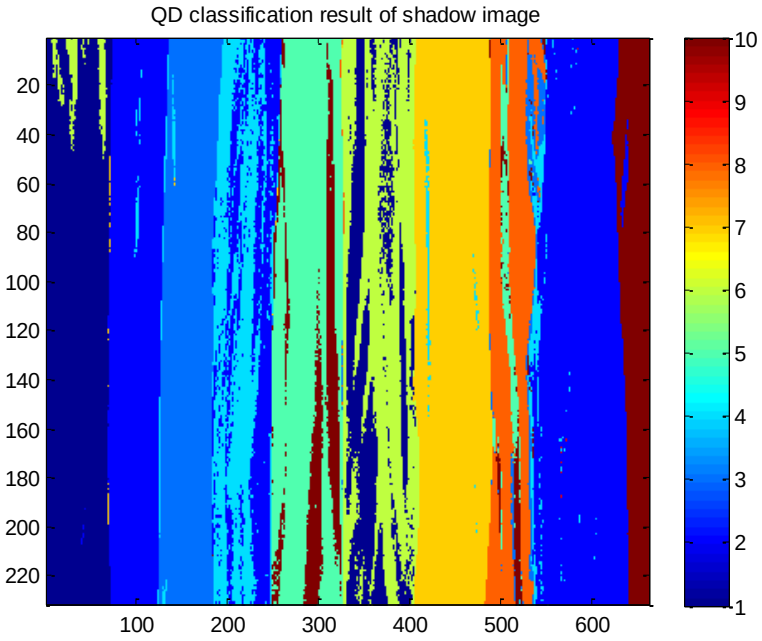

(a)

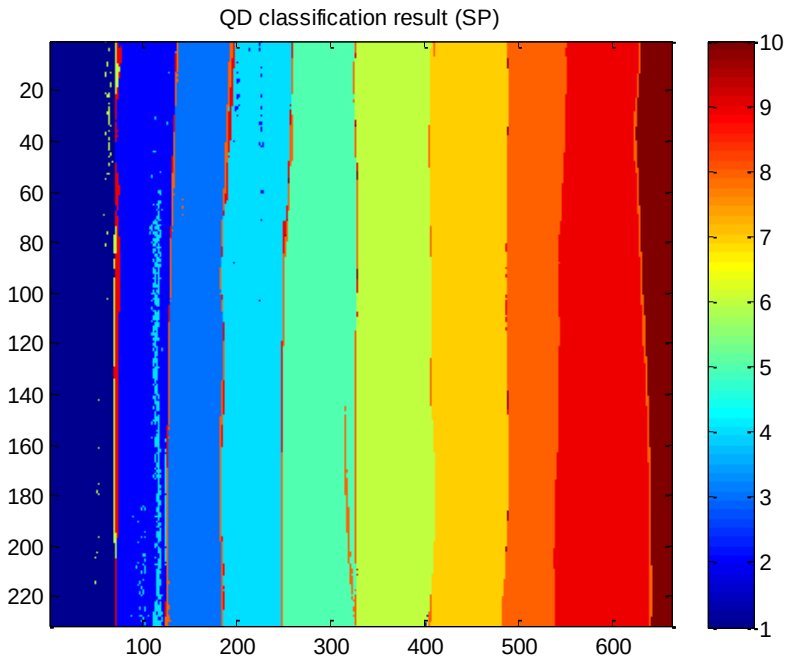

(b)

Figure 8-14 Shows the false colour QD results (a) before correction by RW with accuracy of 57%, (b) after correction by SP with 90% accuracy.

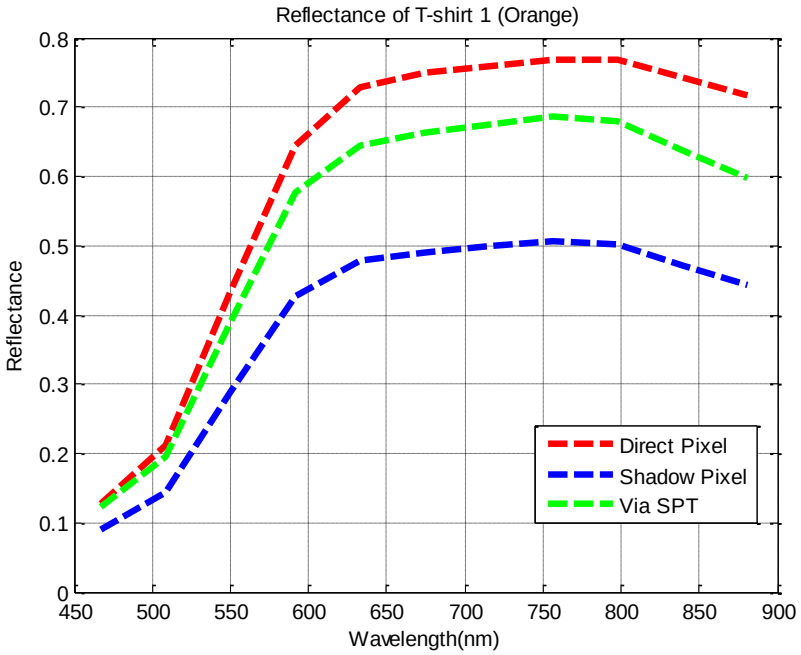

(a)

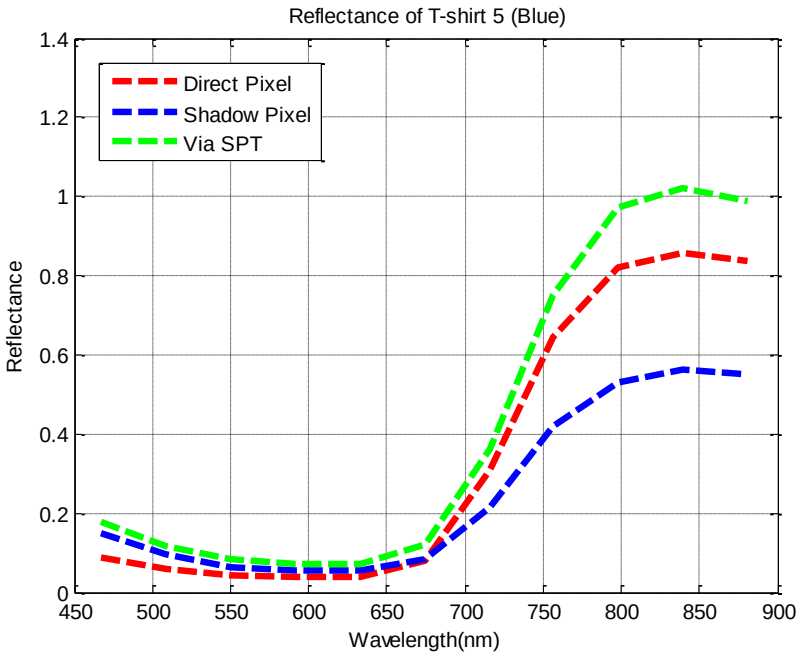
Reflectance of T-shirt 5 (Blue)
Direct Pixel
Shadow Pixel
Via SPT
Reflectance
Wavelength(nm)
1.4
1.2
1
0.8
0.6
0.4
0.2
0
450
500
550
600
650
700
750
800
850
900

(b)

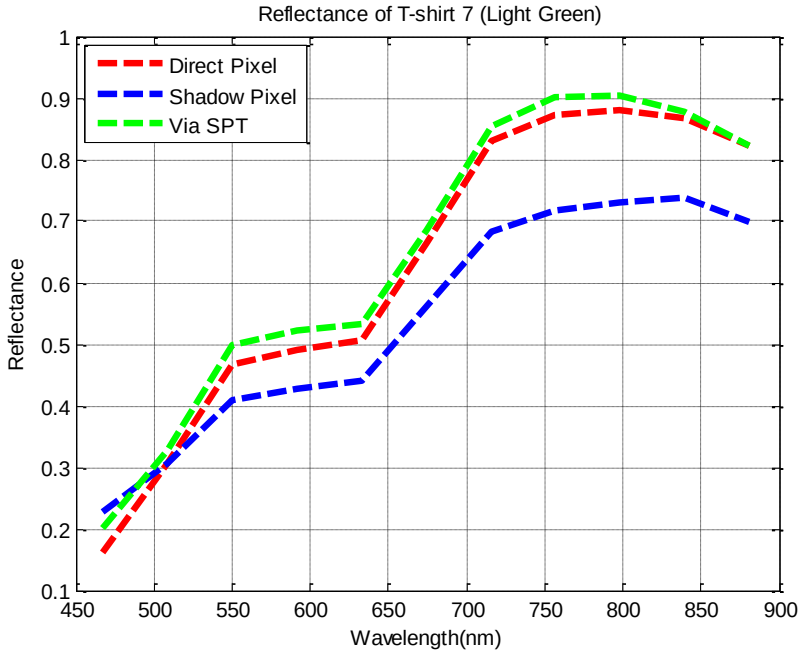
Reflectance of T-shirt 7 (Light Green)
Direct Pixel
Shadow Pixel
Via SPT
Reflectance
Wavelength(nm)
1
0.9
0.8
0.7
0.6
0.5
0.4
0.3
0.2
0.1
450
500
550
600
650
700
750
800
850
900

(c)

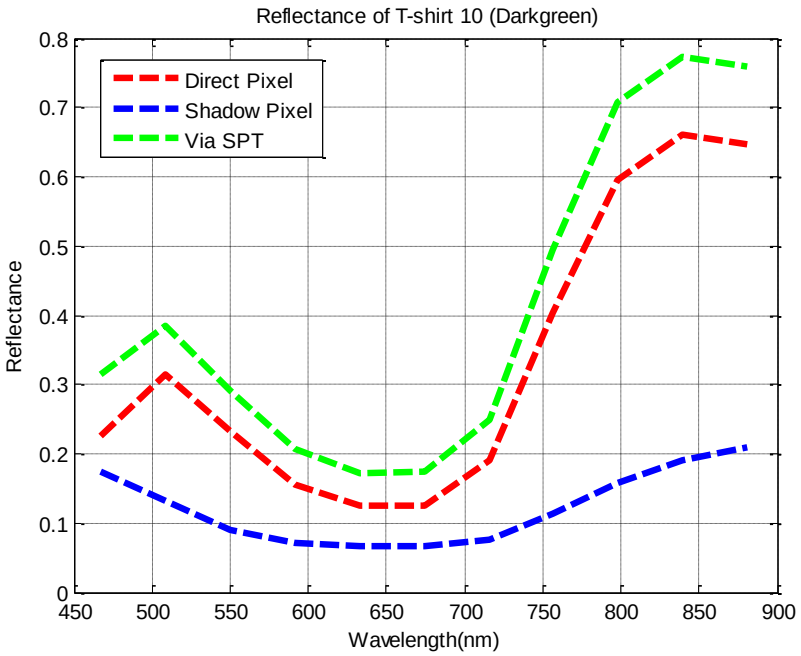

(d)

Figure 8-15 Shows the spectral plot of (a) t-shirt 1 (Orange), (b) t-shirt 5 (Blue), (c) t-shirt 7 (Light Green) and (d) t-shirt 10 (Dark Green) after i) no shadow compensation by RW (in blue), ii) after SPT correction (in green) and iii) comparison with that under direct illuminations.

8.5.2 Outdoor scene

The result of the shadow correction for the lawn scene is shown in Figure 8-16 and it is seen that the RGB images have shown remarkable improvements after the shadow compensation, with substantial enhancements on the spectral integrity as shown in Figure 8-16 (c). Table 8-1 and Table 8-2 show the spectral similarities of the shadow pixels before and after correction by SP technique for the lawn and bunker data sets. From the table, the angle and distance measure after correction have shown better similarities compared to before the correction. It is seen that the SP technique has shown to be an effective shadow compensation technique which can compensate shadows without the need of choosing threshold parameters.

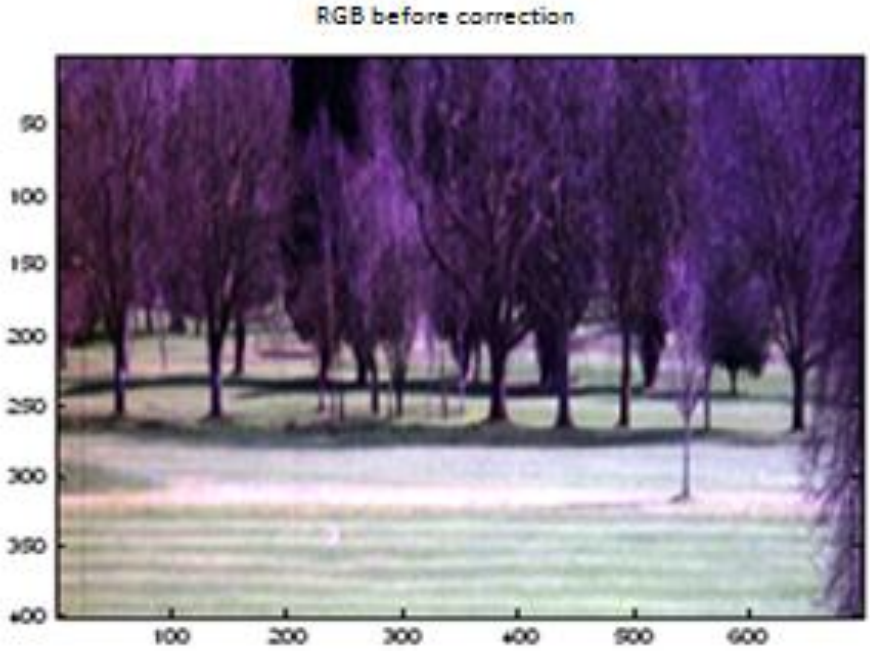
RGB before correction
50
100
150
200
250
300
350
400
100
200
300
400
500
600

(a)

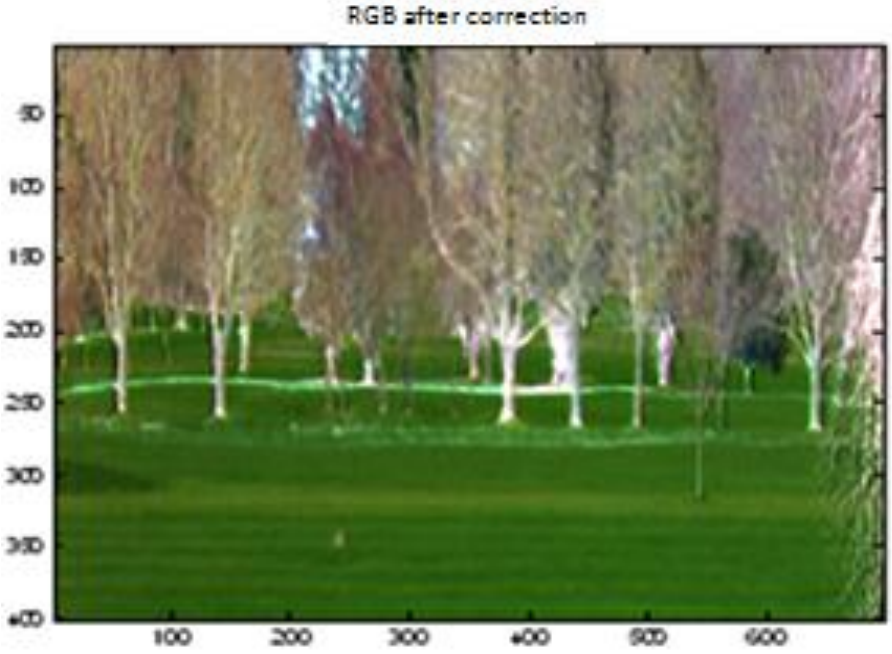
RGB after correction
50
100
150
200
250
300
350
400
100
200
300
400
500
600

(b)

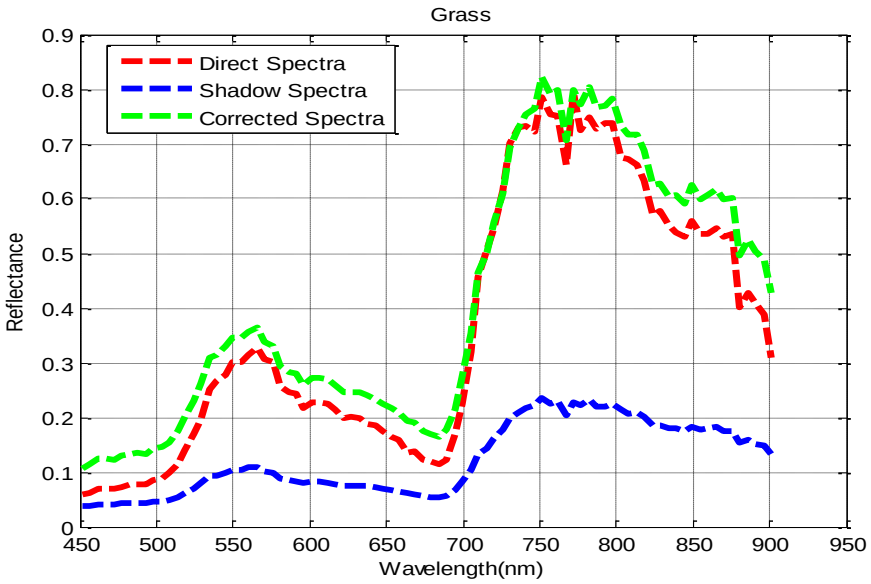

(c)

Figure 8-16 shows the the RGB images (a) before correction (I_{NP}), (b) the RGB after correction by SPT and (c) the spectral plot of the shadow pixels of the lawn before (in blue) and after correction by SPT (in green) with respect to that under direct illumination (in red).

Table 8-1 shows the spectra similarity of the shadow targets before and after correction by SP technique with respected to that under direct illumination for the lawn data set.

Field Data	Before correction	Spectro-polarimetry technique
Angle Similarities	0.1°	0.08°
Distance Similarities	0.3	0.05

Table 8-2 shows the spectra similarity of the shadow targets before and after correction by SP technique with respected to that under direct illumination for the bunker data set.

Bunker Data	Before correction	Spectro-polarimetry technique
Angle Similarities	0.16°	0.13°
Distance Similarities	0.27	0.09

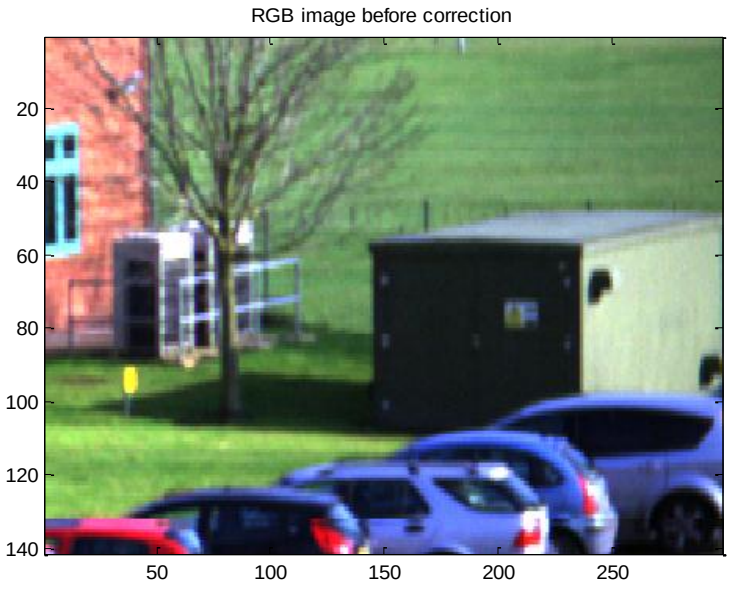

(a)

(b)

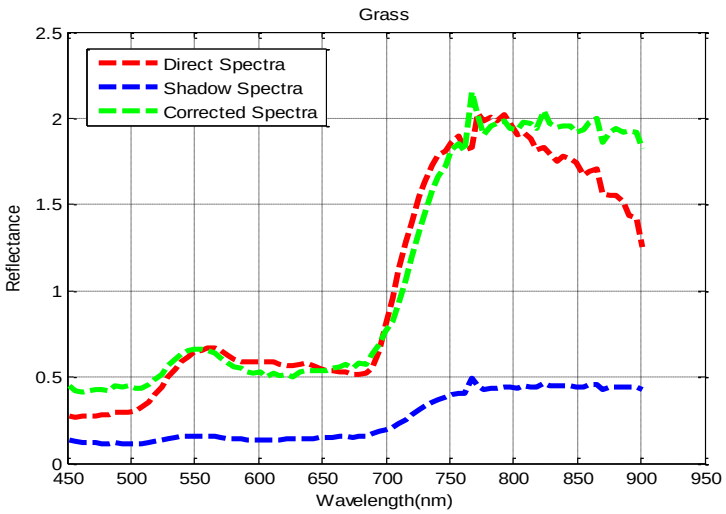

(c)

Figure 8-17 shows the (a) the RGB image before correction (I_{NP}), (b) the RGB image after correction by SP technique and (c) the spectral plot of the shadow target before (in blue) and after correction by SPT (green) with respect to that under direct illumination (in red) for the bunker outdoor data. The edge of shadow shape in (b) is seen to have a mixed pixel problem due to the bad pixels resolution of the camera.

8.6 Conclusion

In this chapter a new method using spectro-polarimetry has been presented for illumination invariance and shadow correction on hyperspectral imageries. The spectro-polarimetry technique (SP) is capable to segment the shadow and non-shadow regions based on the degree of polarization using simple Spectral Angle Mapper (SAM) processing. The present result has shown that pixels under direct and diffuse irradiance can be estimated using the polarization technique.

The overall classification result for using different shadow compensation methods is summarised in Table 8-3 :

(a) The SP technique achieves better classification accuracy with about a factor of two better than that by the RW as it is evidenced by both the 4 and 10 coloured t-shirts data sets.

(c) The proposed SP method has improved the angle match ~25% and 18% better than that of the RW method for the lawn and bunker shadows respectively, with respected to that under direct illuminations.

This SP technique method has overcome most of the disadvantages in DIC and LR method such as:

(a) There is no need to establish shadow masks using elaborate threshold method in the SPT.

(b) The SPT does not require the standard panel to model the diffuse irradiance.

(c) The SPT compensates shadows according to the depth of the shadow: larger value of correction will be given for the deeper shadow.

Table 8-3 The overall result of classification accuracy.

	Raw	RW	DIC	LR	SPT
10 t-shirt data	38%	68%	70%	75%	90%
5 t-shirt data	31%	43%	58%	97%	-
4 t-shirt data	-	48%	73%	86%	98%

9 CONCLUSIONS AND FUTURE WORK

The main objective of this research is to establish a method for the compensation of illumination artefacts such as shadows in order to achieve spectral constancy so to improve object recognitions. This chapter summarises all the achievements during the course of this PhD programme entitled 'Illumination invariance and shadow compensation on hyperspectral images'.

Three different types of algorithms have been developed for shadow compensation and illumination invariance on hyperspectral images in this work. Indoor and outdoor data has been selected as test data to assess the algorithm performance. Three types of performance metric, Quadratic classifier (QD), spectral angle and distance metrics have been used to evaluate algorithms achievements. All algorithms are written in MATLAB to allow future work modifications.

9.1 Diffuse Irradiance Compensation Method (DIC)

It is found from this study that the classification accuracy after converting the data into 'apparent' reflectance denoted by RW, is about a factor of 2 better than that using the raw DN data which includes the sensor characteristics and illumination artefacts. The study also demonstrates that spectral normalisation for 'flattening' illumination artefacts will result in a reduction of classification accuracy by about 30% compared to RW data.

This work has also shown that the shadow compensation can be achieved if the diffuse irradiance can be estimated from the scene. The Diffuse Irradiance Compensation (DIC) method has been proposed for reducing shadow effect. It is found that:

(a) The diffused irradiance compensation (DIC) enhances the target classification accuracy over the RW method by about ~2% to 15% for the data sets investigated in this study.

The DIC method requires the standard panel to be placed in the scene for sampling the diffuse and direct irradiance. In real scenarios this method may be hard to implement. Hyperspectral images may contain various degrees of shadows and the DIC method compensates all shadows by the same amount without taking the softness of the shadows into account. The other limitations in DIC method is the establishment of the shadow mask which requires hard thresholds to segment the scene into shadow and non-shadow regions. The optimum threshold value is scene dependent and the methodology for finding this value in a principled way is still lacking.

9.2 Linear Regression Method (LR)

The DIC method has exhibited some improvements for shadow compensation but it is difficult to implement in practise. Alternatively, a Linear Regression (LR) method which transfers statistics from the non-shadow region into the shadow region has been proposed for illumination invariant of hyperspectral processing.

The achievements and limitations of LR method have been found as follows:

(a) The LR treated data has achieved classification accuracy of ~7% to 54% better than that of the RW treatment for the data sets investigated in this study.

(b) The LR method is found to be ~5% to 39% better than that of the DIC method over the data sets investigated in this work.

(c) The performance of the LR method is strongly dependent on the distributions of the target and backgrounds in the shadow and non-shadow regions.

Although the LR method has exhibit some improvements over the RW and DIC methods, this methodology is prone to outliers and the distributions of targets in the shadow and non-shadow regions. This method is optimum only if the abundance of the objects is equally distributed in both the shadow and non-shadow regions.

9.3 Spectro-polarimetry Technique (SP)

A new method which is based on spectra-polarimetry has been proposed for shadow compensation in HSI imagery. The principle underlying this work makes use of the fact that the reflections from objects under diffuse irradiance are relatively more unpolarised than that under direct illumination. A Spectral Angle Mapper (SAM) has been employed to assess the extent of the direct and diffuse irradiances based on two images taken with and without polarizer for the same scene. This SAM value is then re-scaled for the shadow compensation. Although the polarization technique has been used in the conventional broad band image processing for shadow compensation, this technique is believed to be the first study for spectral invariance in hyperspectral image processing.

(a) The SP technique achieves better classification accuracy with about a factor of two better than that by the RW as it is evidenced by both the 4 and 10 coloured t-shirts data sets.

(b) The proposed SP method has improved the angle match ~25% and 18% better than that of the RW method for the lawn and bunker shadows respectively, with respect to that under direct illuminations.

(e) This SPT method has overcome most of the disadvantages in DIC and LR method such as:

1. There is no need to establish shadow masks using elaborate threshold method in the SP method.

2. The SP technique does not require the standard panel to model the diffuse irradiance.

3. The SP technique compensates shadows according to the depth of the shadow: larger value of correction will be given for the deeper shadow.

The only drawback of this method is that it will require two sets of the same scene to be acquired, with and without polarization. Hence this methodology may be more difficult to be applied to real time applications.

9.4 Future Work

Although the SP technique has shown remarkably good results for shadow compensation, more future work is needed especially for the design of the push broom type hyperspectral camera as the scanning mirror will impose some polarizations to the reflected beam. The design of a hyperspectral polarization sensitive imaging system may help to overcome the limitation of the presently SP method that requires two sets of the same scene to be acquired, with and without polarization.

Other than that, one should attempt to apply the SP technique for the SWIR region. The polarization within the visible to near infrared region is dominated by the reflection properties of the surface. However, the polarization in the short wave infrared region is complicated by the emission properties. The different polarisations in these two regions may help to improve the effectiveness of the SP technique in the future.

Polarization on shadow surface also would be changed during the different time in the day. This technique can also be improved by experimenting it at different time during the same day to see the changes on the polarization properties from the reflectance of target under shadow. Also, the degree of polarisation will be sensitive to sun-target-sensor geometry as a generalisation of the time of day. Furthermore, the shadow compensation algorithm derived in this work has been a non-principled method and a more rigorous physics based approach should be the next step of work.

REFERENCES

1. *Use of airborne hyperspectral imagery to map soil properties in tilled agriculture fields.* **Hively W. D., McCarty G. W., Reeves III J. B., Lang M. W., Oesterling R. A. and Delwiche S. R.** s.l. : Hindawi Publsiing Corporation, 2011, Applied and Environmental Soil Science, Vol. 2011, pp. 1-13.

2. *A review of hyperspectral remote sensing and its application in vegetation and water resource studies.* **Govender, M., Chatty, K. and Bulcock, H.** 2, South Africa : South Africa Water Research Commision, 2007, Water SA, Vol. 33, pp. 145-152.

3. *Airborne infrared hyperspectral imager for intelligence, surveillance and reconnaissance applications.* **Puckrin., E., Turcotte, C. S., Gagnon, M., Bastedo, J., Farley, V. and Chamberland, M.** Baltimore, Maryland : SPIE, 2012. Vol. 8360.

4. *Use of hyperspectral remote sensing for crop stress detection : Ground Based Studies.* **Ray, S. S., Singh, J. P. and Panigrahy, S.** 8, 2010, International Archives of the Photogrammetry, Remote Sensing and Spatial Information Science, Vol. XXXVIII, pp. 562-567.

5. *Hyperspectral remote sensing technology and applications in China.* **Tong, Q., Zhang, B., and Zheng, L.** Frascati, Italy : European Space Agency (ESA), 2004. Proc. of the 2nd CHRIS/Proba Workshop. Vols. SP-578, pp. 1-10.

6. *Multispectral and hyperspectral imaging: Applications for medical and surgical diagnostic.* **Freeman, J., Downs, F., Marcucci, L., Lewis, E. N., Blume, B. and Rish, J.** Chicago, USA : Institute of Electrical and Electronics Engineers (IEEE), 1997. Engineering in Medicine and Bi Proceedings of the 19th Annual International Conference of the IEEE IEEE Engineering in Medicine and Biology Society. Vol. 2, pp. 700 - 701.

7. *Hyperspectral imaging applied to medical diagnosis and food safety.* **Carrasco, O., Gomez, R. B, Chainani, A. and Roper, W. E.** Orlando, FL :

SPIE, 2003. Proc. SPIE 5097, Geo-Spatial and Temporal Image and Data Exploitation III. Vol. 5097, pp. 215-221.

8. *Hyperspectral algorithm development for military applications: A multiple fusion approach.* **Yuen, P. W. T. and Bishop, G.** Edinburgh : Electro Magnetic remote Sensing (EMRS) Defence Technoly Centre (DTC), 2006. 3rd EMRS DTC Technical Conference. Vol. B20, pp. B20-1-6.

9. *Spectral imaging for remote sensing.* **Shaw, G. and Burke, H.** 1, 2003, Lincoln Laboratory Journal, Vol. 14, pp. 3-28.

10. **Richards, J.A. and Jia, X.** *Remote sensing digital image analysis: An introduction.* Berlin, Heidelberg, Germany : Springer, 2006.

11. *Hyperspectral image processing for automatic target detection applications.* **Manolakis, D., Marden, D., and Shaw, G. A.** Lincoln Laboratory Journal : MIT, 2003, Vol. 14, pp. 79-116 .

12. *Hyperspectral multiple approach fusion for the long range detection of low observable objects:MUF2.* **Yuen, P. W. T. and Bishop, G.** Europe : SPIE, 2006. Proceedings of the SPIE: Electro-Optical Remote Sensing II. Vol. 6396.

13. **Alhberg, J., Chevalier, T., Andersson, P. and Klasen, L.** *Target detection in multispectral imagery.* Sweeden : Swedish Defence Research Agency, 2004.

14. *Adaptive multiple-band CFAR detection of an optical pattern with unknown spectral distribution.* **Reed, I. S. and Yu, X.** October 1990, IEEE Transaction on Acoustic. Speech. and Signal Processing, pp. 1760-1770.

15. *Algorithms for the detection of sub-pixels targets in multispectral imagery.* **Ashton, E. A. and Schaum, A.** 7, s.l. : American Society for Photogrammetry and Remote Sensing (ASPRS), July 1998, Photogrammetic Engineering & Remote Sensing, Vol. 64, pp. 723-731.

16. **Ahlberg, J. and Renhorn, I.** *Multi-and hyperspectral target and anomaly detection.* Linkoping : FOI Swedish Defence Research Agency, 2004.

17. **Stein, D. W. J., Beaven, S. G., Hoff, L. E., Winter, E. M., Schaum, A. P. and Stocker, A. D.** Anomaly detection from hyperspectral imagery. *IEEE Signal Processing Magazine.* January 2002, Vol. 19, 1, pp. 58-69.

18. *Adaptive feature extraction techniques for subpixel target detections in hyperspectral remote sensing.* **Yuen P. W. T. and Bishop, G.** London, UK. : SPIE, 2004. Proc. of SPIE Military remote sensing. Vol. 5613.

19. *The effectiveness and limitations of geometric and statistical spectral unmixing techniques for subpixel target detection in hyperspectral remote sensing.* **Yuen P. W. T., Blagg. A. and Bishop, G.** Bruges, Belgium : SPIE, 2005. Proc. of SPIE: Electro-Optical Remote Sensing. Vol. 5988.

20. **West, J. E. .** *Matched filter stocastic background characterization for hyperspectral target detection.* s.l. : Rochester Institute of Technology, 2005.

21. **Chang, C-I.** *Hyperspectral Imaging: Techniques for Spectral Detection and Classification.* New York, USA. : Kluwer Academic/Plenum Publisher, 2003.

22. **Webb, A.** *Statistical pattern recognition.* United Kingdom : A Hodder Arnold Publication. , 1999.

23. **Duda, R. O., Hart, P. E., Stork, D. G.** *Pattern Classification 2nd Edition.* New York : John Wiley & Sons, Inc, 2001.

24. **Seyrafi, K. and Hovanessian, S. A.** *Introduction to electro-optic imaging and tracking system.* Norwood, MA 0206, USA : Artech House, Inc. , 1993.

25. **Driggers, R.G., Cox, P. and Edwards, T.** *Introduction to Infrared and Electro-Optical Systems.* Norwood, MA, USA : Artech Hous, 1999.

26. *Derivation of Scaled Surface Reflectances from AVIRIS Data.* **Gao, B., Heidebrecht, K. B. and Goetz, A. F. H.** s.l. : Elsevier, 1993, Remote Sens. Environ, Vol. 44, pp. 165-178.

27. Atmospehric Correction. *Sarracenia.* [Online] [Cited: 16 August 2012.] http://www.sarracenia.com/astronomy/remotesensing/physics060.html .

28. **Yuen P., Ibrahim I., Hong K., Chen T., Tsitiridis A., Kam F., Jackman J., James D., Richardson M.** Classification enhancements in hyperspectral remote sensing using atmospheric correction preprocessing technique. *The Technical Defence S&T Bulletin.* 2009, Vol. 2, 2, pp. 91-99.

29. *Polarization-and Specular-Reflection-Based, Non-contact Latent Fingerprint Imaging and Lifting.* **Lin, S., Yemelyanov, K.M., Pugh, E. N. J. and Engheta, N.** 9, September 2006, Journal of Optical Society of America A, Vol. 23, pp. 2137-2153.

30. **Freeman, M. H.** *Optics.* London : Butterworth, 1990.

31. **Zissis, G. J.** *The infrared and electro-optic systems handbook. Volume 1: Source of Radiation.* Michigan, USA : IR Information Analysis Centre and SPIE Optical Engineering Press, 1993.

32. **Salekdeh, A. Y.** *Mutispectral and hyperspectral images invariant to illumination.* Canada : Simon Fraser University Library, 2009.

33. **Randall, S.M.** Introduction to hyperspectral imaging. *microimages.* [Online] MicroImages, Inc. [Cited: 8 August 2012.] http://www.microimages.com/documentation/Tutorials/hyprspec.pdf.

34. *Effects of empirical versus model-based reflectance calibrated on automated analysis imaging spectrometer data: A case study from the Drum Mountains, Utah.* **Dwyer, J. L., Kruse, F. A. and Lelkoff, A. B.** 10, s.l. : American Society for Photogrammetry and Remote Sensing (ASPRS), October 1995, Photogrammetic Engineering & Remote Sensing, Vol. 61, pp. 1247-1254.

35. *A comparison between six model-based methods to retrieve surface reflectance and water vapor content from hyperspectral data: A case study using synthethic AVIRIS data.* **Ben-Dor, E., Kindel, B. C. and Patkin, K.**

Dehradun, India : The Optical Society of India, 2005. International Conference on Optics & Optoelectronics (ICOL).

36. *A review of atmospheric correction techniques for hyperpsectral remote sensing of land surfaces and ocean color.* **Gao, B., Davis, C. O. and Goetz, A. F. H.** Washington, DC : IEEE, 2006. Conference on Geoscience and Remote Sensing Symposium (GARSS).

37. *The relationship between size of spatial substes of GER 63 channel scanner data and the quality of the internal average relative reflectance (IARR) atmospheric correction.* **Ben-dor, E. and Kruse, F. A.** 3, United Kingdom : Taylor & Francis, 1994, International Journal Remote Sensing, Vol. 15, pp. 683-690.

38. *Use of airborne imaging spectrometer data to map minerals associated with hydrothermally altered rocks in the Northern Grapevine Mountains, Nevada and California.* **Kruse, F. A.** New York, USA. : Elsivier, 1985, Remote Sensing of Environment , pp. 2431-51.

39. Computing radiances, reflectance and albedo from DN's . *Yale University.* [Online] [Cited: 10 September 2012.] http://www.yale.edu/ceo/Documentation/ComputingReflectanceFromDN.pdf.

40. *Automatic flat field algorithm for hyperspectral image calibration.* **Zhang, X., Zhang, B., Geng, X., Tong, Q. and Zheng, L.** Wuhan, China : SPIE, 2003. Symposium on Multispectral Image Processing and Pattern Recognition. Vol. 5286, pp. 636-639.

41. *Evaluations of airborne visible/infrared imaging spectrometer data of the Mountain Pass, California Carbomatite Complex.* **Crowley, J., Rowan, L. and Podwysocki, M.** Jet Propulsion Lab., California Inst. of Tech : Proceedings of the Airborne Visible/Infrared Imaging Spectro, 2006.

42. *Calibration of airborne imaging spectrometer data to percent reflectance using field spectral measurements.* **Roberts, D.A., Yamaguchi, Y., and Lyon,**

R.J.P. Ann Arbor, Michigan : Environmental Research Institute of Michigan, Canada Centre for Remote Sensing, 1985. Proceedings Nineteenth International Symposium on Remote Sensing of Environment. pp. 679-688.

43. *Airborne Imaging Spectrometer-2: Radiometry and a comparison of methods for the recovery of ground reflectance.* **Conel, J.E., R.O. Green, G.Vane, C.J. Brueege and R.E. Alley.** Pasadena, California : Jet Propulsion Laboratory, 1987. Proceedings Airborne Imaging Spectrometer Data Analysis Workshop. Vol. 21987, pp. 18-47.

44. *Mineral mapping at Cuperite, Nevada, with a 63 channel imaging spectrometer.* **Kruse, F. A., Kieren-Young, K. S., and Boardman, J. W.** 56, Maryland, USA : The American Society for Photogrammetry and Remote Sensing (ASPRS) , 1990, Photogrammetric Engineering & Remote Sensing, pp. 83-92.

45. **Richter, R. and Muller, A.** *Atmospheric/Topographic Correction for Satellite Imagery (ATCOR 2/3 User Guide).* German : German Aerospace Center, 2005. pp. 3137-3148. Vol. 6.1.

46. *Comparison of FLAASH versus Empirical Line Approach for atmospheric correction of OMIS-II imagery.* **Zhang, X., Yang, H. and Shuai, T.** Rio de Janeiro, Brazil : IEEE, 2009. Asian Association on remote Sensing on IEEE Conference on Agriculture/ Soil/Others.

47. *The high accuracy atmospheric correction for hyperpsectral data (HATCH) model.* **Qu, Z.** 6, Colorado, USA : IEEE, June 2003, IEEE Transactions on Geoscience and Remote Sensing, Vol. 41, pp. 1223-1231.

48. *Using ground spectral irradiance for model correction of AVIRIS data.* **Goetz, A. F. H., Heidebrecht, K. B., Kindel, B. and Boardman, J. W.** Pasadena, CA. : Jet Propulsion Laboratory, 1998.

49. **Schowengerdt, R. A.** *Techniques for image processing and classification in remote sensing.* London : Academis Press, 1983.

50. *Atmospheric correction of PROBA/CHRIS data in an urban environment.* **Zhou, J., Wang, J., Li, J. and Hu, D.** 39, United Kingdom : Taylor and Francis, 2011, " International Journal of Remote Sensing, Vol. 32, pp. 2591-2604.

51. *Column atmospheric water vapour and vegetation liquid water retrievals from airborne imaging spectrometer data.* **Gao, B. and Goetz, A. F. H.** New York, Washington DC. : American Geophysical Union, 1990, Journal of Geophysical Research, Vol. 95, pp. 3549-3564.

52. **Campbell, J. B. and Wynne, R. H.** *Introduction to Remote Sensing Fifth Edition.* New York, USA. : The Guilford Press, 2011.

53. *Coniferous forest classificationa and inventory using Landsat and digital terrain data.* **Franklin, J., Logan, T. L., Woodcock, C. E. and Strahler, A. H.** 1, January 1986, IEEE Transaction on Geoscience and Remote Sensing, Vol. 21, pp. 139-149.

54. *Scene shadow effects on multispectral response.* **Ranson, K.J. and Daughtry, S. T.** 4, s.l. : IEEE, 1987, IEEE Transaction on Geoscience and Remote Sensing, Vol. 25, pp. 502-509.

55. *De-shadowing of satellite/airborne imagery.* **Richter, R. and Muller, A.** 15, United Kingdom : Taylor and Francis, 2005, International Journal of Remote Sensing, Vol. 26, pp. 3137-3148.

56. *An algorithm for de-shadowing spectral imagery.* **Adler-Golden, S. M., Matthew, M. W., Anderson, G. P., Felde, G. W. and Gardner, J. A.** Seattle, WA : SPIE, 2002, Proc. of SPIE on Imaging Spectrometry VIII, Vol. 4816, pp. 203-210.

57. *The dangers of underestimating the importance of data adjustments in band ratioing.* **Crippen, R.E.** 4, New Jersey : Prentice Hall, 1998, International Journal of Remote Sensing, Vol. 9, pp. 767-776.

58. *Use of band ratioing for building illumination independent texture classification systems.* **Muniz, R., Corrales , J. A. and Rico-Secades, M.**

Florida, USA : International Association for Pattern Recognition (IAPR), 2008. 9th International Conference on Pattern Recognition.

59. *A band ratio approach for classification in shaded area.* **Kao, H. and Ren, H.** Beijing, China : Asian Association on Remote Sensing (AARS), 2009. 30th Asian Conference on Remote Sensing. Vol. 2, pp. 658-662.

60. *Development of vegetation index using radiant spectra normalized by their arithmetic mean.* **Ono, A., Kajiwara, K., Honda, Y. and Ono, A.** Japan : Nihon-Rimōto-Senshingu-Gakkai, 2006. Proceedings of the Conference of the Remote Sensing Society of Japan. Vol. 40.

61. *Colour constancy form Hyper-spectral data.* **Gevers, T., Stokman, H.M.G and Van de Weijer, J.** Bristol, UK. : The British Machine Vision Association and Society for Pattern Recognition, 2000. Proceedings of British Machine and Vision Conference (BMVC).

62. *Hyperspectral video for illumination-invariant tracking.* **Banerjee, A., Burlina, P. and Broadwater, J.** Grenoble : IEEE, 2009. Hyperspectral Image and Signal Processing: Evolution in Remote Sensing, 2009. WHISPERS '09. First Workshop on.

63. *A novel method for illumination suppression in hyperspectral images.* **Ashton, E. A., Wemett, B.D., Leathers, R. A. and Downes, T. V.** Orlando, FL : SPIE, 2008. Proc. SPIE 6966, Algorithms and Technologies for Multispectral, Hyperspectral, and Ultraspectral Imagery XIV. Vol. 6966, pp. 69660C-69660C-8 .

64. *Effect of radiance-to-reflectance transformation and atmosphere removal on maximum likelihood classification accuracy of high-dimensional remote sensing data.* **Joseph, P. H. and David, A. L.** Pasadena, CA : IEEE, 1994. Proceedings of the 14th Annual International Geoscience and Remote Sensing Symposium IGARSS.

65. *Classification and Change detection using LandSat TM Data: When and how to correct atmospheric effect.* **Song, C., Woodcock, C. E., Seto, K. C., Lenney, M. P. and Macomber, S. A.** MO, USA : Elsivier, 2001, Remote Sensing of Environment Journal, Vol. 75, pp. 230-244.

66. *The atmospheric effect on the separability of field classes measured from satellites.* **Kaufman, Y. J.** MO, USA. : Elsevier, 1985, Remote Sensing of Environment, Vol. 18, pp. 21-34.

67. *An examination of spectral band ratioing to reduce topographic effect on remotely sensed data.* **Holbern, B. and Justice, C.** MO, USA : Elsivier, 1981, Remote Sensing Environment, Vol. 2, pp. 115-133.

68. *Comparison of relative radiometric normalization techniques.* **Yuan, D. and Elvidge, C.D.** MO, USA : Elsevier, 1996, ISPRS Journal of Photogrammetry and Remote Sensing, Vol. 51, pp. 117-126.

69. *A New Approach to Change Vector Analysis Using Distance and Similarity Measures.* **Carvalho Junior, O. A., Guimaraes, R. F., Gillespie, A. R., Silva, N. C. and Gomes, R. A. T.** 11, Basel, Switzerland : Multidisciplinary Digital Publishing Institute (MDPI), 2011, International Journal of Remote Sensing, Vol. 3, pp. 2473-2493.

70. **Egan, W. G.** *Photometry and polarization in remote sensing.* MO, New York : Elsevier, 1985.

71. *Using polarization to separate reflection components.* **Wolff, L.B.** San Diego, CA : Institute of Electrical and Electronics Engineers (IEEE), 1989. Proceedings of IEEE Computer Society Conference on Computer Vision and Pattern Recognition. Vol. 10, pp. 363-369.

72. *Dark target retroreflection increase.* **Egan, W. G.** Denver, CO, USA. : SPIE, 1999. Proc of SPIE: Polarization: Measurement, Analysis, and Remote Sensing II. Vol. 3754.

73. *Separation and contrast enhancements of overlapping cast shadow components using polarization.* **Lin, S., Yemelyanov, K.M., Jr, E. N. P. and Engheta, N.** 16, Washington, DC, USA : Optical Society of America, August 2006, Optics Express, Vol. 14, pp. 7099-7108.

74. *Improved hyperspectral imagery using diffuse illumination or a polarizer.* **Wellems, D. and Bowers, D.** San Diego, CA : SPIE, 2008. Proc of SPIE: Reflection, Scattering, and Diffraction from Surfaces. Vol. 7065.

75. *Ray tracing with polarization parameters.* **Wolff, L. B. and Kurlander, D. J.** 6, 1990, IEEE computer Graphics and Applications, Vol. 10, pp. 44-55.

76. *Improved diffuse reflection models for computer vision.* **Wolff, L., Nayar, S. K. and Oren, M.** 1, New York, USA : Springer, 1998, International Journal of Computer Vision, Vol. 30, pp. 55-71.

77. Raman Spectrocopy. *Holographic Imaging Spectrograph.* [Online] Kaiser Optical System, Inc. [Cited: 18 September 2012.] http://www.kosi.com/Raman_Spectroscopy/holoSpecf18.php?ss=600.

78. **Kam, F.** *Classification Technique for Hyperspectral Remote Sensing.* Swindon : Cranfield University, 2009. Mphil Tesis.

79. *Review of passive imaging polarimetry for remote sensing applications.* **Tyo, J. S., Goldstein, D. L., Chenault, D. B. and Shaw, J. A.** 22, Washington, DC. : Optical Society of America, 2006, Applied Optics, Vol. 45.

80. **Brosseau, C.** *Fundamentals of Polarized Light.* Toronto : John Wiley & Sons, Inc., 1998.

81. **Goldstein, D.** *Polarized light, revised and expanded (optical engineering).* New York : Marcer Decker AG, 2003.

82. *Visual Behavior Based Bio-Inspired Polarization Techniques in Computer Vision and Robotics.* **Shabayek, A. E., Morel, O. and Fofi, D. . In M. Pomplun,**

& J. Nantes, France : Institue of Physics (IOP) Publishing, 2011. International Workshop on Bio-inspired Robots.

83. *Illumination invariance and shadow compensation via spectro-polarimetry technique.* **Ibrahim, I., Yuen, P., Hong, K., Chen, T., Soori, U., Jackman, J. and Richardson, M.** 10, Bellingham, WA : SPIE, 2012, Optical Engineering (OE), Vol. 51.

84. **Ibrahim, I., Yuen, P., Tsitiridis, A., Hong, K., Chen, T., Jackman, J., James, D. and Richardson, M.** Spectral constancy on hyperspectral imageries. *Defence S&T Technical Bulletin.* 2011, Vol. 4, 1, pp. 19-30.

85. *Illumination independent object recognitions in hyperspectral imaging.* **Ibrahim, I., Yuen, P., Tsitiridis, A., Hong, K., Chen, T., Jackman, J., James, D. and Richardson, M.** Touluse, France : SPIE, 2010. Proceedings of the SPIE 7838. Vol. 7838, pp. 78380O-1-12 .

86. *Shadow compensation on hyperpsectral imageries.* **Ibrahim, I., Yuen, P., Soori, U., Chen, T., Hong, K., Tsitiridis, A., Jackman, J. and Richardson, M.** Shrivenham, Swindon : Defence Academy of the United Kingdom, 2012. 10th Electro-optics & Infrared Conference.

87. *Automated Spectral Unmixing of AVIRIS Data Using Convex Geometry Concepts.* **Boardman, J. W.** Fourth JPL Airborne Geoscience Workshop 93-26 : JPL Publication, 1993. Vol. 1.

88. *Comparative study between a new nonlinear model and common linear model for analysing laboratory simulated-forest hyperspectral data.* **Fan, W., Hu, B., Miller, J. and Li, M.** 2009, International Journal of Remote Sensing, pp. 2951 - 2962.

89. *Illumination and shadow compensation of hyperspectral images using a digital surface model and non-linear least squares estimation." 2011.* **Friman, O., Tolt, G. and Ahlberg, J.** s.l. : SPIE, 2011. Image and Signal Processing for Remote Sensing. Proc. of SPIE. Vols. 81800Q-1: 8.

90. *A new method for atmospheric correction and aerosol optical property retrieval for VIS-SWIR multi- and hyperspectral imaging sensors: QUAC (QUick atmospheric correction).* **Bernstein, L. S., Adler-Golden, S. M., Sundberg, R. L., Levine, R. Y., Perkins, T. C., Berk, A., Ratkowski, A. J., Felde, G. and Hoke, M. L.** Seoul, Korea : IEEE, 2005. Geoscience and Remote Sensing Symposium, 2005. IGARSS '05. Proceedings. 2005 IEEE International. pp. 3549 - 3552

91. *In-scene-based atmospheric correction of uncalibrated VISible-SWIR (VIS-SWIR) hyper- and multi-spectral imagery.* **Bernstein, L. S., Adler-Golden, S. M., Sundberg, R. L. and Ratkowski, A. J.** Cardiff, Wales, United Kingdom : SPIE, 2008. Proc. SPIE 7107, Remote Sensing of Clouds and the Atmosphere XIII, 710706.

92. *Active Spectral Imaging.* **Nischan, M. L., Joseph, R. M., Libby, J. C and Kerekes, J. P.** 1, 2003, Lincoln Laboratory Journal, Vol. 14, pp. 131-144.

APPENDICES

Appendix A Reflectance for shadow and direct pixels of 10 different coloured t-shirt data

The reflectance of a target under shadow is difficult to measure by optical sensors due to an insufficient radiation component in the signal reflected by the target. The signal captured by the sensor is always small but non-zero due to the diffuse irradiance which still remains on the scene, although the direct illumination is completely blocked by clouds or objects that cast the shadow. This diffuse irradiance is resulted from the scattered energy from the adjacent targets, background or environment. This appendix would show the comparison between direct and diffuse reflectance from the same targets of 10 different coloured t-shirt data.

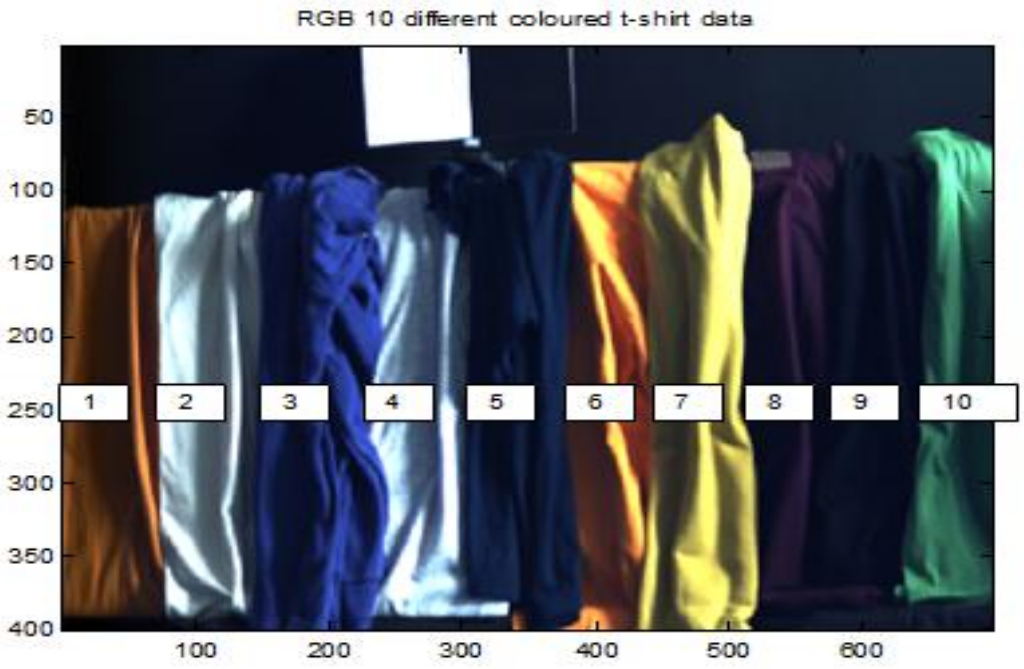

Figure A- 1 shows the RGB of 10 different coloured t-shirts data.

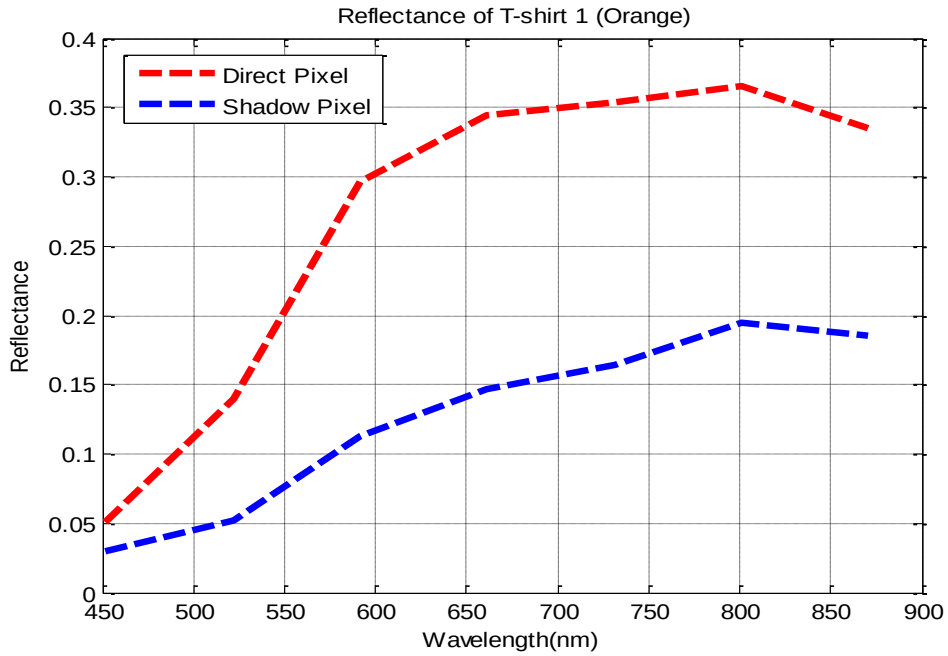

Figure A- 2 shows the plot of direct and shadow pixels for t-shirt 1.

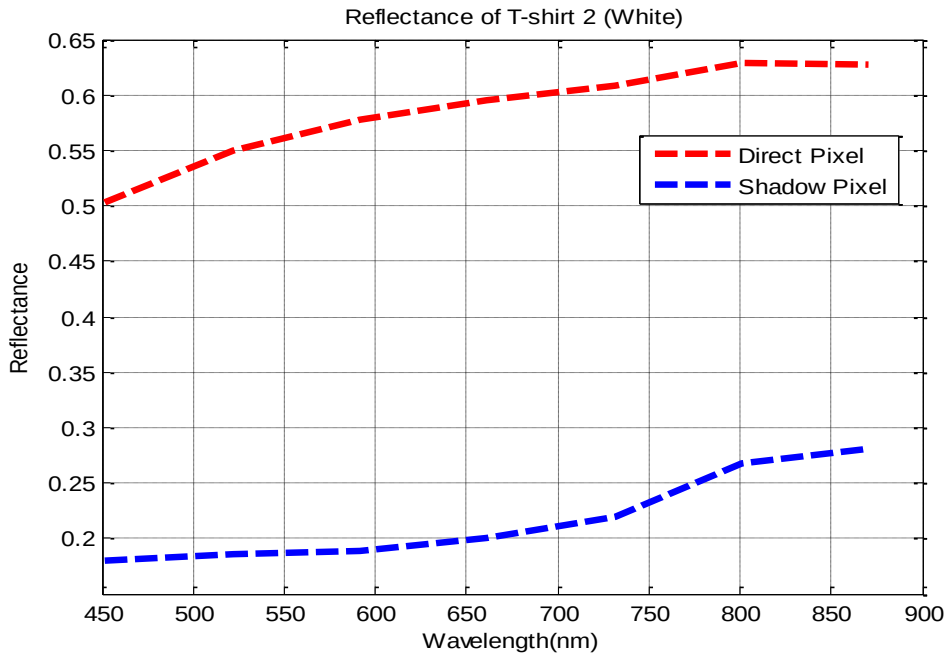

Figure A- 3 shows the plot of direct and shadow pixels for t-shirt 2.

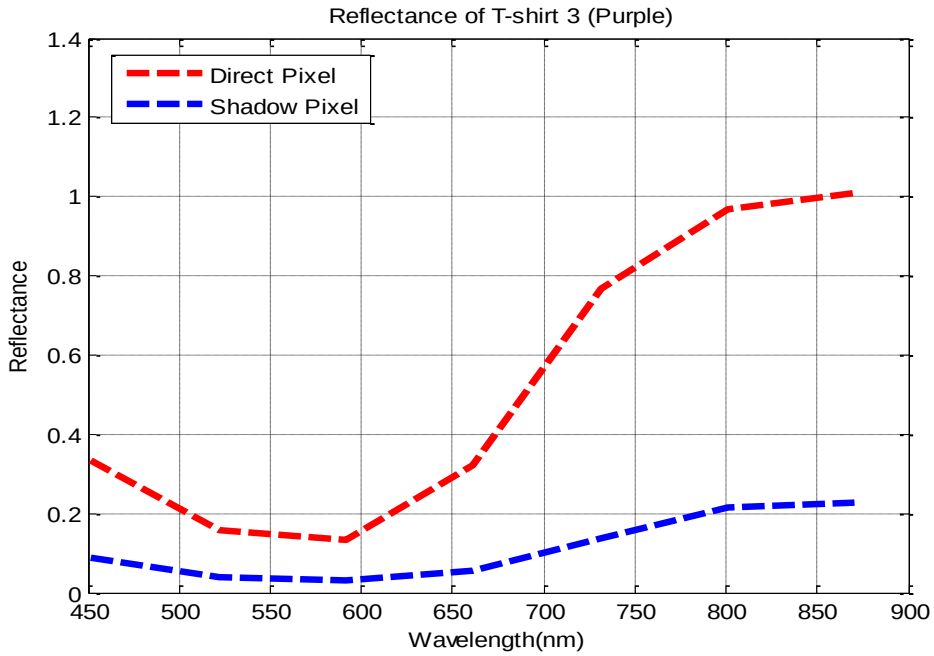

Figure A- 4 shows the plot of direct and shadow pixels for t-shirt 3.

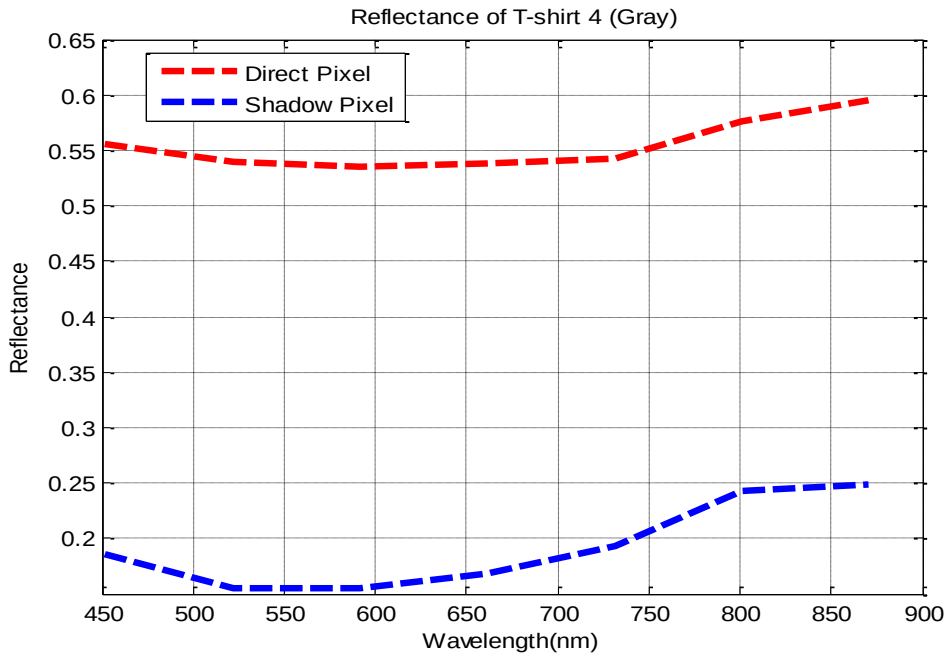

Figure A- 5 shows the plot of direct and shadow pixels for t-shirt 4.

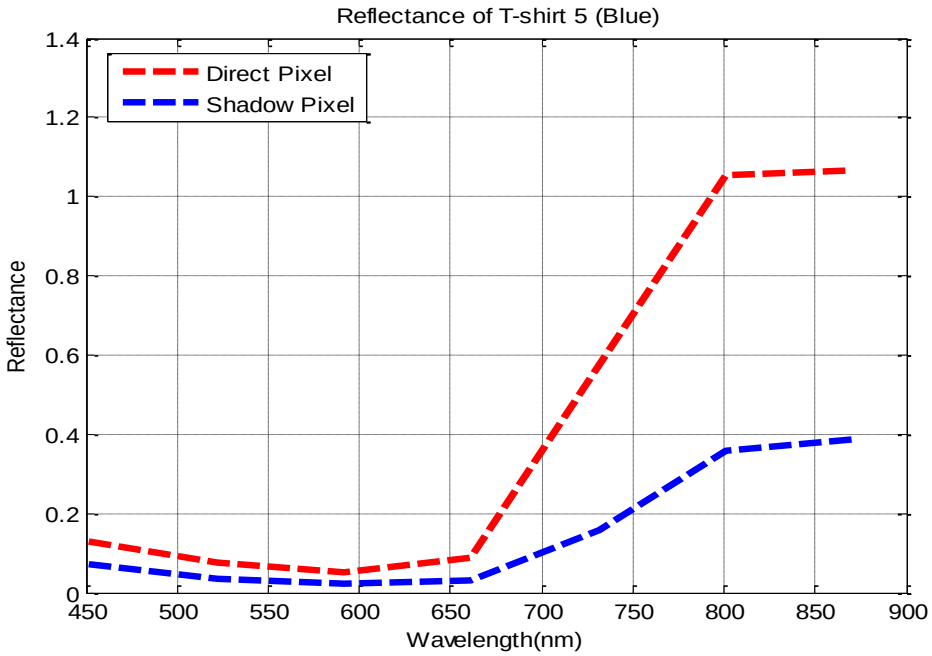

Figure A- 6 shows the plot of direct and shadow pixels for t-shirt 5.

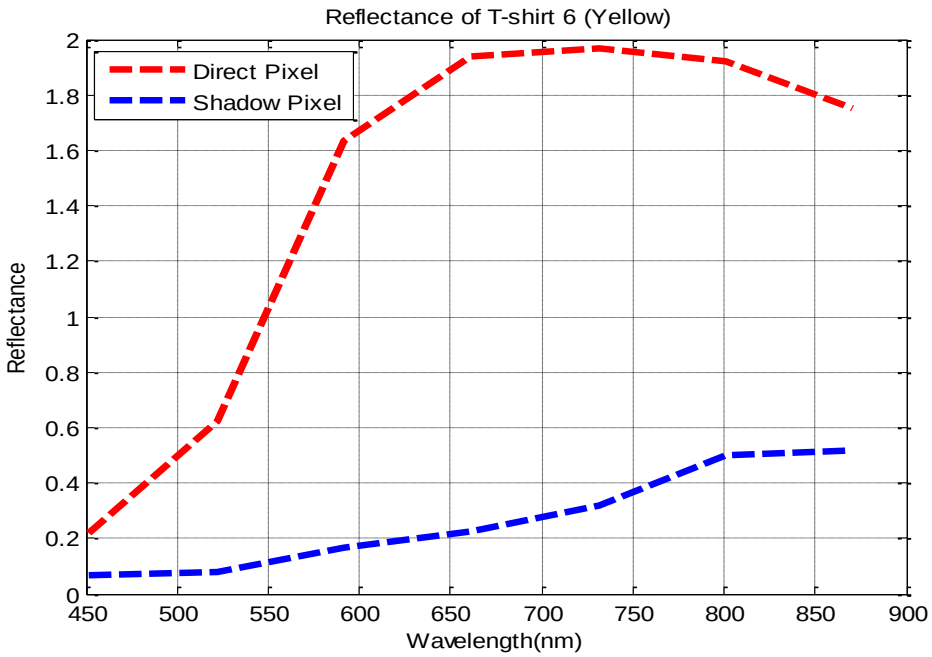

Figure A- 7 shows the plot of direct and shadow pixels for t-shirt 6.

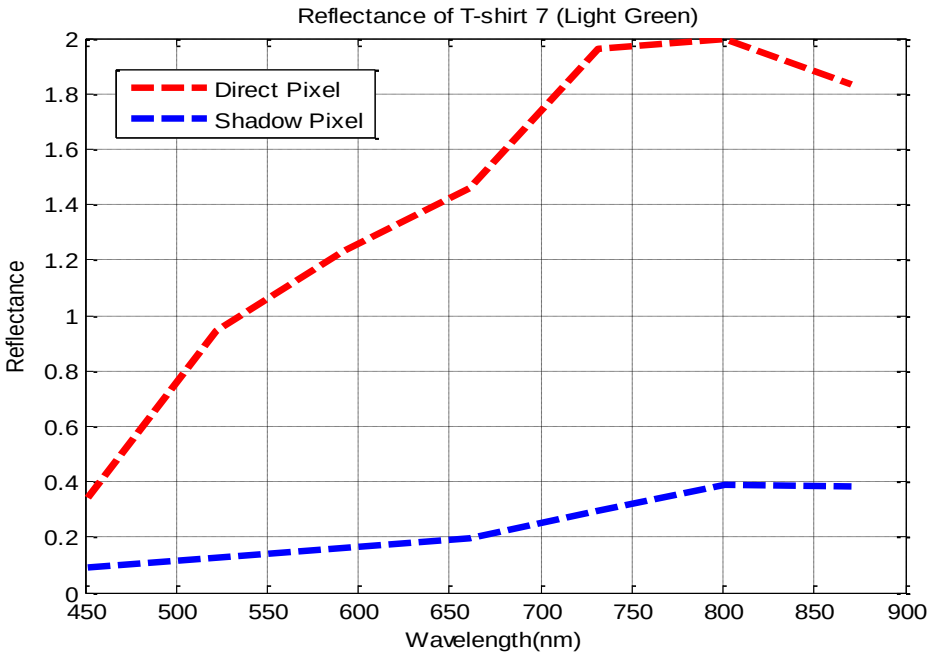

Figure A- 8 shows the plot of direct and shadow pixels for t-shirt 7.

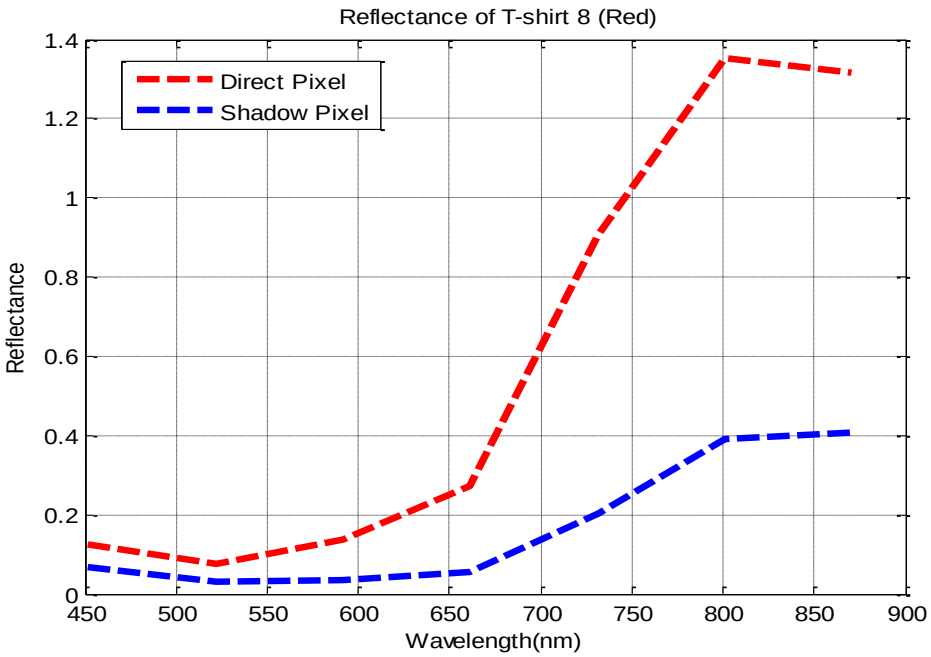

Figure A- 9 shows the plot of direct and shadow pixels for t-shirt 8.

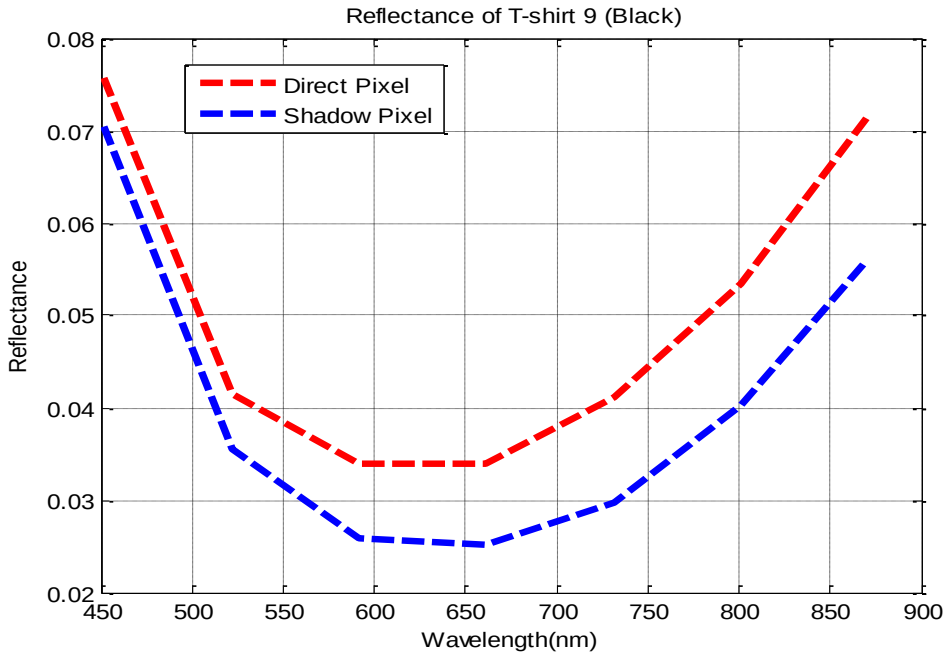

Figure A- 10 shows the plot of direct and shadow pixels for t-shirt 9.

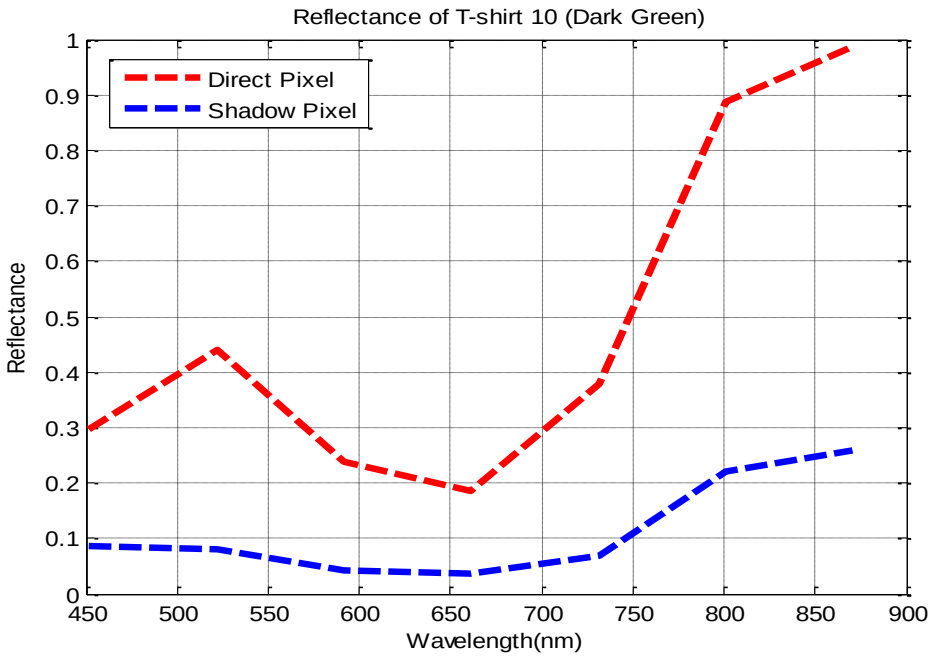

Figure A- 11 shows the plot of direct and shadow pixels for t-shirt 10.

Appendix B Reflectance for shadow and direct pixels of 5 different coloured t-shirt data

This appendix shows the comparison plot between direct and shadow reflectance from the same targets of 5 different coloured t-shirt data. Although the targets is label in colour as in 10 different coloured t-shirt data, the material of the t-shirt targets in different compared to the 10 different coloured t-shirt data. Figure B- 2 shows the RGB image of the 5 different coloured t-shirt data.

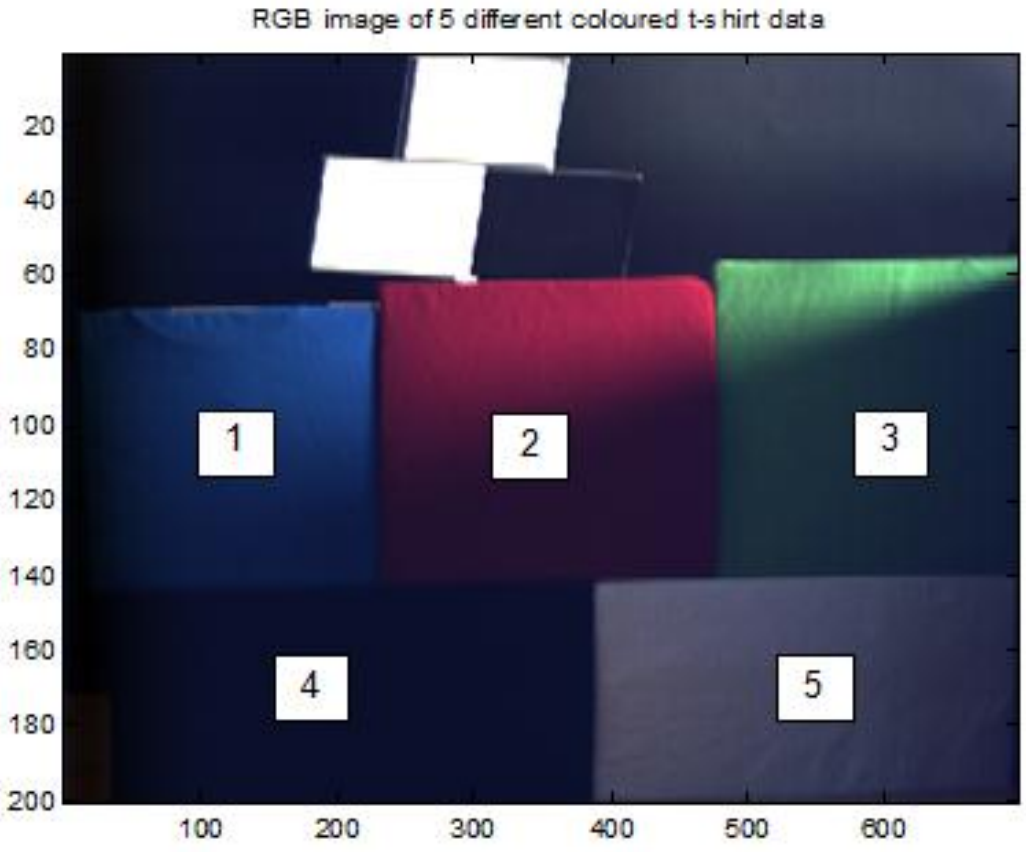

Figure B- 1 shows the RGB of 10 different coloured t-shirts data.

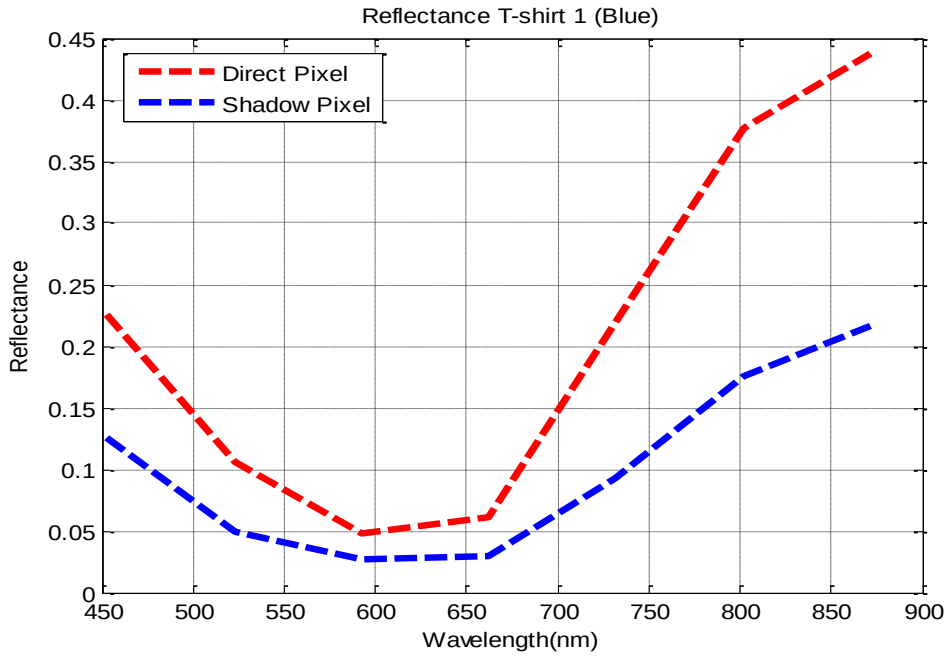

Figure B- 2 shows the plot of direct and shadow pixels for t-shirt 1.

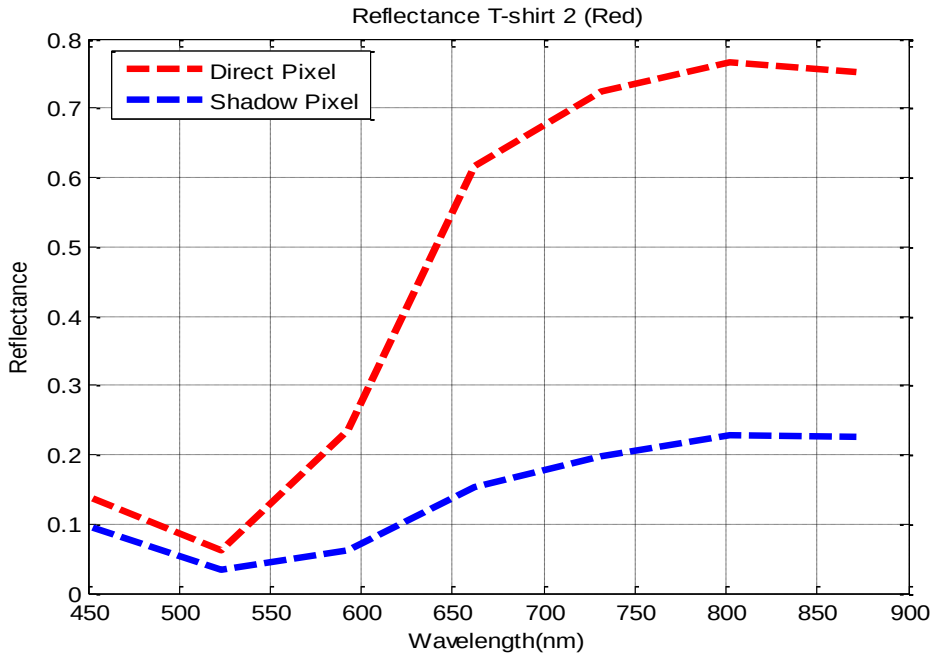

Figure B- 3 shows the plot of direct and shadow pixels for t-shirt 2.

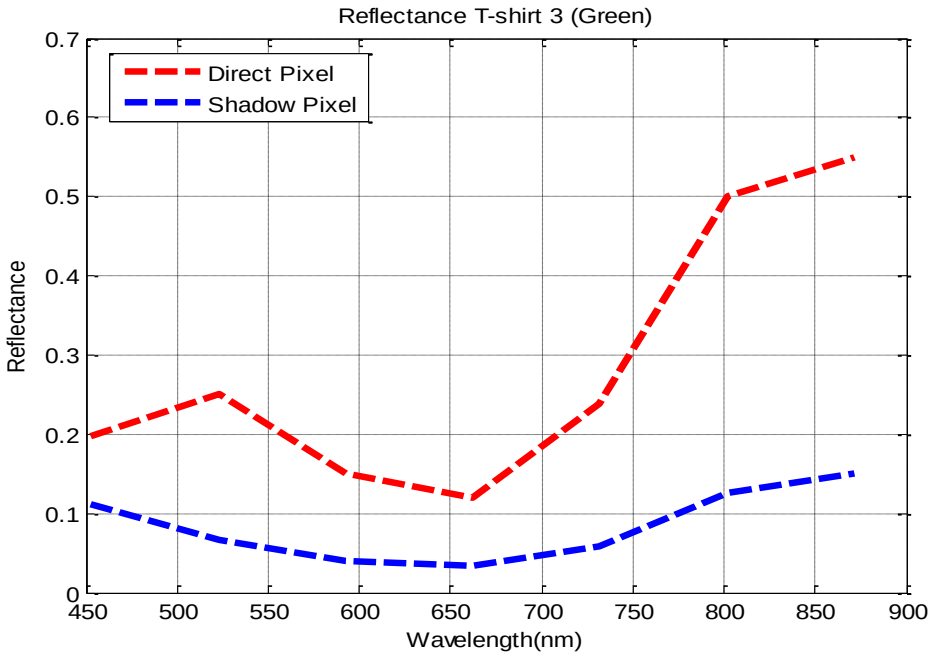

Figure B- 4 shows the plot of direct and shadow pixels for t-shirt 3.

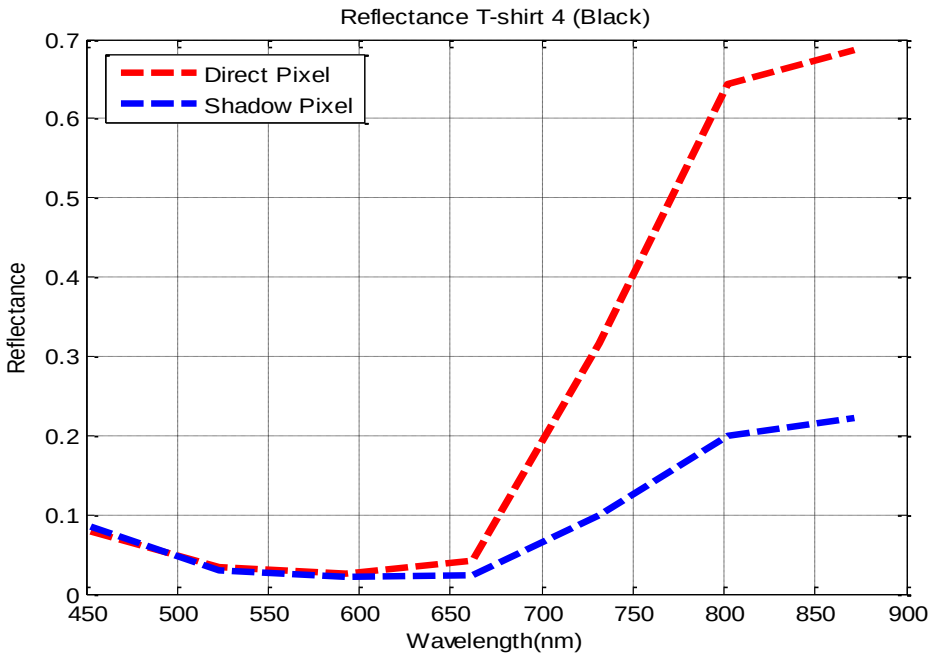

Figure B- 5 shows the plot of direct and shadow pixels for t-shirt 4.

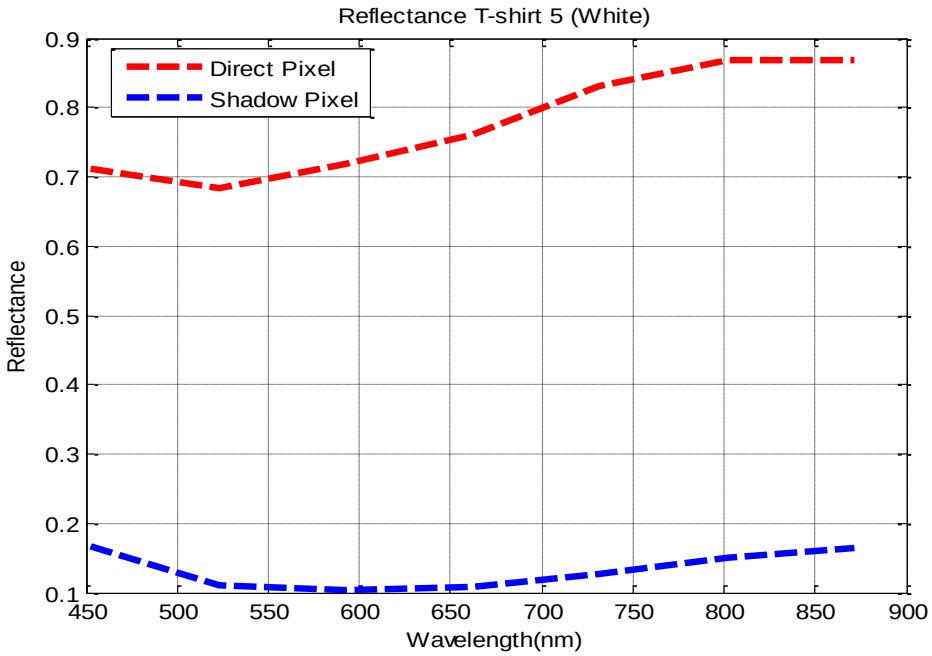

Figure B- 6 shows the plot of direct and shadow pixels for t-shirt 5.

Appendix C Classification accuracy for each class before and after correction

This appendix shows the Quadratic Classification (QD) result of each t-shirt for 10 different coloured t-shirts data before and after correction using DIC, LR and SP technique. This result has been compared with 2 other different classification methods such as Fisher Linear Classifier (FD) and Minimum Distance Classifier (MD).

Table C- 1 shows QD classification result for each t-shirt of 10 different coloured t-shirts data.

	Yellow	White	Purple	Gray	Blue	Orange	Green	Red	Black	Dark Green	Average
RW	33%	63%	99%	28%	62%	42%	95%	41%	39%	60%	**56%**
DIC	68%	70%	89%	48%	87%	12%	84%	47%	96%	99%	**70%**
LR	71%	84%	89%	74%	88%	20%	83%	49%	96%	99%	**75%**
SP	99%	83%	96%	75%	98%	96%	98%	79%	81%	93%	**90%**

Table C- 2 shows FD classification result for each t-shirt of 10 different coloured t-shirts data.

	Yellow	White	Purple	Gray	Blue	Orange	Green	Red	Black	Dark Green	Average
RW	93%	52%	68%	53%	61%	51%	61%	76%	100%	98%	**71%**
DIC	82%	79%	93%	57%	53%	38%	82%	89%	100%	99%	**77%**
LR	88%	79%	93%	77%	42%	24%	84%	82%	100%	98%	**77%**
SP	100%	80%	100%	66%	100%	98%	98%	90%	100%	90%	**92%**

Table C- 3 shows MD classification result for each t-shirt of 10 different coloured t-shirts data.

	Yellow	White	Purple	Gray	Blue	Orange	Green	Red	Black	Dark Green	Average
RW	81%	28%	17%	27%	42%	31%	16%	35%	100%	60%	**44%**
DIC	71%	59%	60%	39%	71%	10%	54%	60%	100%	85%	**61%**
LR	72%	59%	49%	39%	71%	11%	54%	60%	100%	89%	**60%**
SP	90%	82%	99%	79%	68%	90%	94%	75%	100%	91%	**87%**

The SP correction technique has shown substantial improvements in classification accuracy compared to that of the raw data and and after corrections by DIC and LR methods. In general the QD classifier exhibits the best classification performance as it involves both the mean and covarince for classification. The FD assumes the same covariance for all classes, while the MD does not involve covariance for classification and therefore, these classifiers have shown an inferior performance compared to that of the QD as it can be seen in the above tables.

The SP technique also shows consistently better results for the majority of colours, apart from black and dark green, as can be seen in Table C-1. When comparing similar colours, such as yellow and orange, the SP technique produces consistent results. However, this is not the case for the DIC and LR methods due to the fundamental drawbacks in them. This discrepency could be another topic of future work on spectral constancy in hyperspectral imaging.